Naval Research Laboratory

Washington, DC 20375-5000

(2)

NRL Memorandum Report 6648

Tests of Initialization Procedures With the NRL Limited Area Numerical Weather Prediction Model

K. D. SASHEGYI* AND R. V. MADALA

Atmospheric Physics Branch
Space Science Division

**Science Applications International Corporation*
P.O. Box 1303, McLean, VA 22102

June 29, 1990

REPORT DOCUMENTATION PAGE

Form Approved
OMB No. 0704-0188

1. AGENCY USE ONLY (Leave blank)	2. REPORT DATE	3. REPORT TYPE AND DATES COVERED
	1990 June 29	Interim

4. TITLE AND SUBTITLE
Tests of Initialization Procedures with the NRL Limited Area Numerical Weather Prediction Model

5. FUNDING NUMBERS
PE - 61153N
PR - RR033-034A
WU - DN156046

6. AUTHOR(S)
R. V. Madala and K. D. Sashegyi

7. PERFORMING ORGANIZATION NAME(S) AND ADDRESS(ES)
Naval Research Laboratory
Washington, DC 20375-5000

8. PERFORMING ORGANIZATION REPORT NUMBER
NRL Memorandum Report 6648

9. SPONSORING/MONITORING AGENCY NAME(S) AND ADDRESS(ES)
Office of Naval Research
Arlington, VA 22217

10. SPONSORING/MONITORING AGENCY REPORT NUMBER

11. SUPPLEMENTARY NOTES
*Science Applications International Corporation
P.O. Box 1303, McLean, VA 22102

12a. DISTRIBUTION/AVAILABILITY STATEMENT
Approved for public release; distribution unlimited.

12b. DISTRIBUTION CODE

13. ABSTRACT *(Maximum 200 words)*

Several methods are tested to reduce the undesirable gravity wave oscillations in numerical integrations of the Naval Research Laboratory's Limited Area Weather Prediction model. The split-explicit temporal integration scheme used in the model is shown by itself to reduce the amplitude of the external gravity wave oscillations in the first six hours of integration. In a static non-linear initialization procedure, a diagnostic relation is derived for the geopotential on the sigma surfaces of the model. The procedure provides a balanced initial state, except for an initial adjustment of the vertical motion in the first five hours of integration. A vertical mode initialization procedure, following Bourke and McGregor (1983) is also developed for the model. The scheme is tested on two grids, of differing domain size and grid resolution. Convergence of the scheme is shown to be faster for the case of smoother topography along the lateral boundaries. Integrations with two different lateral boundary treatments are compared. The procedure is shown to prevent gravity wave oscillations without producing a mean drift in the surface pressure, to provide a balanced mass divergence, and to produce smaller changes to the initial mass and wind fields, compared to the static initialization.

14. SUBJECT TERMS	15. NUMBER OF PAGES
Initial conditions, initialization, filtering gravity waves, Limited area numerical weather prediction model, static non-linear mass balance, vertical mode initialization	91
	16. PRICE CODE

17. SECURITY CLASSIFICATION OF REPORT	18. SECURITY CLASSIFICATION OF THIS PAGE	19. SECURITY CLASSIFICATION OF ABSTRACT	20. LIMITATION OF ABSTRACT
UNCLASSIFIED	UNCLASSIFIED	UNCLASSIFIED	UL

CONTENTS

TESTS OF INITIALIZATION PROCEDURES WITH THE NRL LIMITED AREA NUMERICAL WEATHER PREDICTION MODEL

1. INTRODUCTION

Various initialization procedures have been tested for use with the Naval Research Laboratory's (NRL) Limited Area Weather Prediction system. The system has been developed to study the development of extratropical cyclones, which occurred along or off the East coast of the U.S. during the Genesis of Atlantic Lows Experiment (GALE) and the Experiment on Rapidly Intensifying Cyclones over the Atlantic (ERICA). Errors in the analysis (which can be due to observational errors and unresolvable scales of motion) and inaccuracies in the model physics give rise to inertia- gravity wave oscillations in numerical integrations of the model. Such errors are reflected as unbalanced deviations in the wind and mass fields, which generate freely propagating inertia-gravity waves. For the external and first few internal vertical modes of the numerical model, the phase speeds of these free inertia- gravity waves are much larger than the speeds of meteorological systems. The resulting high frequency oscillations can be seen in the surface pressure for example, with amplitudes as large as 5 to 10 mb.

Over the years, various methods have been used to reduce these high frequency oscillations in integrations of numerical weather prediction models. Among these, initial conditions used for integrations of the model are sometimes modified or initialized by application of various filtering equations. In the conventional static initialization performed on pressure surfaces, horizontal scaling arguments are used to derive the non-linear mass balance equation, which relates the geopotential and the stream function of the non-divergent wind for the larger scale atmospheric motions (see Haltiner and Williams, 1980, for example). In midlatitudes it has been customary to use the observed geopotential heights to compute a statically balanced wind field, assuming the wind is geostrophic at the lateral boundaries of the model (see Bengtsson, 1975, for example). On the other hand in the tropics, the non-divergent wind is used to derive a statically balanced temperature from the geopotential (see Krishnamurti, 1979, for example). Since most numerical weather prediction models use vertical coordinates different from the pressure, these statically balanced mass and wind fields must be then

Manuscript approved May 2, 1990

interpolated to the model vertical coordinates, introducing some noise in the initial conditions. Sundqvist (1975) used horizontal scaling arguments to derive the non-linear mass balance equation directly on the vertical sigma levels of his numerical model. In the normal mode initialization, used in global numerical weather prediction models (Andersen, 1977, Daley, 1979, Temperton and Williamson, 1981, Williamson and Temperton, 1981, for example), the normal modes of the numerical model are computed and by projecting the initial wind and mass fields (which have been interpolated to the model coordinates) onto these normal modes, the high frequency inertia- gravity waves can then be removed. However in limited area models, it is not possible to define the horizontal structure of the normal modes. In the vertical mode initialization scheme of Bourke and McGregor (1983), filtering conditions for the inertia- gravity waves are applied to the model dynamical equations to derive linear diagnostic equations for the mass divergence and generalized geopotential for the first few vertical modes of the model. With the further condition that the linearized potential vorticity is unchanged by the procedure, the equations can be solved iteratively for the amplitude of the high frequency gravity waves in the initial conditions. The scheme has been shown to be an application of the normal mode initialization scheme used in global models, without the horizontal structure of the normal modes having to be computed (Juvanon du Vachat, 1986; Temperton, 1988).

To reduce the amplitude of these high frequency gravity wave oscillations in the NRL model, several basic types of initialization procedures have been used. A static initialization procedure, which had been developed for the NRL model, is tested. With the future implementation of a wind profiling network in the U.S., there is renewed interest in deriving geopotential heights from the wind field in the midlatitudes. In the NRL scheme then, the non-divergent wind is first computed from the analyzed winds on the pressure surfaces. The computed non-divergent wind and the analyzed temperatures are then interpolated to the model vertical coordinates. A diagnostic relation for the geopotential on the sigma surfaces of the numerical model is derived, by setting the tendency of mass divergence to zero and ignoring vertical advection and friction in the divergence equation. For the boundary condition on the geopotential, we generalized the conventional geostrophic relationship,

deriving diagnostic conditions for the normal derivatives of the geopotential by ignoring the tendencies of momentum in the momentum equations.

A second type of initialization procedure, based on the vertical mode initialization scheme of Bourke and McGregor (1983), has also been developed for the NRL model. As is customary, we keep the geopotential, temperature and pressure fixed at the lateral boundaries of the model. To provide a boundary condition for the mass divergence however, an approximate mass divergence is computed along the lateral boundary using the thermodynamic equation. In our scheme, changes in the tangential wind along the lateral boundaries are consistent with the changes in the vorticity and divergence computed by the scheme.

The effect of the split-explicit scheme, which is used for integration in time in the NRL model, and the non-linear initialization procedures in reducing gravity wave oscillations in integrations of the NRL model are investigated. The influence of two different lateral boundary treatments and two different grids of differing resolution and domain size are investigated. In these integrations, idealized boundary conditions are obtained by interpolation from operational analyses. To minimize the impact of noise from the boundaries influencing the interior, the boundary conditions are derived from initialized fields for the cases of integrations starting from initialized fields.

The numerical model, the vertical modes, the split-explicit integration scheme and the two different lateral boundary treatments are described in section 2. In section 3, the static initialization procedure is described and illustrated. The vertical mode scheme is then described in section 3. The convergence of the scheme is also shown for the two different grids. A low resolution grid with a resolution of 2° in longitude by 1.5° in latitude, covers the continental U.S., and a high resolution grid of 0.5° resolution in latitude and longitude covers the eastern U.S. In section 5, integrations with the split-explicit scheme for time integration are compared with a centered difference scheme on the high resolution grid, for uninitialized initial conditions. Integrations with the split-explicit scheme are then compared for varying degrees of static initialization. In section 6, integrations with

initial conditions, initialized with the vertical mode scheme, are compared to integrations with uninitialized fields for both the low and high resolution grids. Differences due to the different lateral boundary treatments are compared. The results are summarized and discussed in section 7.

2. MODEL DESCRIPTION

The Naval Research Laboratory's primitive equations model (Madala et al., 1987) uses sigma coordinates in the vertical and incorporates topography and physical parameterizations of the boundary layer and precipitation processes. The model is integrated in time using the efficient split-explicit method (Madala, 1981). In the horizontal, an Arakawa C grid (Arakawa and Lamb, 1977) is used with a latitude and longitude grid. The finite difference scheme is a second order quadratic conserving scheme. The model has been used for example to study the east coast snow storm of 10-12 February, 1983 (Chang et al., 1989). For experiments in this paper, ten layers of equal thickness (with $\Delta\sigma = 0.1$) are used in the vertical sigma (σ) coordinate from the surface ($\sigma = 1$) to the model top ($\sigma = 0$). The model includes large scale precipitation and a cumulus parameterization using a modified Kuo scheme. Unstable lapse rates are removed by a dry convective adjustment scheme following Manabe et al. (1965). The boundary layer is parameterized using a drag coefficient formulation, and second order horizontal diffusion is included.

Two different model grids are used for the model. A low resolution grid (called the US grid), with a resolution of 2° longitude by 1.5° latitude, covers the continental U.S. in a domain from 140.0°W to 40.0°W and 10.0°N to 70.0°N. The other grid (called the GALE grid) is a high resolution grid of 0.5° resolution in latitude and longitude, covering the eastern U.S. from 102.5°W to 57.5°W and 22.5°N to 47.5°N. Analyses at 14 standard pressure levels (from 50 to 1000 mb) on a 2.5° hemispheric grid from the National Meteorological Center (NMC) provide the initial conditions and idealized boundary conditions for model integrations in this paper. The NMC 2.5° resolution hemispheric analysis is interpolated to the horizontal model grid using Lagrangian cubic polynomial interpolation. The thermodynamic variables are interpolated in the vertical to the model sigma levels assuming they are linear in the log of the pressure, while the wind components are interpolated assuming they are linear in the pressure. An enveloped topography is derived for each model grid from the U.S. Navy's global 10 minute elevation data, by computing the average height for each model grid square and adding one standard deviation. On each model grid, the enveloped topography is then filtered by using the two-dimensional triangular smoother-desmoother of

Shapiro (1970), to filter out any wavelengths in the topography of twice the grid distance. For use with the vertical mode initialization scheme, the model topography is further smoothed by using one pass of the two-dimensional nine point triangular smoother (Shapiro, 1970). Climatalogical mean sea surface temperatures for the month of January of one degree resolution, taken from Reynolds (1982), are interpolated to the model grids.

2.1 Vertical Modes of the Model

In order to solve for the vertical modes of our numerical model, we linearize about a basic state at rest with a mean temperature T^*, which is a function of sigma only, and separate the linear and non-linear terms in the model dynamical equations. The model dynamical equations in flux form can then be written in matrix notation as

$$\frac{\partial \overline{p_s^x u}}{\partial t} + \delta_x \boldsymbol{\phi} = \mathbf{A}_u \tag{2.1}$$

$$\frac{\partial \overline{p_s^y v}}{\partial t} + \delta_y \boldsymbol{\phi} = \mathbf{A}_v \tag{2.2}$$

$$\frac{\partial p_s \mathbf{T}}{\partial t} + \mathbf{M}_2 \mathbf{D} = \mathbf{A}_T \tag{2.3}$$

$$\frac{\partial p_s}{\partial t} + \mathbf{N}_2^T \mathbf{D} = 0 \tag{2.4}$$

and the hydrostatic relation and continuity equation are written

$$\boldsymbol{\phi} - \boldsymbol{\phi}_s = \mathbf{M}_1 \mathbf{T} \tag{2.5}$$

$$p_s \dot{\sigma} = \mathbf{N}_1 \mathbf{D} \tag{2.6}$$

where column vectors are in bold type, $\mathbf{M}_1$, $\mathbf{M}_2$, $\mathbf{N}_1$ are matrices, and $\mathbf{N}_2^T$ represents the transpose of vector $\mathbf{N}_2$. The vertical sigma coordinate (σ) is defined by the ratio of the pressure p to the surface pressure p_s (Phillips, 1957). The dynamical variables are in vector form, where the elements of the vectors represent the values of the variables at each of the ten model sigma

levels for a single horizontal grid point. The vectors u, v represent the horizontal wind, T the temperature and ϕ the geopotential, at each of the model sigma levels, which are defined at the middle of each of the sigma layers in the vertical. ϕ_s is the surface geopotential (at $\sigma = 1$). The generalized geopotential Φ is defined as

$$\Phi = p_s[\phi-\phi_s + RT^*-\phi^*] \tag{2.7}$$

where the average geopotential ϕ^* on the sigma surface is related to the mean temperature T^* through the hydrostatic relation $\phi^* = M_1 T^*$. The vertical motion $\dot{\sigma}$ in the sigma coordinate (σ) is staggered in the vertical, being defined at sigma levels at the boundaries between the vertical layers. Subscripts representing the horizontal grid points on the C grid (see also grid mesh in Fig. 2 in section 2.3) have been omitted for clarity. The x and y coordinates are defined by multiplying the longitude and latitude in radians by the average radius of the earth. The mass divergence D on the sigma surfaces is defined on the C grid in our spherical coordinates by

$$D = \frac{1}{h_y}\,\delta_x\left(h_y\,\overline{p_s}^{x}\,u \right) + \frac{1}{h_x}\,\delta_y\left(\overline{h_x}^{y}\,\overline{p_s}^{y}\,v \right) \tag{2.8}$$

Here the difference operator δ is defined in the x direction, using the generalized geopotential Φ as an example, by

$$\delta_x\Phi = \frac{\Phi(x+\Delta x/2) - \Phi(x-\Delta x/2)}{h_x\ \Delta x} \tag{2.9}$$

where Δx is the grid spacing for the x coordinate and h_x (equal to the cosine of the latitude for our coordinate) is the map factor for the x coordinate. A similar difference operator is defined for the y coordinate, where the map factor is $h_y = 1$ in our case. An averaging operator is also defined in the x-direction, using the surface pressure as an example, by

$$\overline{p_s}^{x} = \frac{p_s(x+\Delta x/2) + p_s(x-\Delta x/2)}{2} \tag{2.10}$$

A similar averaging operator is defined for the y-coordinate and a two dimensional averaging can be defined as

$$\overline{p_s}^{xy} = \overline{\overline{p_s}^{x}}^{y} = \overline{\overline{p_s}^{y}}^{x} \qquad (2.11)$$

Elements of the matrices M_1, M_2, N_1 and the vector N_2 are functions of sigma only. The vectors on the right hand side (RHS) of Eqs. (2.1), (2.2) and (2.3) include Coriolis, friction, non-linear advection and diabatic terms. Details of the vector and matrix elements can be found in the report by Madala et al. (1987).

Solutions to the homogeneous equations (in which terms on the RHS of Eqs. (2.1), (2.2), (2.3) and (2.4) are zero) are freely propagating gravity waves. Now eliminating all variables in the homogeneous equations except Φ, we obtain

$$\frac{\partial^2 \Phi}{\partial t^2} - M_3 \nabla^2 \Phi = 0 \qquad (2.12)$$

where the matrix M_3 is defined as $M_3 = M_1 M_2 + (RT^* - \phi^*)N_2^T$ and whose elements are only functions of the vertical sigma coordinate and do not depend on the x and y coordinates. In our x and y spherical coordinates, the two dimensional Laplacian ∇^2 is defined by

$$\nabla^2 \Phi = \frac{1}{h_y} \delta_x (h_y \delta_x \Phi) + \frac{1}{h_x} \delta_y (\overline{h_x}^{y} \delta_y \Phi) \qquad (2.13)$$

Similarly, we can show that the mass divergence D satisfies the same equation (2.12), while the vorticity of the background flow is not affected by gravity wave motions. The equation (2.12) is separable and by separating the vertical structure, a set of vertical eigenmodes and corresponding eigenvalues can be obtained (see also Kasahara and Puri, 1981, for example). In terms of our matrix notation, the eigenvectors ϵ_k and corresponding eigenvalues λ_k are found by solving the matrix equation

$$M_3 \epsilon_k = \lambda_k \epsilon_k. \qquad (2.14)$$

If E represents the eigenvector matrix (with each column representing an eigenvector ϵ_k) of matrix M_3, and Λ is the diagonal matrix with the diagonal elements given by the eigenvalues λ_k, then we can write

$$M_3 E = \Lambda E. \qquad (2.15)$$

and by multiplying Eq. (2.12) by the inverse of $\mathbf{E}$ we have

$$\frac{\partial^2 \mathbf{e}}{\partial t^2} - \mathbf{\Lambda} \nabla^2 \mathbf{e} = 0 \qquad (2.16)$$

where $\mathbf{e} = \mathbf{E}^{-1} \mathbf{\Phi}$, and we have used the property of the eigenvector matrix that $\mathbf{E}^{-1} \mathbf{M}_3 \mathbf{E} = \mathbf{\Lambda}$, which can be easily verified by comparing the elements of matrices $\mathbf{M}_3 \mathbf{E}$ and $\mathbf{E} \mathbf{\Lambda}$ (see Strang, 1988, p254, for example). For each vertical mode we have

$$\frac{\partial^2 e_k}{\partial t^2} - \lambda_k \nabla^2 e_k = 0 \qquad (2.17)$$

where e_k is the amplitude of the generalized geopotential and λ_k is the

TABLE 1: Mean temperatures for 12Z January 23, 1986, on sigma surfaces of 10 layer model for GALE grid.

Model Level	Sigma Level	Temperature (°K)
1	0.05	205.9
2	0.15	214.0
3	0.25	222.1
4	0.35	236.1
5	0.45	249.4
6	0.55	259.4
7	0.65	266.6
8	0.75	271.9
9	0.85	275.9
10	0.95	278.4

TABLE 2: The equivalent depths and the phase speeds for the vertical modes of a ten layer model for the mean temperature profile defined in Table 1.

Mode No.	Equiv. Depth (meters)	Phase Speed (meters s^{-1})
1	9,399.0	303.5
2	1,508.0	121.6
3	226.6	47.1
4	85.7	29.0
5	30.3	17.2
6	13.7	11.6
7	6.4	7.9
8	2.7	5.1
9	0.9	3.0
10	0.2	1.3

eigenvalue for the k^{th} mode. Eq. (2.17) is a wave equation describing the propagation of the free gravity mode whose phase speed c_k is given by $\sqrt{\lambda_k}$. In the linearization used here to obtain the gravity modes, the Coriolis term is combined with the non-linear terms, and as such the gravity modes are applicable only for high frequencies or small time periods compared to the period of inertial oscillations. However it can be noted that the vertical structure of the modes derived in this case is unchanged even if the Coriolis terms are included with the linear terms on the left hand side of Eqs. (2.1) and (2.2). In this case the linearization defines the inertia- gravity modes (see section 4.1).

As an example the eigenmodes are computed for the ten layer model using a emperature profile taken from the NMC 2.5° hemispheric analysis for 122 January 23, 1986 during the second Intensive Observing Period (IOP) of GALE.

The temperatures are interpolated to the model grid and averaged on the sigma surfaces over the GALE grid covering the eastern U.S. The average temperatures on the model sigma levels at the middle of each layer are shown in Table 1. The eigenvalues and the phase speeds for each of the ten vertical modes computed are shown in Table 2. The eigenvalues are given in terms of equivalent depths defined by λ_k/g , where g is the acceleration due to gravity. The corresponding vertical structure for each of the modes is shown in Fig. 1. The number of zero crossings in the vertical structure of each mode is given by the mode number minus one. The phase speeds of the modes vary from 303.5 m s^{-1} for the external (first) mode to 1.3 m s^{-1} for the tenth mode. For the first three modes, the external mode and first two internal modes, the phase speeds are much faster than typical meteorological systems, which are typically less than 20 m s^{-1}. Then to integrate a model with a centered difference scheme in time and a grid spacing Δx, the time step 2 Δt must be small enough to satisfy the CFL condition $2\,\Delta t\,(U+c) / \Delta x \leq 1$, for the external gravity mode which has the fastest phase speed c, and where U is a maximum advecting wind speed (see for example Mesinger and Arakawa, 1976, p51). To allow the NRL model to be integrated more efficiently at a larger time step, more appropriate for meteorological systems, the split-explicit scheme was developed.

2.2 Split-Explicit Time Integration

In the split-explicit method of Madala (1981), a centered difference scheme is used with a large time step to compute initial estimates of the tendencies of the model variables for all the terms, except for diffusion which uses forward differencing. The time step satisfies the CFL condition for the phase speed of the 4^{th} gravity mode. To step the model variables at time t - Δt forward in time by 2 Δt, using the centered difference scheme, the non-linear terms and forces are computed at time t. These first estimates of the tendencies of the mass (surface pressure p_s, temperature T) and wind fields (u, v) are then corrected for the motion of the higher frequency gravity modes, assuming that the computed non-linear, Coriolis, diabatic and friction forcing terms are constant during the time step of 2 Δt. The specific humidity q is not corrected. To obtain the corrections, the amplitudes of the deviations of the divergence D - D(t) and the generalized geopotential

$\Phi - \Phi(t)$ are integrated over the interval of $2\Delta t$ at smaller time steps, for each of the first three vertical modes. For the external mode a time step of $\Delta t/8$ is used, while for the first two internal vertical modes time steps of $\Delta t/4$ and $\Delta t/2$, respectively, are used. The average of these deviations, over the interval of twice the large time step $2\Delta t$, is then used to correct the initial explicit estimate of the variables. Further details can be found in the Appendix. For the integration of the deviations of the divergence a lateral boundary condition is also required for the generalized geopotential. A boundary value for $\Phi - \Phi(t)$ is computed by a linear interpolation from the boundary values at $t-\Delta t$ and t. Further pragmatic boundary conditions are provided by reducing the amplitude and phase of the deviations of the divergence and generalized geopotential in a boundary zone (see the Appendix). Besides providing a 4 to 5 times saving in computer time over explicit methods, the averaging of the lower gravity wave eigenmodes can be expected to reduce the amplitude of the freely propagating higher frequency gravity waves.

2.3 Lateral Boundary Conditions

To update the large scale flow at the horizontal boundaries during the integration of the NRL model, externally prescribed boundary conditions are required for both the u and v components of the wind field and the mass and humidity fields. In the model, the mass and humidity variables of surface pressure p_s, temperature T, geopotential ϕ (or generalized geopotential Φ), and specific humidity q are defined at the lateral boundary. The wind components are staggered in the C grid and as applied to the NRL model, the tangential wind is defined at the boundary, while the normal wind is staggered half a grid point in from the boundary (see Fig. 2). In this paper two different lateral boundary treatments, the tendency relaxation scheme of Perkey and Kreitzberg (1976) and the Davies (1976, 1983) relaxation scheme, are used and compared for use with various initialization procedures. To provide the model boundary conditions in our experiments, idealized boundary values and tendencies are derived from the NMC 2.5 degree hemispheric analyses, interpolated to the model grid.

(a) Perkey Kreitzberg scheme.

In the Perkey Kreitzberg scheme, model computed tendencies for each of the dependent variables are blended with specified boundary tendencies in a

boundary zone of 5 points. After each time step, the model tendencies for each of the independent model variables are adjusted according to

$$\frac{\partial a}{\partial t} = (1-\alpha)\left[\frac{\partial a}{\partial t}\right]_m + \alpha\left[\frac{\partial a}{\partial t}\right]_b \tag{2.18}$$

where a is the independent model variable $\overline{p_s^x}u$, $\overline{p_s^y}v$, p_s, p_sT, or p_sq, subscript m represents the model computed value, and subscript b the prescribed boundary value. α is a linear function of the minimum distance (n) from the lateral boundary, in units of the grid spacing. As in Chang et al. (1989), we use for the mass and humidity variables (that is, for p_s, p_sT, p_sq)

$$\alpha = \begin{cases} 1 - \frac{n}{5} & \text{for } n \leq 5 \\ 0 & \text{for } n > 5 \end{cases} \tag{2.19}$$

while for the wind components $\overline{p_s^x}u$, $\overline{p_s^y}v$, which are staggered on the grid mesh, we use

$$\alpha_u = \begin{cases} 1 & \text{for } n \leq 0.5 \\ \bar{\alpha}^x & \text{for } n \geq 1 \end{cases} \tag{2.20}$$

$$\alpha_v = \begin{cases} 1 & \text{for } n \leq 0.5 \\ \bar{\alpha}^y & \text{for } n \geq 1 \end{cases} \tag{2.21}$$

The boundary tendencies, derived from the twelve hourly NMC analyses, are updated every twelve hours of model integration.

(b) Davies scheme.

In the Davies scheme, computed model variables are relaxed to the boundary values themselves at each time step in a boundary zone of 6 points. In this case, the model variables are adjusted at each time step according to

$$a = (1-\alpha)\, a_m + \alpha\, a_b \tag{2.22}$$

where, following Grønås et al. (1987), we define α as a quadratic function of the minimum distance (n) from the lateral boundary, in units of the grid spacing. For the mass variables we use

$$\alpha = \begin{cases} 1 & \text{for } n = 0 \\ \left[\frac{6.5 - n}{6} \right]^2 & \text{for } 1 \leq n \leq 5 \\ 0 & \text{for } n \geq 6 \end{cases} \qquad (2.23)$$

The functions α_u and α_v for the u and v components of the wind field are defined similarly as in Eqs. (2.20) and (2.21), using the averaging operators in the x and y coordinate directions, respectively. At each time step, the boundary values are computed by a linear interpolation in time from the 12 hourly NMC analyses.

3. STATIC INITIALIZATION

In the static initialization procedure used at NRL, a diagnostic relationship is derived for the geopotential on the sigma surfaces of the model. The non-divergent wind is first computed for the analyzed winds on the pressure surfaces. The NRL model differs from many other limited area models in that the tangential wind is specified at the lateral boundary of the model, instead of the normal wind. To compute the non-divergent wind then we solve for the stream function, assuming that the tangential wind along the lateral boundary is purely non-divergent. The non-divergent wind and the analyzed temperatures are then interpolated to the sigma coordinates of the model. A diagnostic relation is then derived for the geopotential on the sigma surfaces of the numerical model, by ignoring the tendency of divergence, vertical advection and friction. The initial non-divergent wind and analyzed temperatures, interpolated to the sigma surfaces, are used to compute the non-linear forcing terms. Boundary conditions for the normal derivatives of the geopotential are obtained by ignoring the tendencies in the momentum equations.

3.1 Non-Divergent Wind on Pressure Surfaces

For large scale atmospheric motions, the divergence of the velocity field is an order of magnitude smaller than the vorticity. To a first approximation then, the flow can be considered non-divergent on surfaces of constant pressure. On pressure surfaces, the vorticity ζ_p and divergence D_p are defined on the model horizontal grid as

$$\zeta_p = \frac{1}{h_y}\,\delta_x(h_y\, v) - \frac{1}{\overline{h_x}^{y}}\,\delta_y(h_x\, u) \tag{3.1}$$

$$D_p = \frac{1}{h_y}\,\delta_x(h_y\, u) + \frac{1}{h_x}\,\delta_y(\overline{h_x}^{y}\, v) \tag{3.2}$$

where u and v are the analyzed wind components on a pressure surface, interpolated to the horizontal grid of the model. The non-divergent flow can

then be described by introducing a stream function ψ, so that the non-divergent wind components u_ψ and v_ψ at that pressure level are given by

$$u_\psi = -\delta_y \psi \qquad (3.3)$$
$$v_\psi = \delta_x \psi$$

By computing the vorticity on the pressure surface, we can solve Poisson's equation,

$$\nabla^2 \psi = \zeta_p \qquad (3.4)$$

for the stream function ψ, and whence for the non-divergent wind. To provide boundary conditions for the stream function, we assume that the analyzed tangential wind along the boundary of our model domain is purely non-divergent. Then we obtain the Neumann boundary conditions for the stream function

$$\delta_y \psi = -u \quad \text{at } y = y_0, y_1 \qquad (3.5)$$
$$\delta_x \psi = v \quad \text{at } x = x_0, x_1$$

where y_0, y_1 give the southern and northern lateral boundaries and x_0, x_1 give the western and eastern boundaries. In this case the stream function is not unique, since adding a constant value to the solution of the stream function is also a solution. As described in the report of Sashegyi and Madala (1989), to obtain a unique solution for the stream function, we prescribe a value for the stream function $\psi = 0$ at a single arbitrary point on the boundary and use the elliptic equations solver of Madala (1978, 1981). Choice of a zero value as a first guess of the solution of the stream function then leads to the efficient convergence of Madala's elliptic equations solver.

As eloquently described by Lynch (1989), the partitioning of the wind into the divergent and non-divergent parts is not unique in a limited area domain. The choice of using the tangential wind on the boundary to describe the normal gradient of the stream function, minimizes the kinetic energy in the divergent wind and does not lead to a mixed divergent and non-divergent term in the kinetic energy balance. It can be noted that choice of defining the normal wind at the boundary in some models, instead of the tangential wind used in the NRL model, leads to solving Poisson's equation

$$\nabla^2 \chi = D_p \qquad (3.6)$$

for a velocity potential χ, which defines the divergent component of the wind. The non-divergent wind is then computed by subtracting the divergent component from the original wind field. For the boundary conditions in this case, it is

assumed that $\chi = 0$ at the lateral boundaries, that is, it is assumed that the divergent component of the wind is zero on the boundary.

3.2 Static Non-Linear Mass Balance

For large scale atmospheric motions, the time tendency of the divergence is small compared to the other terms in the divergence equation. A diagnostic equation for the geopotential on the sigma surfaces of the model can then be derived by ignoring this term. We can rewrite the model momentum equations (2.1) and (2.2) in the form

$$\frac{\partial \overline{p_s^x}^x u}{\partial t} + \overline{p_s^x}^x \delta_x \phi + R\, \overline{T}^x \delta_x p_s = N_u \tag{3.7}$$

$$\frac{\partial \overline{p_s^y}^y v}{\partial t} + \overline{p_s^y}^y \delta_y \phi + R\, \overline{T}^y \delta_y p_s = N_v \tag{3.8}$$

where we have included the non-linear advection of momentum, the Coriolis force and friction in the terms on the RHS. The equation for the mass divergence on the sigma surfaces is then obtained by taking δ_x of h_y times Eq. (3.7) and adding δ_y of h_x times Eq. (3.8) giving

$$\frac{\partial D}{\partial t} + \nabla\cdot[p_s \nabla(\phi - \phi_s)] = N_D - \nabla\cdot[RT\, \nabla p_s + p_s \nabla \phi_s] \tag{3.9}$$

where the horizontal geopotential gradient is given by $\nabla\phi = (\delta_x\phi, \delta_y\phi)$ and we have utilized the two dimensional divergence operator ∇ to define

$$N_D = \nabla\cdot N_V = \frac{1}{h_y}\delta_x(h_y N_u) + \frac{1}{h_x}\delta_y(\overline{h_x^y}^y N_v) \tag{3.10}$$

$$\nabla\cdot(p_s\nabla\phi) = \frac{1}{h_y}\delta_x(h_y \overline{p_s^x}^x \delta_x\phi) + \frac{1}{h_x}\delta_y(\overline{h_x^y}^y \overline{p_s^y}^y \delta_y\phi) \tag{3.11}$$

Here we have also defined the vector N_V by $N_V = (N_u, N_v)$. Since the time tendency of the divergence is assumed small compared to the other terms in the

mass divergence equation (3.9), we can ignore this term. That is, setting the tendency of the mass divergence zero in Eq. (3.9), we have

$$\nabla\cdot[p_s\nabla(\phi-\phi_s)] = N_D - \nabla\cdot[RT\,\nabla p_s + p_s\nabla\phi_s] \tag{3.12}$$

To compute the term N_D, we first compute the non-divergent wind on the pressure surfaces, as described in section 3.1. The non-divergent wind and the analyzed temperatures are then interpolated to the sigma surfaces of the model (see the beginning of section 2 on the model description). The non-divergent wind is then used to compute the terms on the RHS of Eqs. (3.7) and (3.8) ignoring vertical advection and friction (leaving horizontal advection and Coriolis forces). The analyzed temperatures and a surface pressure computed on the model topography by interpolation are used to compute the remaining forcing terms on the RHS of Eq. (3.12).

To solve Eq. (3.12), boundary conditions are required for the geopotential. To obtain the boundary conditions we ignore the tendencies of the u and v momentum in Eqs. (3.7) and (3.8) to obtain the Neumann boundary conditions for the geopotential

$$\overline{p_s}^{x}\,\delta_x(\phi-\phi_s) = N_u - R\,\overline{T}^{x}\delta_x p_s - \overline{p_s}^{x}\,\delta_x\phi_s \tag{3.13}$$

at $x = x_0 + \frac{\Delta x}{2}$, $x_1 - \frac{\Delta x}{2}$ and

$$\overline{p_s}^{y}\,\delta_y(\phi-\phi_s) = N_v - R\,\overline{T}^{y}\delta_y p_s - \overline{p_s}^{y}\,\delta_y\phi_s \tag{3.14}$$

at $y = y_0 + \frac{\Delta y}{2}$, $y_1 - \frac{\Delta y}{2}$,

where $y = y_0, y_1$ give the southern and northern lateral boundaries and $x = x_0, x_1$ give the western and eastern boundaries. In Fig. 2, our boundary conditions for the geopotential gradient are defined along the lines given by the shorter dashes, half a grid point in from the lateral boundary. Essentially, we have generalized the conventional geostrophic boundary condition relating the gradient of the geopotential to the geostrophic wind, by using the non-divergent wind and including the non-linear horizontal advection term. The

elliptic equation (3.12) can now be solved for the geopotential using the Neumann boundary conditions (3.13) and (3.14) with an elliptic equations solver, such as the Stabilized Error Vector Propagation (SEVP) solver (see Madala, 1978; Sashegyi and Madala, 1989). For the SEVP solver, the initial geopotential derived from the observed temperatures is used to provide the prescribed value at a point on the lateral boundary (to give a unique solution) and to provide the first guess for the solver.

The balanced temperatures on the sigma surfaces are then found from the balanced geopotential, by inverting the hydrostatic equation. Use of the hydrostatic equation to compute the temperature introduces a 2 $\Delta\sigma$ saw tooth wave structure in the vertical temperature profile. To remove this buckling, deviations of the temperatures T' from the mean temperature T^* are computed at sigma levels at the boundaries of the vertical layers (half way between the model sigma levels).

$$T' = \overline{T}^{\sigma} - \overline{T^*}^{\sigma} \tag{3.15}$$

The corrected temperatures are then obtained by adding the deviations (interpolated back to the model sigma levels) to the mean temperature and removing the mean of the deviations, so that the mean is unchanged.

$$T = T^* + \overline{T'}^{\sigma} - \langle \overline{T'}^{\sigma} \rangle \tag{3.16}$$

where $\langle\ \rangle$ is the horizontal average over the model domain on the sigma surface.

3.3 Application of Static Initialization

As an illustration of the scheme, the analyzed winds and temperatures, taken from the NMC analysis for 12Z January 23, 1986, are first interpolated to the model horizontal GALE grid for each of the 14 standard pressure levels from 50 to 1000 mb in a domain covering the eastern U.S. The horizontal resolution of the GALE grid is 0.5° in latitude and longitude in a domain 102.5°W to 57.5°W and 22.5°N to 47.5°N. The non-divergent wind is then computed as outlined above in section 3.1. In Fig. 3a we show the root-mean-square (rms) changes that result in the u-component of the wind field after

computing the non-divergent wind. Changes in the v-component of the wind field are similar. We see that average changes in the wind field are 2 m s^{-1} in the upper troposphere and 1.0 to 1.5 m s^{-1} in the middle and lower troposphere. The non-divergent wind and analyzed temperatures on the 14 standard pressure levels are then interpolated in the vertical to the ten model sigma levels. Our diagnostic equation for the geopotential is then used to compute a balanced geopotential on the sigma surfaces. In Fig. 3b we show the rms changes in the temperature at each of the model sigma levels resulting from solving for the non-linear mass balance. Changes in the temperature in the upper troposphere of 1°C reduce to 0.5°C in the middle troposphere. However in the lower troposphere large changes of 4.0°C are found. For comparison, the actual analyzed winds and temperatures are interpolated to the model sigma levels. In Figure 4, we compare the wind and temperature fields for the analyzed fields and the statically initialized fields, after having interpolated them back to 500 and 1000 mb pressure levels for display. At the 500 mb level, the temperature changes are small although the small trough is weaker as a result of the non-linear mass balance. At the 1000 mb level however the strength of the front is greatly weakened by the scheme, as is reflected in the large rms change in temperature seen in Fig. 3b.

4. IMPLICIT NORMAL MODE INITIALIZATION

We follow the vertical mode initialization scheme of Bourke and McGregor (1983) by using the model dynamical equations to filter out the high frequency inertia- gravity waves. Filtering conditions are applied to the model dynamical equations to derive linear diagnostic equations for the mass divergence and generalized geopotential, which are solved iteratively for the first three vertical modes of the numerical model. The further condition that the linearized potential vorticity is unchanged by the procedure is required to compute the vorticity. Boundary conditions on the generalized geopotential and mass divergence are required. As is customary, we keep the geopotential, temperature and pressure fixed at the lateral boundaries. To provide a boundary condition for the divergence, an approximate divergence is computed using the thermodynamic equation. In our scheme, changes in the tangential wind along the lateral boundaries are consistent with the changes in the vorticity and divergence computed by the scheme.

4.1 Inertia- Gravity Wave Modes

We express the dynamical equations in terms of the time tendencies of mass weighted vorticity, divergence and generalized geopotential, linearized about the basic state at rest with mean temperature T^*. The equations, with the β term included with the non-linear terms on the RHS, are

$$\frac{\partial \zeta}{\partial t} + f D = A_\zeta \tag{4.1}$$

$$\frac{\partial D}{\partial t} + \nabla^2 \phi - f \zeta = A_D \tag{4.2}$$

$$\frac{\partial \phi}{\partial t} + M_3 D = A_\phi \tag{4.3}$$

Here f is the Coriolis parameter, which is a function of latitude and we have further defined the mass weighted vorticity ζ on the sigma surfaces as

$$\zeta = \frac{1}{h_y} \delta_x (h_y \overline{p_s}^y v) - \frac{1}{h_x \overline{p_s}^x} \delta_y (h_x \overline{p_s}^x u) \tag{4.4}$$

In the equations we have ignored the staggering of the vorticity and mass divergence relative to the generalized geopotential.

The freely propagating inertia- gravity waves in the model are solutions to the linearized equations (4.1), (4.2) and (4.3) with the forcing terms on the RHS of the equations equal to zero. Taking the time derivative of Eq. (4.2) and eliminating the tendencies of the generalized geopotential and the vorticity using Eqs. (4.3) and (4.1) with the terms on the RHS zero, we find that the mass divergence satisfies the equation

$$\frac{\partial^2 D}{\partial t^2} + \left[f^2 - M_3 \nabla^2 \right] D = 0 \qquad (4.5)$$

In this case, the vertical modes, which are again found by solving for the eigenmodes of matrix M_3, have the same vertical structure as that computed for the gravity wave modes in section 2.1. The "ageostrophic deviations" $f\zeta - \nabla^2\Phi$, which is f times the ageostrophic vorticity, can also be shown to satisfy the same equation. Eliminating D from the homogeneous form of Eqs. (4.1) and (4.3), an expression for the tendency of the linearized potential vorticity Q is obtained

$$\frac{\partial}{\partial t} (M_3\zeta - f \Phi) = 0 \qquad (4.6)$$

where the linearized potential vorticity Q is defined as

$$Q \equiv (\zeta - f M_3^{-1} \Phi) \qquad (4.7)$$

That is, the linearized potential vorticity Q is unchanged by the inertia-gravity wave motions (see also Errico, 1986).

Now in terms of the amplitude of the mass divergence for each vertical mode, we have

$$\frac{\partial^2 d_k}{\partial t^2} + \left[f^2 - \lambda_k \nabla^2 \right] d_k = 0 \qquad (4.8)$$

By including the Coriolis parameter in the linearization, we have introduced a low frequency cutoff for the inertia- gravity wave modes (see also Gill, 1982, for example). Assuming that the latitudinal wavelength of the modes are small compared to the change in the Coriolis parameter f with latitude, Eq. (4.8) is a wave equation with the phase speed of the plane wave modes given by

$$c_k^2 = \lambda_k \left[1 + \left[\frac{1}{\kappa R_d} \right]^2 \right] \tag{4.9}$$

where R_d is the Rossby radius of deformation defined by

$$R_d = \frac{\sqrt{\lambda_k}}{f} \tag{4.10}$$

and $\kappa = (\kappa_x, \kappa_y)$ is the horizontal wavenumber with $\kappa^2 = \kappa_x^2 + \kappa_y^2$. At the higher frequencies (that is, for wavelengths small compared to $2\pi R_d$), the phase speeds of the modes can be approximately given by $\sqrt{\lambda_k}$ and the modes are essentially the gravity wave modes computed in section 2.1. For our ten layer model and our limited area domains, the gravity waves for the first two modes are largely of high frequencies, since the Rossby radius of deformation is large (7,256 km and 2,907 km at 35°N for example, for the first and second modes, respectively), compared to the size of the model domain. However, for the higher modes, the Rossby radius of deformation becomes comparable or smaller than the domain size (1,126 km and 693 km for the third and fourth modes at 35°N, for example), and the gravity waves are of lower frequency.

4.2 Vertical Mode Initialization

4.2.1 Filtering Equations. We want to reduce the initial amplitude and tendency of the high frequency inertia- gravity waves so that their amplitude remains small during the integration of the numerical model. By requiring that initially the first and second derivatives of the mass divergence are zero, the amplitudes of the high frequency inertia- gravity waves will be kept small during integration of the model. Taking the time derivative of Eq. (4.2) and substituting for the tendencies of the generalized geopotential and vorticity

from Eqs. (4.1) and (4.3), an expression for the second derivative of the mass divergence with respect to time is obtained,

$$\frac{\partial^2 D}{\partial t^2} - M_3 \nabla^2 D + f^2 D = \frac{\partial A_D}{\partial t} - \nabla^2 A_\Phi + f A_\zeta \qquad (4.11)$$

The terms on RHS of Eqs. (4.1), (4.2), (4.3), which include the beta and non-linear terms, vary slowly with time compared to the time scale for high frequency gravity waves. Therefore we can ignore the time tendency of A_D in Eq. (4.11). Then applying our filtering conditions

$$\frac{\partial D}{\partial t} = \frac{\partial^2 D}{\partial t^2} = 0 \qquad (4.12)$$

to Eqs. (4.2) and (4.11) respectively, we obtain

$$\nabla^2 \Phi - f \zeta = A_D \qquad (4.13)$$

$$M_3 \nabla^2 D - f^2 D = \nabla^2 A_\Phi - f A_\zeta \qquad (4.14)$$

To complete the set of equations a further condition is required. Assuming that the changes to our initial fields due to our filtering procedure will be small, then the changes to our fields represent that part of the fields due to the freely propagating inertia- gravity waves. If they are small, their motion can be described by the linearized equations (4.1), (4.2) and (4.3) with the terms on the RHS equal to zero. We can therefore require that the linearized potential vorticity be unchanged by our initialization procedure. Our filtering conditions are now

$$M_3 \nabla^2 \Phi - f^2 \Phi = M_3 (A_D + f Q_0) \qquad (4.15)$$

$$M_3 \nabla^2 D - f^2 D = \nabla^2 A_\Phi - f A_\zeta \qquad (4.16)$$

$$\zeta - f M_3^{-1} \Phi = Q_0 \text{ , a constant} \qquad (4.17)$$

We only need to filter the high frequency gravity waves, whose phase speeds are much larger than the typical speeds of weather systems. Therefore our

filtering conditions need only be applied for those vertical modes whose phase speeds are larger than about 25 m s^{-1}. For the ten layer model example shown in Table 2, filtering the first three modes is sufficient. Using the same vertical structure we defined earlier we can express our variables in terms of amplitudes for each of the vertical modes, where

$e = E^{-1}\Phi$, $d = E^{-1}D$, $v = E^{-1}\zeta$, $\eta = E^{-1}Q$.

Then our filtering conditions for the first three modes k = 1, 2, 3 can be written

$$\nabla^2 e_k - \frac{f^2}{\lambda_k} e_k = a_k \tag{4.18}$$

$$\nabla^2 d_k - \frac{f^2}{\lambda_k} d_k = \frac{1}{\lambda_k} b_k \tag{4.19}$$

$$v_k = \frac{f}{\lambda_k} \overline{e_k}^{xy} + \eta_0 \tag{4.20}$$

where the forcing functions a_k and b_k are the k^{th} elements of the vectors

$$a = E^{-1} (A_D + f \overline{Q_0}^{xy}) \tag{4.21}$$

$$b = E^{-1} (\nabla^2 A_\Phi - f \overline{A_\zeta}^{xy}) \tag{4.22}$$

Here we have reintroduced the averaging operators to take into account the staggering of the variables on our model grid. Since the forcing functions on the RHS of Eqs. (4.18) and (4.19) depend on the vorticity, divergence and geopotential, the set of equations is solved iteratively. With a first estimate for the variables given by the uninitialized fields, the forcing functions for the Helmholtz equations can be computed by integrating the model to obtain the non-linear terms A_D, A_Φ, A_ζ, and the initial potential vorticity Q_0 computed. By solving the Helmholtz equations for the amplitudes of generalized geopotential and divergence, new values of the variables can be computed. By recomputing the forcing functions the process can be repeated.

We require boundary conditions for the amplitudes of the generalized geopotential and the mass divergence to solve the Helmholtz equations at each iteration of our initialization procedure. We choose to keep Φ fixed at the boundary, so that at the boundary ϕ, T and p_s are unchanged by the

initialization procedure. It has been customary to set the amplitude of the mass divergence in the first three modes to zero along the boundary and adjusting the integrated divergence over the model domain. However for a domain with substantial topographic features along the boundary, this is too restrictive. We choose to estimate the divergence at the first mass point in from the boundary using the thermodynamic equation and neglecting the tendency of the generalized geopotential. In terms of the amplitudes of the vertical modes we have, using thermodynamic equation (4.3) with $\frac{\partial e}{\partial t} = 0$,

$$d_k = \frac{\{E^{-1} A_{\tilde{\Phi}}\}_k}{\lambda_k} \tag{4.23}$$

4.2.2 Iterative Procedure. By defining incremental changes to the amplitudes of mass divergence, generalized geopotential and vorticity for each iteration i

$$d_k^i = d_k^{i-1} + \Delta d_k^i \quad , \quad e_k^i = e_k^{i-1} + \Delta e_k^i \quad , \quad v_k^i = v_k^{i-1} + \Delta v_k^i \tag{4.24}$$

an equivalent scheme can be derived for the incremental changes. For the i^{th} iteration of the amplitudes of the generalized geopotential, mass divergence and vorticity, we have for the k^{th} mode

$$\nabla^2 e_k^i - \frac{f^2}{\lambda_k} e^i{}_k = a_k^{i-1} \tag{4.25}$$

$$\nabla^2 d_k^i - \frac{f^2}{\lambda_k} d^i{}_k = \frac{1}{\lambda_k} b_k^{i-1} \tag{4.26}$$

$$\lambda_k v_k^i - f \overline{e_k^{i}}^{xy} = \lambda_k v_k^{i-1} - f \overline{e_k^{i-1}}^{xy} \tag{4.27}$$

We can use Eqs. (4.2) and (4.11) to compute the residuals which remained after the previous $(i-1)^{th}$ iteration. Using Eq. (4.17) to substitute for the vorticity in the equation for the mass divergence Eq. (4.2) and multiplying by E^{-1}, we find that

$$\nabla^2 e_k^{i-1} - \frac{f^2}{\lambda_k} e^{i-1}{}_k = a_k^{i-1} - \frac{\partial d_k}{\partial t}^{i-1} \tag{4.28}$$

That is, the residual remaining after the $(i-1)^{th}$ iteration for the equation of the amplitude of the generalized geopotential is given by the tendency of the mass divergence. A similar residual can be computed for equation for the amplitude of the mass divergence. Taking the time derivative of Eq. (4.2) and substituting for the second time derivative of the mass divergence in Eq. (4.11) and then multiplying by E^{-1}, we find

$$\nabla^2 d_k^{i-1} - \frac{f^2}{\lambda_k} d_k^{i-1} = \frac{1}{\lambda_k} b_k^{i-1} - \frac{1}{\lambda_k} \frac{\partial}{\partial t} \left[\nabla^2 e_k^{i-1} - f \overline{v_k^{i-1}}^{xy} \right] \tag{4.29}$$

That is, the residual remaining after the $(i-1)^{th}$ iteration is given by the tendency of the amplitude of the ageostrophic deviation $f\zeta - \nabla^2\phi$. Then by subtraction, we find that the incremental changes are forced by

$$\nabla^2 \Delta e_k^i - \frac{f^2}{\lambda_k} \Delta e_k^i = \frac{\partial d_k^{i-1}}{\partial t} \tag{4.30}$$

$$\nabla^2 \Delta d_k^i - \frac{f^2}{\lambda_k} \Delta d_k^i = \frac{1}{\lambda_k} \left[\nabla^2 \frac{\partial e_k^{i-1}}{\partial t} - f \overline{\frac{\partial v_k^{i-1}}{\partial t}}^{xy} \right] \tag{4.31}$$

$$\Delta v_k^i = \frac{f}{\lambda_k} \overline{\Delta e_k^i}^{xy} \tag{4.32}$$

where the terms on the RHS of Eqs. (4.30), (4.31) are now the residuals from the previous iteration. To compute the residuals on the RHS, we integrate the model one time step to compute adiabatic tendencies without friction, diabatic heating, or updating of the values of the model variables at the lateral boundaries. The residuals are then computed from

$$\frac{\partial d}{\partial t} = E^{-1} \frac{\partial D}{\partial t} = E^{-1} \left[\delta_x \left[\frac{\partial \overline{p_s}^x u}{\partial t} \right] + \frac{1}{h_x} \delta_y \left[\overline{h_x}^y \frac{\partial \overline{p_s}^y v}{\partial t} \right] \right] \tag{4.33}$$

$$\frac{\partial v}{\partial t} = E^{-1} \frac{\partial \zeta}{\partial t} = E^{-1} \left[\delta_x \left[\frac{\partial \overline{p_s}^y v}{\partial t} \right] - \frac{1}{\overline{h_x}^y} \delta_y \left[h_x \frac{\partial \overline{p_s}^x u}{\partial t} \right] \right] \tag{4.34}$$

$$\frac{\partial e}{\partial t} = E^{-1} \frac{\partial \phi}{\partial t} = E^{-1} \left[M_1 \left[\frac{\partial p_s T}{\partial t} \right] + \left[R T^* - \phi^* \right] \left[\frac{\partial p_s}{\partial t} \right] \right] \tag{4.35}$$

In terms of the changes to the amplitude of the generalized geopotential our boundary condition on changes to e becomes

$$\Delta e_k = 0. \tag{4.36}$$

In terms of changes to the amplitude of the divergence the boundary condition becomes

$$\Delta d_k = \frac{1}{\lambda_k} \frac{\partial e_k}{\partial t} \tag{4.37}$$

4.2.3 Changes to the Horizontal Wind, Temperature and Surface Pressure. The resulting changes to the horizontal wind field can then be computed from the changes in the divergence and vorticity by solving for the changes in the velocity potential and the stream function. The grid stencil for the divergence (and velocity potential) and the vorticity (and stream function) is shown in Fig. 5. That is, given the change in the divergence $\Delta D = E\,\Delta d$ we solve a Poisson's equation

$$\nabla^2 \Delta\chi = \Delta D \tag{4.38}$$

for the change $\Delta\chi$ in the velocity potential χ at the interior mass (generalized geopotential Φ) points (see Fig. 5) for each sigma level of the model. The boundary condition on $\Delta\chi$ is

$$\Delta\chi = 0 \tag{4.39}$$

at the model lateral boundaries. This produces no change in the tangential wind along the model boundaries, but only change to the divergent wind in the interior. Now given the change in the vorticity $\Delta\zeta = E\,\Delta v$ we solve a Poisson's equation

$$\nabla^2 \Delta\Psi = \Delta\zeta \tag{4.40}$$

for the change $\Delta\Psi$ in the stream function Ψ for each sigma level of the model. The vorticity changes calculated from Eq. (4.32) are specified at interior points staggered half a grid distance from the mass and wind points. Since the integrated vorticity over the domain may change, the integrated tangential wind along our model boundary may change. We therefore prescribe a boundary condition of no change in the stream function

$$\Delta\Psi = 0 \tag{4.41}$$

at fictitious boundary staggered half a grid point outside our model boundary, implying that the non-divergent wind does not change there. However the non-divergent wind and hence the tangential wind does change along the model

boundary. The gradients of the changes of the stream function and the velocity potential at each sigma level of the model then define the changes to the mass weighted wind,

$$\Delta(\overline{p_s^x u}) = \delta_x \Delta\chi - \delta_y \Delta\Psi \tag{4.42}$$

$$\Delta(\overline{p_s^y v}) = \delta_y \Delta\chi + \delta_x \Delta\Psi \tag{4.43}$$

With the changes to the wind field defined in this way, the changes to the wind field along the lateral boundaries of the model are consistent with the changes in the vorticity and mass divergence over the model domain.

Following Temperton (1984), the changes in the surface pressure p_s, and the temperature T can be derived directly from changes in the generalized geopotential Φ. We consider the linearized equations for the motion of the freely propagating gravity waves

$$\frac{\partial \Phi}{\partial t} = - M_3 D \tag{4.44}$$

$$\frac{\partial p_s T}{\partial t} = - M_2 D \tag{4.45}$$

Now eliminating D we can relate the tendencies of surface pressure and temperature to that of the generalized geopotential for gravity wave motions, so that

$$\frac{\partial p_s}{\partial t} = - N_2^T D = N_2^T M_3^{-1} \frac{\partial \Phi}{\partial t} \tag{4.46}$$

$$\frac{\partial p_s T}{\partial t} = M_2 M_3^{-1} \frac{\partial \Phi}{\partial t} \tag{4.47}$$

Since the changes derived from our initialization procedure represent the gravity wave part of the flow, we can assume a wave solution for the changes. The changes to the surface pressure and temperature are then related to the changes in the generalized geopotential by

$$\Delta p_s = N_2^T M_3^{-1} \Delta\Phi = N_2^T M_3^{-1} E \Delta e \tag{4.48}$$

$$\Delta(p_s T) = M_2 M_3^{-1} \Delta\Phi = M_2 M_3^{-1} E \Delta e \tag{4.49}$$

4.3 Convergence of the Vertical Mode Scheme

To test our vertical mode initialization procedure, we use the 12 hourly NMC 2.5° hemispheric analyses for the period 12Z January 23 to 12Z January 29, 1986, for the period of the second Intensive Observing Period (IOP) of GALE. The initial synoptic situation, showing a cold front moving off the east coast of the U.S. and a low in the Gulf of Alaska, is shown in Figs. 4 and 8. During this IOP, a coastal front develops along the east coast of the U.S. and subsequently, a cyclone develops offshore when the low system from the Gulf of Alaska reaches the east coast. The thirteen analyses for the period are interpolated to the model coordinates for the two different horizontal grids with differing domain size and resolution and then initialized with the vertical mode scheme for the first three vertical modes only. The US grid covers a domain including the continental U.S.A. with a horizontal resolution of 2° longitude by 1.5° latitude. The GALE grid covers a smaller domain including the eastern half of the U.S.A. and extending out over the Atlantic to 52.5°W with a finer horizontal resolution of 0.5° in longitude and latitude. In the vertical, both grids use ten equally spaced sigma levels. The smoothed model topography used for each grid is shown in Fig. 6a and b. For the GALE grid, a case with smoother topography along the lateral boundary, shown in Fig. 6c, is also generated by merging the courser topography from the US grid (Fig. 6a) with the GALE topography (Fig. 6b) in a boundary zone with a width of five degrees in latitude and longitude. The merging is carried out by linearly interpolating the courser topography from the US grid to the GALE grid, and replacing the GALE topography at the first seven points in from the boundary. At the eight to tenth points, a linear combination is used with weights given by (0.75, 0.25), (0.5, 0.5) and (0.25, 0.75) for the course topography and GALE topography, respectively.

4.3.1 Using the low resolution US grid. At the analysis times, the initial amplitudes for the mass divergence and vorticity are computed on the US grid for each of the vertical modes, prior to initialization. The mean amplitudes of the mass divergence and vorticity for each of the vertical modes are averaged over the US domain and in time over the period of interest for the thirteen analyses and shown in Table 3. The mean amplitude of the vorticity decreases with increasing mode number, while the mean amplitude of

TABLE 3: The mean mass divergence and vorticity on the sigma surfaces of the model for the US grid, averaged for the week of 12Z January 23 to 12Z January 29, 1986.

Mode No.	Mass Divergence (dynes cm^{-2} s^{-1})	Vorticity (dynes cm^{-2} s^{-1})
1	7.68	82.04
2	7.54	36.28
3	12.63	36.98
4	9.08	32.86
5	7.63	17.53
6	6.32	11.82
7	4.81	8.14
8	3.81	5.56
9	2.92	4.41
10	1.82	2.65

the mass divergence maximizes at the third mode. As expected, the amplitudes of the divergence are an order of magnitude smaller than the amplitude of vorticity for the external mode. The analyses, interpolated to the model sigma coordinates for the US grid, are initialized with the vertical mode scheme for the first three vertical modes only. After each iteration of our vertical mode initialization procedure, the resulting root-mean-square (rms) changes in the amplitudes of the mass divergence, vorticity, generalized geopotential and surface pressure were computed. In Fig. 7 we show these rms changes, averaged for all the analysis times, at each iteration of the initialization procedure. For each of the first three vertical modes initialized, it can be noted that the mean rms changes in the amplitudes of the divergence at the first iteration of the procedure are as large as the initial amplitudes themselves, while the changes in the amplitude of the vorticity are very small compared to

their initial values. For the first two modes, the changes in the amplitude of the mass divergence decrease rapidly with increasing iterations, with the changes being very small after just two iterations. For the third mode, the changes in amplitudes of the mass divergence do not decrease as rapidly. The mean rms changes in the surface pressure, shown in Fig. 7d are less than a mb for each iteration.

To demonstrate the effect of the number of modes initialized on the changes in the amplitude of the mass divergence with each iteration, the number of modes initialized is varied from one to six modes for the case of one analysis on 12Z January 23, 1986. In Fig. 7e we show the changes in the mass divergence for the highest mode number initialized for each of the cases. The rate of decrease in the mass divergence changes increases as the higher order modes are initialized, and in fact increases with iteration for the sixth mode initialized. For the first two modes, the gravity waves are essentially of high frequency, since the Rossby radius of deformation is so large for these modes (see section 4.1). As the mode number increases however, the Rossby radius of deformation decreases and the frequency of the inertia-gravity mode decreases for the same wavelengths. The tendencies of the mass divergence for the gravity modes are then much less for the higher order modes, and convergence of the scheme would be expected to be slower.

As an illustration, we demonstrate the result of the vertical mode initialization using the NMC analysis for 12Z January 23, 1986. The initial analyzed sea-level pressure and wind field at the sigma level $\sigma = 0.25$ are shown in Figs. 8a and 8b. A deep surface low of 987 mb lies west of Greenland and high pressure dominates the eastern U.S. Aloft at the jet level, strong jet maxima of about 55 and 48 m s^{-1} straddle a trough over the eastern U.S., with a further jet maximum upstream, entering the domain from the Gulf of Alaska. The surface pressure change resulting from the vertical mode initialization is shown in Fig. 8c. The surface pressure adjustments due to initialization are small, with an rms change in this case of 0.9 mb and at most several mb in places. After the initialization, the vertical motion $\dot{\sigma}$ in the middle troposphere at a sigma level $\sigma = 0.45$, is shown in Figure 8d. Upward motion relative to the sigma surface (negative values of the vertical motion) is found on the south side of the jet off the coast of North America

and also ahead of the exit region of the jet streak. Sinking motion is found in the region of the high surface pressure over the eastern U.S. In sigma coordinates, the sigma surfaces follow the sloping topography, with the result that westerly flow in the lee of mountains gives rise to strong upward motions on the sigma surface. Such strong topographic signatures are seen in the lee of the Rockies and the Appalachian mountains. In Fig. 9 we compare the contributions to the vertical motion from the first three modes (Fig. 9a), which are initialized, and from the remaining modes (Fig. 9b), which are unchanged by the initialization procedure. The strong signal due to the mountains clearly dominates the vertical motion computed for the first three modes, while smaller synoptic scale magnitudes are apparent in the remaining modes.

The vertical mode initialization scheme removes that portion of the initial wind and mass fields that describe the inertia- gravity waves (for modes 1 to 3). Such structures then should be seen in the changes made to the analyzed fields resulting from the initialization. In Fig. 10a we show the wind and geopotential height changes at the jet level $\sigma = 0.25$. At the jet level, we see that the geopotential changes reach 30 to 40 gpm in places. The wind field shows flow of several m s^{-1} crossing the contours of geopotential height, indicative of inertia- gravity wave structures (see Matsuno, 1966, for example). At the same level the changes in temperature and the u and v components of the wind are shown in Fig. 10b, c and d. The changes in the temperature are at most a degree, while changes in the wind components are at most several m s^{-1}. Typical vertical profiles of the rms changes in the u component and the temperature are shown in Fig. 11. The resulting changes in the mean temperature, shown in Table 4, are very small and at most 0.15°C in the upper troposphere.

4.3.2 Using the high resolution GALE grid. For the smaller GALE grid with 0.5 degree resolution, the mean amplitudes for the vorticity and mass divergence are shown in Table 5, for each of the vertical modes. For each iteration of our vertical mode initialization scheme, the mean rms changes in the amplitudes of the divergence and the vorticity are shown in Fig. 12, for the first three modes initialized. In this case, the amplitude changes for the geopotential (or equivalently vorticity) decrease very rapidly for all the

TABLE 4: The root-mean-square changes in the mean temperature on the US grid for 12Z January 23, 1986, resulting from vertical mode initialization.

Model Level	Sigma Level	ΔT^* (°K)
1	0.05	0.052
2	0.15	0.143
3	0.25	0.098
4	0.35	0.048
5	0.45	0.022
6	0.55	0.018
7	0.65	0.014
8	0.75	0.069
9	0.85	-0.001
10	0.95	-0.011

three modes. However, the amplitude changes for the mass divergence in the case of the third mode do not decrease as rapidly and in fact do not reduce to zero. On the GALE grid, smaller scale topographic features of appreciable amplitude are present (see Fig. 6b), compared to the US grid (see Fig. 6a). For the third mode, the gravity modes at these smaller scales are of high frequency and of shorter vertical scale. Non-linear effects of the gravity waves interacting with the topography can become significant. Also in the boundary zone, where there was no special smoothing of the topography, the divergence forced by the topography for these modes can get quite large. Then the errors in the computed boundary divergence can be large also. To test the latter, the initialization is repeated for two cases with the topography on the GALE grid smoothed in a five degree boundary zone, as outlined in the beginning of section 4d (see Fig. 6c). In Fig. 12c we compare the changes in the amplitude of the mass divergence when the unsmoothed (Fig. 6b) and the

smoothed topography (Fig. 6c) are used for a typical example (such as for the analysis on 12Z January 23, 1986) and for an extreme example with much larger changes at higher iterations (for 12Z January 24). In both cases, the changes in the mass divergence decrease much more rapidly when the topography is smoothed in a five degree boundary zone.

For the smaller GALE grid, the initial sea level pressure and wind field in the upper troposphere at sigma level $\sigma = 0.25$ for 12Z January 23, 1986 is shown in Fig. 13a and b. A front is shown moving off the east coast of the U.S. with high pressure dominating the eastern half of the U.S. A strong jet streak is leaving the domain at the north-east corner of the domain and a minor short wave trough with its associated jet maximum is located on the Gulf of Mexico. The surface pressure changes, shown in Fig. 13c are small, being at

TABLE 5: The mean mass divergence and vorticity on the sigma surfaces of the model for the GALE grid, averaged for the week of 12Z January 23 to 12Z January 29, 1986.

Mode No.	Mass Divergence (dynes cm^{-2} s^{-1})	Vorticity (dynes cm^{-2} s^{-1})
1	7.53	92.17
2	8.12	39.21
3	15.11	42.80
4	10.05	37.65
5	9.17	19.48
6	6.73	12.05
7	4.79	7.96
8	3.84	5.72
9	2.74	4.32
10	1.72	2.51

most a mb. In this GALE domain, the western boundary is at about 1 km, sloping down to 500 to 250 meters within 5 degrees in from the boundary (Fig. 6b). The topographic features in the domain produce a strong signal in the vertical motion field shown in Fig. 13d. The increasing westerly shear with height at the western boundary and in the lee of the Appalachians, produces strong rising motion in sigma coordinates. Away from the influences of sloping sigma surfaces over the topography, sinking motion is observed in the high pressure along the Mississippi river valley and rising motion on the south side of the jet axis off the east coast. Qualitative agreement is found with the vertical motion field produced for the larger US domain. When the smoother topography in the boundary zone (see Fig. 6c) is used, the large noisy values in the vertical motion along the northern boundary and south-west corner (seen in Fig. 13d) are removed, while the interior remains unchanged (see Fig. 13e). The strong signal remaining in the vertical motion field along the western boundary, due to the high gradients in the topography there, demonstrates the importance of the specification of accurate boundary conditions used for the solution of the divergence changes in the initialization procedure. For this case the resulting changes in the geopotential and wind and temperature changes at σ =0.25 are shown in Fig 14. In the upper troposphere, the resulting rms changes in the wind components are about 1 m s^{-1}, while the rms temperature changes are about 0.5°C. In the vertical, the variation of the rms changes in the wind components and temperature with each iteration is similar to that shown for the US grid in Fig. 11, decreasing with increasing number of iterations. Three iterations are sufficient for the changes in the wind and temperature to be very small.

5. MODEL INTEGRATIONS WITH STATIC INITIALIZATION

To test the effect of the split-explicit time integration scheme in smoothing the unwanted high frequency oscillations in the NRL model, the model is integrated on the GALE grid with uninitialized data both with the split-explicit scheme described in section 2.2 and with an explicit time integration scheme of smaller time steps. Integrations with varying degrees of static initialization are then compared in three other experiments. Time series of the surface pressure and the vertical motion $\dot{\sigma}$ in sigma coordinates at selected points on the GALE grid were compared in the five experiments, which are listed in Table 6. The NMC 2.5 degree hemispheric analysis for 12Z January 23, 1986 is used to start the integrations for each of the experiments. This is a case of a cold-air damming and coastal front event, which occurred from January 23-25, 1986, during GALE. The GALE grid covers a domain from 22.5°S to 47.5°N in latitude and 102.5°W to 57.5°W in longitude, with 0.5 degree horizontal resolution.

For the experiments here, the Perkey Kreitzberg lateral boundary formulation, described in section 2.3a is used. To provide the boundary tendencies for each of the experiments, the non-divergent wind is computed for

TABLE 6: Experiments with Static Initialization on GALE grid.

1A Explicit Integration with uninitialized initial state using leapfrog scheme with a 2 Δt time step of 60 secs.

1B Split-Explicit Integration with uninitialized initial state, using a 2 Δt time step of 300 secs.

1C Split-Explicit integration with Non-divergent Initial State, using a 2 Δt time step of 300 secs.

1D Split-Explicit integration with Static Non-linear Mass Balance, using a 2 Δt time step of 300 secs.

Supplementary experiment:

1C' Same as 1C, but with boundary tendencies computed from non-divergent wind and observed temperatures.

each of the 12 hourly NMC analyses, the fields interpolated to the sigma coordinates of the model and a statically balanced temperature computed as outlined in section 3.2. Initial boundary values and 12 hour tendencies are then extracted for the 5 point boundary zone, defined in section 2.3a. To provide the same boundary values in each of the experiments, the initial fields for each experiment are merged with the statically balanced fields in the boundary zone, using the linear function α defined by Eq. (2.19). That is, we multiply the initial fields by $(1-\alpha)$ and add α times the statically balanced fields in the boundary zone.

5.1 Damping by Split-Explicit Scheme

In expt 1A, the model is integrated in time with a conventional leapfrog scheme for 12 hours with a 2 Δt time step of 60 s starting from uninitialized data. Oscillations of surface pressure of as much as 5 to 8 mb of amplitude and periods of 1 to 2 hours are observed in the first 12 hours of integration. Curve A in Fig. 15a shows these typical oscillations in the surface pressure at a grid point at 90°W and 35°N in the western half of the domain. Curve A in Fig. 15b shows the vertical motion $\dot{\sigma}$ interpolated to a sigma level at $\sigma = 0.5$, for the same grid point. The curve A shows a typical rapid adjustment (increase in this figure) in the first 6 of the integration with smaller oscillations of periods of 2 to 4 hours superimposed. The higher frequency oscillations in surface pressure are largely due to the barotropic external gravity mode while the adjustment and oscillations in the vertical motion in the middle troposphere are largely due to the internal gravity modes.

In expt 1B, the model is integrated for 48 hours with the split-explicit scheme using a 2 Δt time step of 300 s starting again from the same uninitialized data. For the first hour or so the oscillations in the surface pressure (Curve B in Fig. 15a) are the same as in the explicit integration. However the oscillations are strongly damped in the next three hours of integration. Little difference is noticed in Fig. 15b in the variation of $\dot{\sigma}$ at $\sigma = 0.5$ between the explicit (Curve A) and split-explicit (Curve B) integrations. One can conclude that the split-explicit integration scheme acts to reduce the amplitude of the unwanted external gravity waves in the first three to four hours of integration.

5.2 Non-Divergent and Statically Balanced Initial Fields

As outlined in section 3.1, the analyzed vorticity on pressure surfaces is used to first calculate the non-divergent component of the wind. A first guess of the surface pressure and temperature is found by interpolation to the model topography. The non-divergent wind, analyzed temperature and humidity are then interpolated to the model sigma levels. The initial and non-divergent wind fields at 1000 mb and 500 mb were compared in Fig. 4. In expt 1C, a 48 hour integration using the split-explicit scheme is then performed with this data. As shown by Curve C in Figure 16a, the amplitude of the initial oscillations of the surface pressure are reduced to 2 to 3 mb and are largely damped out after 3 hours. Oscillations in the surface pressure of a mb can be still seen at a grid point at 83°W and 35°N (not shown) over the Appalachian mountains. Curve C in Figure 16b shows that the strong adjustment (increase) in the vertical motion $\dot{\sigma}$ is still present in the first 6 hours and the superimposed higher frequency oscillations are only slightly reduced in amplitude. By removing the divergent component of the wind from the analyzed data the initial value of the vertical motion is also reduced. On sigma surfaces over sloping topography, a vertical shear of the non-divergent wind will introduce divergence on the sigma surfaces, as will errors caused by vertical interpolation. By largely removing the horizontal divergence we have essentially removed the external gravity mode after three hours of integration.

In a supplementary experiment 1C', boundary tendencies are computed from analyzed temperatures and the non-divergent winds on pressure surfaces, instead of from statically balanced temperatures. For initial conditions, the analyzed temperatures and winds are interpolated to the sigma coordinates without merging the statically balanced temperatures in the boundary zone. The integrations in this case were largely indistinguishable from those expt 1C. Since in the PK scheme, we damp only the tendencies in the boundary zone, initial differences in the boundary zone in the two cases are damped, leading to similar integrations. Little difference was also found in the integrations if the mass divergence is removed from the initial fields on the sigma surfaces instead of on the pressure surfaces.

A static initialization of the mass field is performed using the non-linear mass balance equation in sigma coordinates, as outlined in section 3.2. The non-linear balance equation is used to derive a balanced geopotential and temperature field from the non-divergent wind field. In Fig. 4 we showed the initial and balanced temperature fields interpolated to the 1000 mb pressure level. As mentioned in section 3.3, the balanced temperature field is much smoother than the initial field, due to the smoothing of the Laplacian operator. In expt 1D, a 48 hour integration was carried out starting from this statically initialized data. The oscillations in the surface pressure, shown in Curve D of Figure 16a, are of the same amplitude as in the non-divergent case (Curve C in Fig. 16a), being damped after 3 hours of integration. However, a small mean drift of about a mb is seen to develop in the surface pressure (curve D) during the 12 hours of integration. Again oscillations of surface pressure of a mb still remain over the Appalachian mountains. The vertical motion shown in curve D of Figure 16b still shows the rapid adjustment (increase) during the first 5 hours, but the higher frequency oscillations are much reduced in amplitude and mostly eliminated after 4 hours of integration. The non-linear balance of the mass field essentially removes the internal gravity waves except for the initial adjustment in the first 4 hours.

When using the split-explicit scheme and starting from uninitialized or initialized data, the 12 to 48 hour forecasts are very similar. Even in expt 1D, where the static initialization had smoothed out the initial temperature gradient along the front (see Fig. 4), the model regenerates the temperature gradient and intensifies it further in the first 12 hours. As an example, we show in Fig. 17, the variation of the surface pressure and the vertical motion at a grid point in the second twelve hours of integration for expts 1B, 1C and 1D. In the case of expts 1B and 1C, the variation in the surface pressure is much the same. Since the same boundary values and tendencies were used in the three expts (expts 1B, 1C and 1D), we see that the drift in the surface pressure, produced by the static initialization, is eliminated in the second twelve hours. Only in the case of expt 1A, with a 12 hour explicit time integration with uninitialized data, are high frequency oscillations in the surface pressure and vertical motion still substantial after 12 hours of integration, producing more noticeable differences in the 12 hour forecast.

6. MODEL INTEGRATIONS WITH VERTICAL MODE INITIALIZATION

To assess the effect of the vertical mode initialization procedure in removing the high frequency gravity wave oscillations, the NRL model is integrated starting from initialized and uninitialized data, for the two different US and GALE grids of differing domain size and horizontal resolution. The influence of two different lateral boundary treatments, namely the tendency relaxation scheme of Perkey and Kreitzberg (PK) and the Davies relaxation scheme, is also investigated. The experiments are summarized in Table 7. As described in section 2.3, model computed tendencies are relaxed to specified boundary tendencies in a boundary zone of 5 points at each time step in the PK scheme. The 12 hourly boundary tendencies, derived from the NMC hemispheric analyses interpolated to the model grid. In the Davies scheme, large scale boundary values are computed by linear interpolation from 12 hourly values, derived from NMC analyses, which have been interpolated to the model grid. The computed model variables are then relaxed to the boundary

TABLE 7: Experiments with Vertical Mode Initialization.

US GRID (with a 2 Δt time step of 400 secs):

2B 24 Hour integration with uninitialized initial state, using PK lateral boundary scheme.

2C 24 Hour integration with initialized initial state, using PK lateral boundary scheme.

2E 24 Hour integration with initialized initial state, using Davies lateral boundary scheme.

GALE GRID (with a 2 Δt time step of 100 secs):

3B 12 Hour integration with uninitialized initial state, using PK lateral boundary scheme.

3C 12 Hour integration with initialized initial state, using PK lateral boundary scheme.

3D 12 Hour integration with uninitialized initial state, using Davies lateral boundary scheme.

3E 12 Hour integration with initialized initial state, using Davies lateral boundary scheme.

values themselves at each time step in a boundary zone of 6 points. For integrations with initialized fields, the analyzed fields interpolated to the model grid are also initialized to provide balanced boundary values and tendencies. In this way we prevent a lot of noise propagating from the boundary into the interior of the model domain, which could contaminate the results. On the two grids, the smoothed topography, as shown in Fig. 6 is used for the integrations.

6.1 Integrations on the US grid

In the first three experiments listed in Table 7, we compare 24 hour integrations with initialized and uninitialized initial conditions on the US grid, using the two different lateral boundary treatments. The split-explicit integration scheme is used in each case with a 2 Δt time step of 400 seconds. In expt 2B, the PK tendency relaxation scheme is used for the lateral boundary treatment with uninitialized initial conditions. The 12 hourly boundary tendencies are derived from the uninitialized analyzed fields. Initial oscillations of nearly 8 mb in the surface pressure, caused by the uninitialized initial conditions, are damped by the split-explicit scheme in the first 6 hours or so, as was shown in section 5.1. As an example, curve B in Figs. 18a and b shows the variation of the surface pressure with time at a grid point at 90°W and 35°N on the US grid. In expt 2C, initialized initial conditions are used with the PK lateral boundary scheme. The boundary tendencies in this case are derived from initialized NMC analysis fields. With initialized initial conditions, the high frequency oscillations are almost completely removed, even over high topography such as the Rocky Mountains. An example with the surface pressure can be seen with curve C in Figs. 18a and b. Large high frequency oscillations in the vertical motion are also eliminated for the interior grid points, as can be seen in Figs. 18c and d. Even though both expts 2B and 2C used somewhat different boundary conditions (uninitialized values versus initialized values) no mean drift was produced. In the boundary zone, the difference seen between the results in expt 2B and that in expt 2C, is due to gravity waves, which are damped in time by the PK scheme.

In expt 2E, the Davies scheme is used with initialized initial conditions. As can be seen by Curve E in Fig. 18, use of the Davies scheme produces a similarly smooth integration of the surface pressure and the same variation in the vertical motion. However, the variation of the surface pressure with time in this case does differ somewhat after 4 hours from that found with the PK tendency relaxation scheme. The PK scheme produced some artificially larger vertical motions at the first grid point inside the boundary. The time variation of the surface pressure and vertical motion at a grid point in the boundary zone, at a distance of three times the grid spacing in from the boundary, is shown in Fig. 19. A linear variation of the surface pressure is seen with time in the boundary zone when the Davies scheme is used. With the PK scheme oscillations of long period of about 12 hours can be seen in the surface pressure and the vertical motion. The variation of the vertical motion is small for the Davies scheme at this point. This noise, generated by the PK scheme in the boundary zone, may have propagated into the interior to cause the differences seen in the integrations after 4 hours. The difference can be seen (in Fig. 18b for example) as a low amplitude oscillation of long period at 12 to 24 hours integration. However little overall differences can be seen in the 12 and 24 hour forecast fields between each of the experiments.

6.2 Integrations on the GALE grid

A series of four integrations are conducted on the GALE grid with uninitialized and initialized initial conditions with the two lateral boundary schemes (see last four experiments listed in Table 7). In each case, the split-explicit scheme is used for time integration with a 2 Δt time step of 200 seconds. For the cases with initialized initial conditions, 12 hourly boundary values and tendencies are computed from the NMC analyzes, interpolated to the model grid and then initialized. The integrations with initialized initial conditions, expts 3C and 3E, essentially remove the high frequency oscillations. As an example in Fig. 20, we show the variation of surface pressure and the vertical motion in the middle troposphere at two grid points on the GALE grid for the different integrations with initialized and uninitialized initial conditions. The grid point at 90°W and 35°N is in the western half of the domain, while the grid point at 83°W and 35°N lies on the top of the Appalachian Mountains. With the PK lateral boundary scheme,

oscillations of a mb or so are seen during the integration period when uninitialized initial conditions are used (Curve B). With initialized initial conditions obtained with the vertical mode scheme, the oscillations are removed except for an initial hump of 0.5 mb in the surface pressure seen after the first two hours of integration (Curve C). With the Davies scheme and initialized initial conditions, a smoother variation of the surface pressure is seen (Curve E). The rapid initial adjustment in the vertical motion has been largely removed, leaving a slower increase in the vertical motion with time.

In expt 3D, the Davies scheme for the lateral boundary treatment is used with uninitialized initial conditions. A different response is produced in the surface pressure, while the response in the vertical motion field is similar to the PK scheme for grid points in the interior of the domain. In Fig. 21, we compare the surface pressure variation and vertical motion in the middle troposphere at our two grid points for initialized and uninitialized initial conditions, when the Davies scheme is used. In the case of the Davies scheme with uninitialized initial conditions, an initial shock of large amplitude is seen in the surface pressure (curve D in Figs. 21a and b), which is rapidly damped in the first 4 hours or so. The scheme acts to damp any gravity waves that propagate into the boundary zone from the interior. Using initialized initial conditions, this initial shock is eliminated (curve E in Figs. 21a and b). With time, the integrations in the first 12 hours differ by as much as a mb or so in expts 3D and 3E (see Fig. 21). The difference is explained by the fact that in expt 3D, we force uninitialized boundary values in the boundary zone, and the model solution in the interior is forced to adjust in the first three of four hours of integration.

In the boundary zone large differences are found when using the different boundary treatments. In Figs. 22a and b, we show the variation of the surface pressure at two grid points in the boundary zone for the different lateral boundary treatments. The grid point at 59°W and 40°N lies a distance of three grid lengths from the lateral boundary (at 57.5°W), while the grid point at 58°W and 40°N is a distance of one grid length. With the Davies scheme, the boundary values are strongly forced in the boundary zone, which is reflected in the linear variation in the surface pressure in the boundary zone (see

curve E in Figs. 22a and b, for example). With the PK scheme, oscillations in the surface pressure, with an amplitude of one to two mb and period of about twelve hours, can be seen in the boundary zone (see curve C in Fig. 22a and b). The two schemes also differ in their response in the vertical motion in the boundary zone. With the PK scheme, the vertical motion piles up at the first grid point in from the boundary, while with the Davies scheme, larger vertical motions are found in the zone between the interior region and the boundary zone. The variation of the vertical motion at the two grid points in the boundary zone is shown in Figs. 22c and d. Using the Davies scheme, curve E in Fig. 22c shows a slow increase of the vertical motion to 20×10^{-3} hr^{-1}, for the grid point which is a distance of three grid lengths in from the lateral boundary. In Fig. 22d, curve E shows a slower linear variation of the vertical motion, increasing to 10×10^{-3} hr^{-1}, at the grid point one grid length from the boundary. With the PK scheme low amplitude changes in the vertical motion occur at the boundary between the boundary zone and the interior (see curve C in Fig. 22c), while unrealistically large values of 30×10^{-3} hr^{-1} are reached in the vertical motion at the grid point lying a distance of one grid length in from the lateral boundary (see curve C in Fig. 22d). In Fig. 23, we compare the surface pressure variation and vertical motion in the middle troposphere at our two grid points in the boundary zone for initialized and uninitialized initial conditions, when the Davies scheme is used. The boundary values are again strongly forced in the boundary zone in both cases. The initial shock in the surface pressure variation in curve D, in Fig. 23a, is eliminated by the initialization (curve E).

7. SUMMARY AND CONCLUSIONS

To remove the high frequency gravity wave oscillations, various initialization procedures have been tested for use with the Naval Research Laboratory limited area numerical weather prediction model. Operational analyses obtained from the National Meteorological Center (NMC) for the period of the second intensive observing period of the GALE experiment are used to test the procedures and provide initial and boundary conditions for model integrations. The model is integrated with initial conditions with varying degrees and type of initialization on two different model grids, one a low resolution grid of 2° longitude by 1.5° latitude covering the continental U.S. (US grid) and the other a higher resolution grid of 0.5° in latitude and longitude covering the eastern U.S. (GALE grid). The influence of two different lateral boundary treatments, namely the tendency relaxation scheme of Perkey and Kreitzberg (PK) and the Davies relaxation scheme, are compared. For integrations with initialized fields, the NMC analyzed fields interpolated to the model grid are also initialized to provide balanced boundary values and tendencies. This reduces noise in the boundary zone, which can propagate into the interior of the domain and contaminate our test.

In the static initialization procedure, the non-divergent wind is first computed for the analyzed winds on the pressure surfaces, by solving for the streamfunction. The non-divergent wind and the analyzed temperatures are then interpolated to the sigma coordinates of the model. A diagnostic relation is then derived for the geopotential on the sigma surfaces of the numerical model, by ignoring the tendency of divergence, non-linear vertical advection and friction. The initial non-divergent wind and analyzed temperatures, interpolated to the sigma surfaces are used to compute the non-linear forcing terms. With the tangential wind defined along the model lateral boundary with the C grid, consistent boundary conditions for the normal derivatives of the geopotential are easily obtained by ignoring the tendencies in the momentum equations.

The NRL model uses the split-explicit scheme to integrate in time. The scheme is compared to a centered difference scheme by integrating the model on the GALE grid. The split-explicit scheme has been shown to reduce the

amplitude of the unwanted external gravity wave oscillations in the first three to four hours of integration. However, a typical rapid adjustment with superimposed oscillations occurs in the mid-troposphere vertical motion in the first 4 to 6 hours of integration. The new static initialization procedure is also tested on the GALE grid. By interpolating the non-divergent wind and analyzed temperature to the model sigma surfaces, the amplitude of the initial oscillations of the surface pressure are reduced to 2 to 3 mb and are largely damped out after 3 hours. Using the non-divergent wind and performing a static non-linear balance of the mass field, provides a balanced initial state, except for a smooth initial adjustment of the vertical motion in the first five hours or less of integration and a small mean drift in the surface pressure. For the varying degrees of static initialization, similar 12 to 48 hour forecasts are produced when the split-explicit scheme for time integration was used.

A vertical mode initialization scheme following that of Bourke and McGregor (1983) has been developed for use with the NRL model. Filtering conditions are applied to the model dynamical equations to derive to linear diagnostic equations for the mass divergence and geopotential, which are solved iteratively for the first three vertical modes of the numerical model. These modes have phase speeds which are much faster than those of meteorological systems. The further condition that the linearized potential vorticity is unchanged by the procedure is required to compute the vorticity. The observed wind and temperature is first interpolated to the sigma surfaces of the model. The iterative procedure is then used to compute incremental changes to the generalized geopotential, mass divergence and vorticity for the first three vertical modes of the numerical model. As is customary, we keep the geopotential, temperature and pressure fixed at the lateral boundaries in the scheme. To provide a boundary condition for the divergence however, an approximate divergence at the boundary is computed using the thermodynamic equation. In our scheme, changes in the tangential wind along the lateral boundaries are consistent with the changes in the vorticity and mass divergence computed. The procedure provides a balanced vertical motion field and produces smaller changes to the initial mass and wind fields, compared to the static initialization. The scheme is tested on two grids, of differing domain size and grid resolution. Convergence of the scheme is rapid with the

lower resolution US grid, with three iterations of the scheme being sufficient for convergence. With the smaller GALE grid of higher resolution and sloping topography along two boundaries, the convergence of the scheme is slower and in fact the mass divergence didn't converge for the third mode. However, by smoothing the topography in a boundary zone of five degrees, the convergence of the scheme is much improved. In both cases, changes in the mass and wind fields are still small after three iterations.

Integrations with initial conditions, initialized with the vertical mode initialization procedure, prevent gravity wave oscillations, without producing a mean drift in the surface pressure, and provide a balanced vertical motion field. On the coarse US grid, little difference is found between integrations using either of the lateral boundary treatments. However, some low amplitude oscillations in the surface pressure of long period remain in the interior of the domain and some noise is generated in the vertical motion at the lateral boundaries when the Perkey Kreitzberg scheme is used. On the smaller GALE grid, some noise is produced in the vertical motion in the boundary zone by both schemes. In the interior, the Davies scheme produces a smoother variation of the surface pressure. When the Davies scheme is used with integrations starting from uninitialized data and boundary values, an initial shock in the surface pressure is damped in the first four hours. However a small drift in the surface pressure is produced. This indicates that the boundary values used with the Davies scheme should be as balanced as possible for the numerical model, being initialized or derived from integrations on a larger grid or with another model. Similar 12 to 48 hour forecasts are again produced with the various experiments.

For grids of high resolution such as our GALE grid, and especially when fine scale topography is used along the boundary, it is recommended that no more than three iterations of the vertical mode scheme should be used in practice. For grids of even higher resolution, only the first two modes may be able to be initialized, with possibly no more than three iterations used with the scheme. Some improvement however, can be expected by smoothing the topography in the boundary zone or using a nested model to provide more accurate boundary values for the mass divergence for the inner nested grids.

ACKNOWLEDGEMENTS

The first author was supported under contract number N00014-86-C-2365 with NRL and the second author was supported by SPAWAR and NRL's basic research program. Preliminary results were described by Sashegyi et al. (1987) in the Proceedings of the IAMAP Symposium on Mesoscale Analysis and Forecasting, held 17-19 August 1987 in Vancouver, Canada and by Sashegyi and Madala (1988) in the preprints volume of the Eight Conference on Numerical Weather Prediction, which was held 22-26 February 1988 in Baltimore, Maryland.

APPENDIX: SPLIT-EXPLICIT SCHEME

The model equations in matrix notation can be written

$$\frac{\partial \overline{p_s^x} u}{\partial t} + \delta_x \Phi = A_u \tag{A1}$$

$$\frac{\partial \overline{p_s^y} v}{\partial t} + \delta_y \Phi = A_v \tag{A2}$$

$$\frac{\partial p_s T}{\partial t} + M_2 D = A_T \tag{A3}$$

$$\frac{\partial p_s}{\partial t} + N_2^T D = 0 \tag{A4}$$

$$\frac{\partial p_s q}{\partial t} = A_q \tag{A5}$$

$$\phi - \phi_s = M_1 T \tag{A6}$$

where the variables are defined in section 2.1, and the non-linear, Coriolis, friction and diabatic terms are included in the terms on the right hand sides of the equations. Integrating (A1), (A2), (A3), (A4) and (A5) over a time step $2\Delta t$ we obtain

$$\overline{p_s^x} u(t+\Delta t) - \overline{p_s^x} u(t-\Delta t) + 2\Delta t\, \delta_x \bar{\Phi} = 2\Delta t\, \bar{A}_u \tag{A7}$$

$$\overline{p_s^y} v(t+\Delta t) - \overline{p_s^y} v(t-\Delta t) + 2\Delta t\, \delta_y \bar{\Phi} = 2\Delta t\, \bar{A}_v \tag{A8}$$

$$p_s T(t+\Delta t) - p_s T(t-\Delta t) + 2\Delta t\, M_2 \bar{D} = 2\Delta t\, \bar{A}_T \tag{A9}$$

$$p_s(t+\Delta t) - p_s(t-\Delta t) + 2\Delta t\, N_2^T \bar{D} = 0 \tag{A10}$$

$$p_s q(t+\Delta t) - p_s q(t-\Delta t) = 2\Delta t\, \bar{A}_q \tag{A11}$$

where the averages $\bar{\alpha} = \frac{1}{2\Delta t} \int_{t-\Delta t}^{t+\Delta t} \alpha \, dt$ (A12)

and $\overline{p_s^x}$ and $\overline{p_s^y}$ represent grid point averages as defined in section 2.1. The non-linear and Coriolis terms on the right hand sides are slowly varying so that $\bar{A}_u = A_u(t)$, $\bar{A}_v = A_v(t)$, $\bar{A}_T = A_T(t)$. For an explicit time step choosing

$\bar{\Phi} \simeq \Phi(t)$, $\bar{D} \simeq D(t)$, gives the conventional centered difference scheme for time integration. We use this explicit difference scheme to compute first estimates of the variables at time $t+\Delta t$, giving

$$\bar{p}_s^x u^{ex}(t+\Delta t) - \bar{p}_s^x u(t-\Delta t) + 2\Delta t\, \delta_x \Phi(t) = 2\Delta t\, A_u(t) \quad \text{(A13)}$$

$$\bar{p}_s^y v^{ex}(t+\Delta t) - \bar{p}_s^y v(t-\Delta t) + 2\Delta t\, \delta_y \Phi(t) = 2\Delta t\, A_v(t) \quad \text{(A14)}$$

$$p_s T^{ex}(t+\Delta t) - p_s T(t-\Delta t) + 2\Delta t\, M_2\, D(t) = 2\Delta t\, A_T(t) \quad \text{(A15)}$$

$$p_s^{ex}(t+\Delta t) - p_s(t-\Delta t) + 2\Delta t\, N_2^T\, D(t) = 0 \quad \text{(A16)}$$

$$p_s q^{ex}(t+\Delta t) - p_s q(t-\Delta t) = 2\Delta t\, A_q(t) \quad \text{(A17)}$$

Subtracting these equations from Eqs. (A7), (A8), (A9), (A10) and (A11), we can then write for the corrected variables

$$\bar{p}_s^x u(t+\Delta t) + 2\Delta t\, \delta_x[\bar{\Phi} - \Phi(t)] = \bar{p}_s^x u^{ex}(t+\Delta t) \quad \text{(A18)}$$

$$\bar{p}_s^y v(t+\Delta t) + 2\Delta t\, \delta_y[\bar{\Phi} - \Phi(t)] = \bar{p}_s^y v^{ex}(t+\Delta t) \quad \text{(A19)}$$

$$p_s T(t+\Delta t) + 2\Delta t\, M_2[\bar{D} - D(t)] = p_s T^{ex}(t+\Delta t) \quad \text{(A20)}$$

$$p_s(t+\Delta t) + 2\Delta t\, N_2^T\, [\bar{D} - D(t)] = p_s^{ex}(t+\Delta t) \quad \text{(A21)}$$

$$p_s q(t+\Delta t) = p_s q^{ex}(t+\Delta t) \quad \text{(A22)}$$

where the terms on the right-hand side are the explicit computations of the variables. We only need to compute the corrections $\bar{\Phi} - \Phi(t)$, $\bar{D} - D(t)$ for those vertical modes whose phase speeds relative to the ground $U + \sqrt{\lambda_k}$ are greater than $\Delta x/(2\Delta t)$, where U is the maximum background flow speed. It can also be noted that the specific humidity q need not be corrected. To obtain the corrections for these modes, the amplitudes of the deviations $\Phi - \Phi(t)$, $D - D(t)$ are integrated at smaller time steps, over the interval of twice the large time step.

To integrate the deviations we require equations for the tendencies of mass divergence and generalized geopotential. By taking δ_x of h_y times Eq. (A1) and adding δ_y of h_x times Eq. (A2) we obtain the equation for the divergence. By taking M_1 times Eq. (A3) and adding $(RT^* + \phi^*)$ times Eq. (A4) an equation for the generalized geopotential is obtained. That is

$$\frac{\partial D}{\partial t} + \nabla^2 \Phi = A_m \tag{A23}$$

$$\frac{\partial \Phi}{\partial t} + M_3 D = M_1 A_T \tag{A24}$$

$$\text{where } A_m = \frac{1}{h_y} \delta_x (h_y A_u) + \frac{1}{h_x} \delta_y (\overline{h^y}^x A_v) \tag{A25}$$

and the two dimensional Laplacian ∇^2 is defined by Eq. (2.13) in section 2.1. In terms of our vertical modes, the amplitudes of the mass divergence and generalized geopotential are $d = E^{-1}D$, $e = E^{-1}\Phi$. The amplitudes of the deviations of the divergence $d_k^n - d_k(t)$, and the generalized geopotential $e_k^n - e_k(t)$ are integrated with smaller time steps given by $\Delta\tau_k = \Delta t/m_k$. For the ten layer model, the deviations are computed for the first three modes with m_k given by 8, 4 and 2 respectively. Now integrating over smaller time steps we have

$$d_k^{n+1} - d_k^{n-1} + 2 \Delta\tau_k \nabla^2 e_k^n = 2 \Delta\tau_k \{ E^{-1} A_m(t)\}_k \tag{A26}$$

$$e_k^{n+1} - e_k^{n-1} + 2 \Delta\tau_k \lambda_k d_k^n = 2 \Delta\tau_k \{ E^{-1} M_1 A_T(t)\}_k \tag{A27}$$

For our explicit time step, applying the centered difference scheme with time step $2\Delta t$ to Eqs. (A23) and (A24), or from Eqs. (A13), (A14), (A15), (A16) directly, we obtain

$$d_k^{ex}(t+\Delta t) - d_k(t-\Delta t) + 2 \Delta t \nabla^2 e_k(t) = 2 \Delta t \{ E^{-1} A_m(t)\}_k \tag{A28}$$

$$e_k^{ex}(t+\Delta t) - e_k(t-\Delta t) + 2 \Delta t \lambda_k d_k(t) = 2 \Delta t \{ E^{-1} M_1 A_T(t)\}_k \tag{A29}$$

By subtraction we obtain the equations for integrating the deviations $d_k^n - d_k(t)$, $e_k^n - e_k(t)$,

$$[d_k^{n+1} - d_k(t)] - [d_k^{n-1} - d_k(t)] + 2\Delta\tau_k \nabla^2 (e_k^n - e_k(t)) = \frac{1}{m_k} [d_k^{ex}(t+\Delta t) - d_k(t-\Delta t)] \quad \text{(A30)}$$

$$[e_k^{n+1} - e_k(t)] - [e_k^{n-1} - e_k(t)] + 2\Delta\tau_k \lambda_k (d_k^n - d_k(t)) = \frac{1}{m_k} [e_k^{ex}(t+\Delta t) - e_k(t-\Delta t)] \quad \text{(A31)}$$

where $d_k^{ex}(t+\Delta t) = \{E^{-1} D^{ex}(t+\Delta t)\}_k = \{E^{-1}[\delta_x(\overline{p_s}^x u^{ex}) + \frac{1}{h_x}\delta_y(\overline{h_x p_s}^y v^{ex})]\}_k$

and $e_k^{ex}(t+\Delta t) = \{E^{-1}\Phi^{ex}(t+\Delta t)\}_k$

The required corrections are then given by

$$\bar{d}_k - d_k(t) = \frac{1}{m_k} \sum_{n=1}^{m_k} (d_k^n - d_k(t)) \quad \text{(A32)}$$

$$\bar{e}_k - e_k(t) = \frac{1}{m_k} \sum_{n=1}^{m_k} (e_k^n - e_k(t)) \quad \text{(A33)}$$

For the integration of the deviations of the divergence, a lateral boundary condition is required for the generalized geopotential. The boundary value for $e_k - e_k(t)$ is computed by linear interpolation from the values at $t - \Delta t$ and t. Further pragmatic boundary conditions are provided by reducing the amplitude and phase speed of the deviations of the divergence and generalized geopotential in the boundary zone by the factor $1-\alpha$, where α is defined in section 2.3, for the two different lateral boundary formulations. That is to reduce the phase speed c_k in the boundary zone, we multiply λ_k in Eq. (A31) and the ∇^2 term in Eq.(A30) by $(1-\alpha)$. The amplitudes are reduced in the boundary zone by multiplying the correction terms in Eqs. (A20) and (A21) by $(1-\alpha)$ and those in Eqs (A18) and (A19) by $(1-\alpha_u)$ and $(1-\alpha_v)$, respectively.

REFERENCES

Andersen, J.H., 1977: A routine for normal mode initialization with non-linear correction for a multi-level spectral model with triangular truncation. ECMWF Internal Report No. 15, European Centre for Medium Range Weather Forecasts, Bracknell, U.K., 41 pp.

Arakawa, A., and V.R. Lamb, 1977: Computational design of the basic dynamical processes of the UCLA general circulation model. Methods in Computational Physics, Vol. 17, General Circulation Models of the Atmosphere, J. Chang, Ed., Academic Press, New York, 173-265.

Bengtsson, L., 1975: Four-dimensional assimilation of meteorological observations. GARP Publication Series, No. 15, World Meteorological Organization, Geneva, Switzerland, 57-69.

Bourke, W., and J.L. McGregor, 1983: A nonlinear vertical mode initialization scheme for a limited area prediction model. Mon. Wea. Rev., 111, 2285-2297.

Chang, S., K. Brehme, R. Madala, K. Sashegyi, 1989: A numerical study of the east coast snowstorm of 10-12 February 1983. Mon. Wea. Rev., 117, 1768-1778.

Daley, R., 1979: The application of non-linear normal mode initialization to an operational forecast model. Atmosphere-Ocean, 17, 97-124.

Davies, H.C., 1976: A lateral boundary formulation for multi-level prediction models. Quart. J. Roy. Meteor. Soc., 102, 405-418.

Davies, H.C., 1983: Limitations of some common lateral boundary schemes used in regional NWP models. Mon. Wea. Rev., 111, 1002-1012.

Errico, R.M., 1986: Initialization of the PSU/NCAR mesoscale model. NCAR Technical Note, NCAR/TN-270+IA, National Center for Atmospheric Research, Boulder, CO., 120pp.

Gill, A.E., 1982: Atmosphere-Ocean Dynamics. Academic Press, New York, 662pp.

Grønås, S., A. Foss and M. Lystad, 1987: Numerical simulations of polar lows in the Norwegian Sea. Tellus, 39A, 334-353.

Haltiner, G.J., and R.T. Williams, 1980: Numerical Prediction and Dynamic Meteorology. Second ed., John Wiley and Sons, New York, 477pp.

Juvanon du Vachat, R., 1986: A general formulation of normal modes for limited-area models: Application to initialization. Mon. Wea. Rev., 114, 2478-2487.

Kasahara, A., and K. Puri, 1981: Spectral representation of three-dimensional global data by expansion in normal mode functions. Mon. Wea. Rev., 109, 37-51.

Krishnamurti, T.N., 1979: Tropical Meteorology. Compendium of Meteorology for use by Class I and Class II meteorological personnel, Vol. 2, Part 4, A. Wiin-Nielsen, Ed. WMO Technical Publication, No. 364, World Meteorological Organization, Geneva, Switzerland, 428pp.

Lynch, P., 1988: Deducing the wind from vorticity and divergence. Mon. Wea. Rev., 116, 86-93.

Madala, R.V., 1978: An efficient direct solver for separable and non-separable elliptic equations. Mon. Wea. Rev., 106, 1735-1741.

Madala, R.V., 1981: Efficient time integration schemes for atmosphere and ocean models. Finite Difference Techniques for Vectorized Fluid Dynamic Calculations, D.L. Book, Ed., Chap. 4, Springer-Verlag, New York, 56-74.

Madala, R.V., 1981: Solution of elliptic equations. Finite Difference Techniques for Vectorized Fluid Dynamic Calculations, D.L. Book, Ed., Chap. 7, Springer-Verlag, New York, 117-134.

Madala, R.V., S.W. Chang, U.C. Mohanty, S.C. Madan, R.K. Paliwal, V.B. Sarin, T. Holt and S. Raman, 1987: Description of the Naval Research Laboratory Limited Area Dynamical Weather Prediction Model. NRL Memorandum Report, No. 5992, Naval Research Laboratory, Washington, D.C., 131pp.

Manabe, S., J. Smagorinsky, and R.F. Strickler, 1965: Simulated climatology of a general circulation model with a hydrologic cycle. Mon. Wea. Rev., 93, 769-798.

Matsuno, T., 1966: Quasi-geostrophic motions in the equatorial area. Jour. Meteor. Soc. Japan, Series II, 44, 25-43.

Mesinger, F., and A. Arakawa, 1976: Numerical Methods used in Atmospheric Models. GARP Publication Series, No. 17, Vol. 1, World Meteorological Organization, Geneva, Switzerland, 64pp.

Perkey, D.J., and C.W. Kreitzberg, 1976: A time-dependent lateral boundary scheme for limited-area primitive equation models. Mon. Wea. Rev., 104, 744-755.

Phillips, N.A., 1957: A coordinate system having some special advantages for numerical forecasting. Jour. of Meteor., 14, 184-185.

Reynolds, R.W., 1982: A monthly averaged climatology of sea surface temperatures. NOAA Technical Report, NWS-31, Climate Analysis Center, National Weather Service, Washington, D.C., 35pp.

Sashegyi, K.D., S.W. Chang and R.V. Madala, 1987: Preliminary results from real data experiments with the NRL mesoscale numerical model. Proceedings, Symposium on Mesoscale Analysis and Forecasting, Incorporating Nowcasting, IAMAP, Aug 17-19, Vancouver, Canada, ESA SP-282, 497-500.

Sashegyi, K.D., and R.V. Madala, 1988: Initialization experiments with the NRL mesoscale numerical model. Preprints, 8th Conference on Numerical Weather Prediction, Amer. Meteor. Soc., Feb 22-26, Baltimore, MD, 778-781.

Sashegyi, K.D., and R.V. Madala, 1989: A user's guide to the SEVP solver: An efficient direct solver for elliptic partial differential equations. NRL Memorandum Report, No. 6450, Naval Research Laboratory, Washington, D.C., 38pp.

Shapiro, R., 1970: Smoothing, filtering and boundary effects. Rev. Geophys. Space Phys., 8, 359-387.

Strang, G., 1988: Linear Algebra and its Applications. Third ed., Harcourt Brace Jovanovich, San Diego, CA., 505pp.

Sundqvist, H., 1975: Initialization for models using sigma as the vertical coordinate. Jour. Appl. Meteor., 14, 153-158.

Temperton, C., 1984: Orthogonal vertical modes for a multilevel model. Mon. Wea. Rev., 112, 503-509.

Temperton, C., 1988: Implicit normal mode initialization. Mon. Wea. Rev., 116, 1013-1031.

Temperton, C., and D.L. Williamson, 1981: Normal mode initialization for a multilevel grid-point model. Part I: Linear aspects. Mon. Wea. Rev., 109, 729-743.

Williamson, D.L., and C. Temperton, 1981: Normal mode initialization for a multilevel grid-point model. Part II: Nonlinear aspects. Mon. Wea. Rev., 109, 744-757.

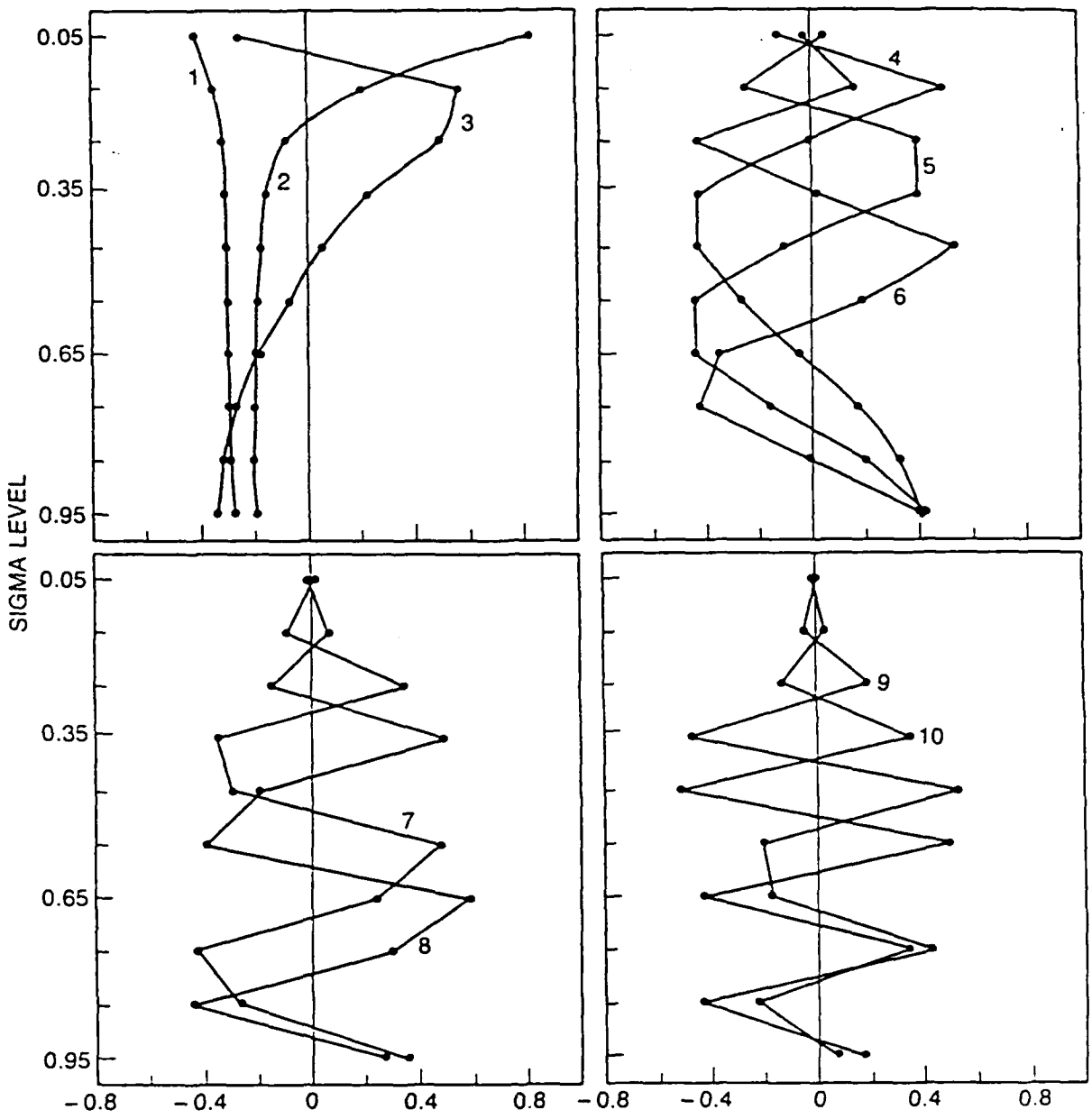

FIG. 1. The vertical structure of the modes versus sigma level in a ten layer model for the case of a basic state at rest with the mean temperature profile defined in Table 1.

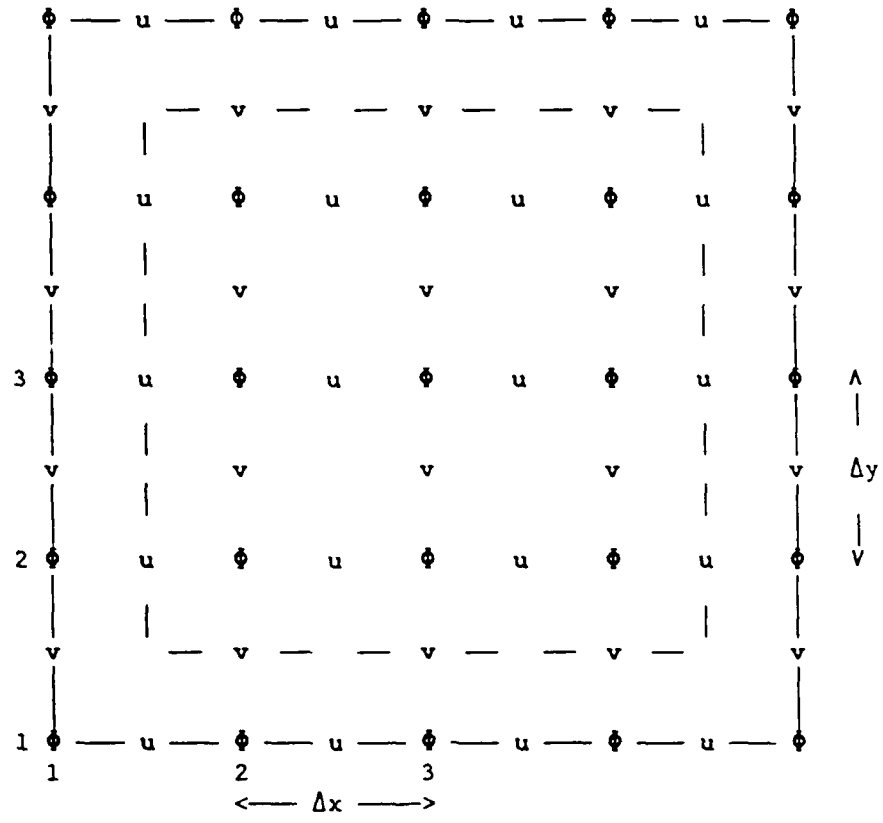

FIG. 2. The horizontal grid stencil for the Arakawa C grid as applied to the NRL model, showing the lateral boundary grid points. u and v represent the horizontal wind components. The surface pressure p_s, the temperature T, the geopotential ϕ, specific humidity q, the mass divergence D and vertical motion $\dot{\sigma}$ are defined at the same horizontal grid point as the generalized geopotential Φ.

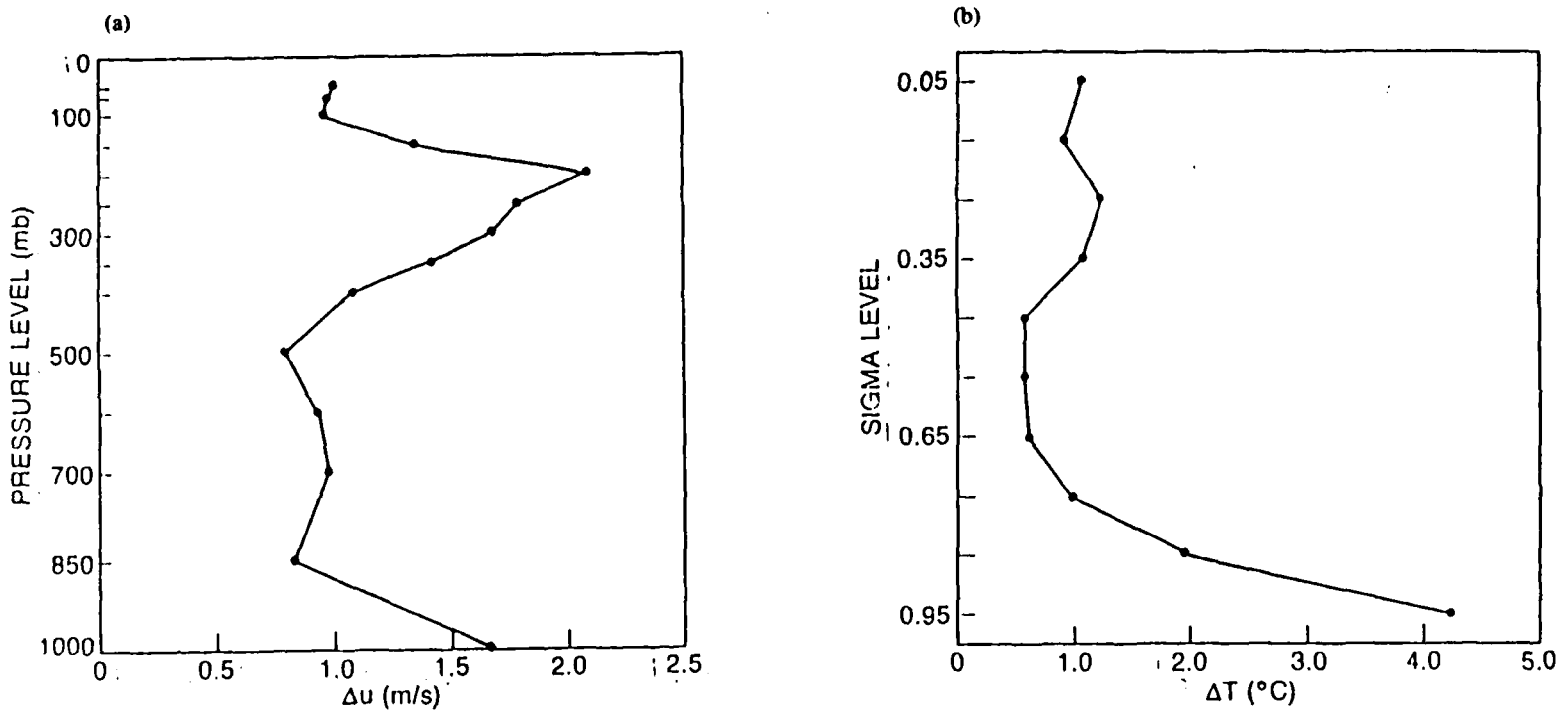

FIG. 3. The root-mean-square changes for 12Z January 23, 1986 on the GALE grid in (a) the u-component of the analyzed wind as a result of computing the non-divergent wind and (b) the root-mean-square changes in the analyzed temperature after the non-linear mass balance equation is used to replace the temperature.

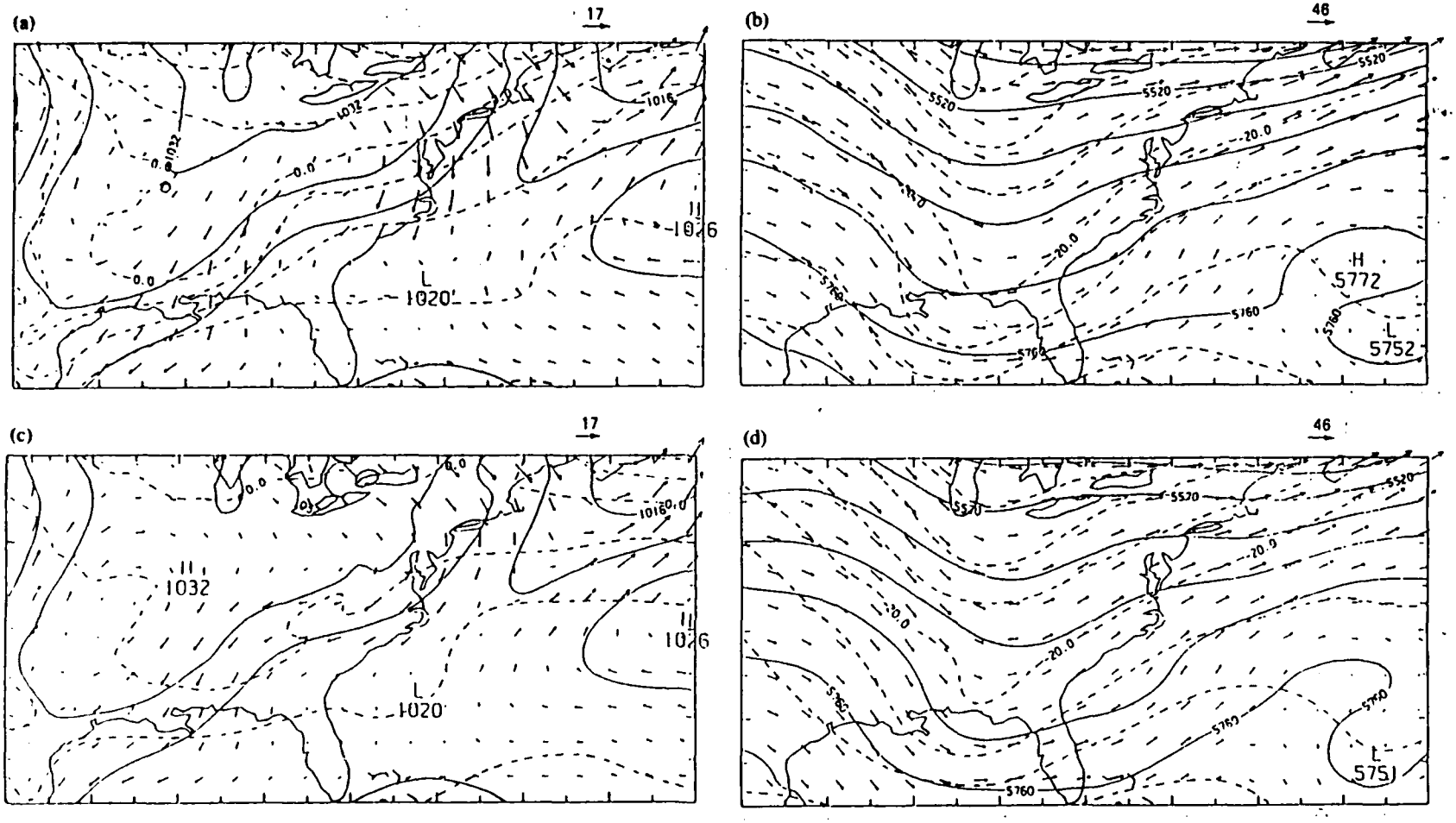

FIG. 4. (a) The analyzed sea-level pressure, wind and temperature at 1000 mb on the GALE grid for 12Z January 23, 1986. The contours of sea-level pressure are every 4 mb and every 5°C for the temperature. The maximum wind vector is 17 m s^{-1}. (b) The analyzed geopotential, wind and temperature at 500 mb on the GALE grid for 12Z January 23, 1986. The contours of geopotential are every 60 gpm and every 2.5°C for the temperature. The maximum wind vector is 46 m s^{-1}. The 1000 mb and 500 mb fields after static initialization are shown in (c) and (d).

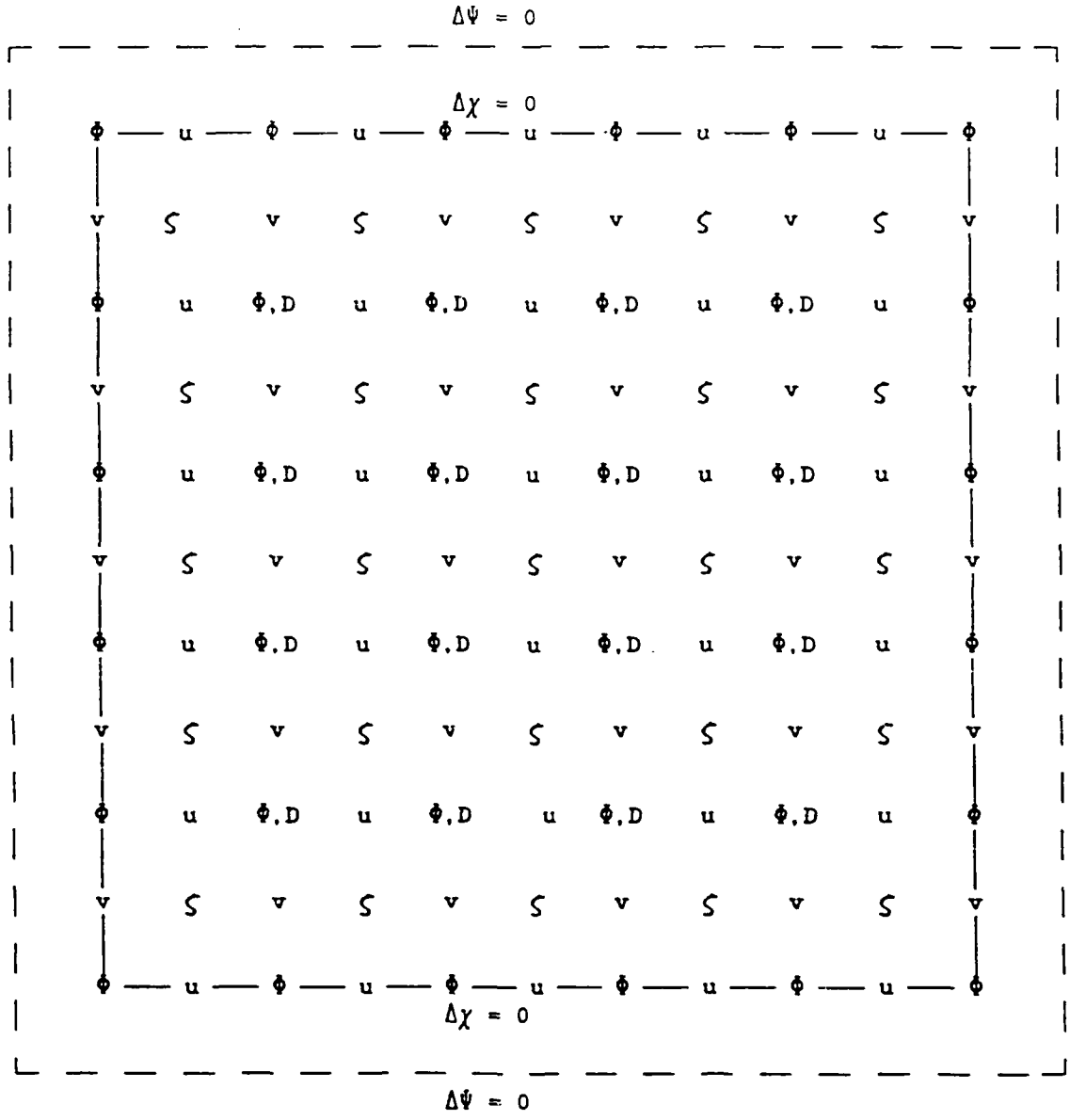

FIG. 5. The horizontal grid stencil used to compute the changes in the wind field, given the changes in the mass divergence and vorticity. The stream function change $\Delta\Psi$ is defined in the interior at the same grid point as the vorticity ζ, while the velocity potential change $\Delta\chi$ is defined at the same grid point as the mass divergence D. The lateral boundary conditions for $\Delta\chi$ and $\Delta\Psi$ are indicated.

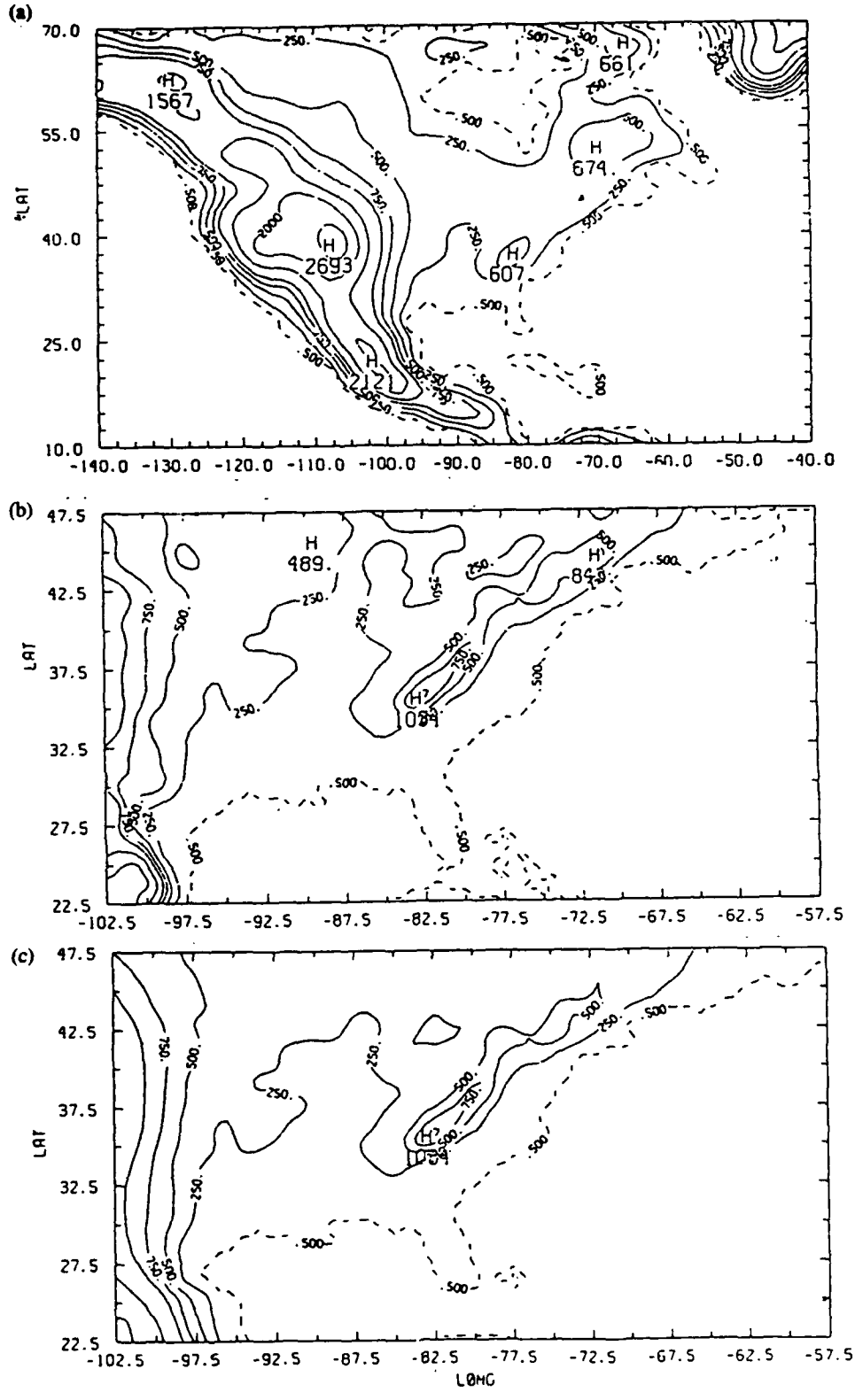

FIG. 6. The smoothed model topography for (a) the US grid, (b) for the GALE grid and (c) for the GALE grid with the topography further smoothed in a five degree zone around the lateral boundary. The horizontal resolution is 2° longitude by 1.5° latitude for the US grid and 0.5° in latitude and longitude for the GALE grid. The contour intervals are 500 m for elevations above 1000 m, and 250 m for those below 1000 m.

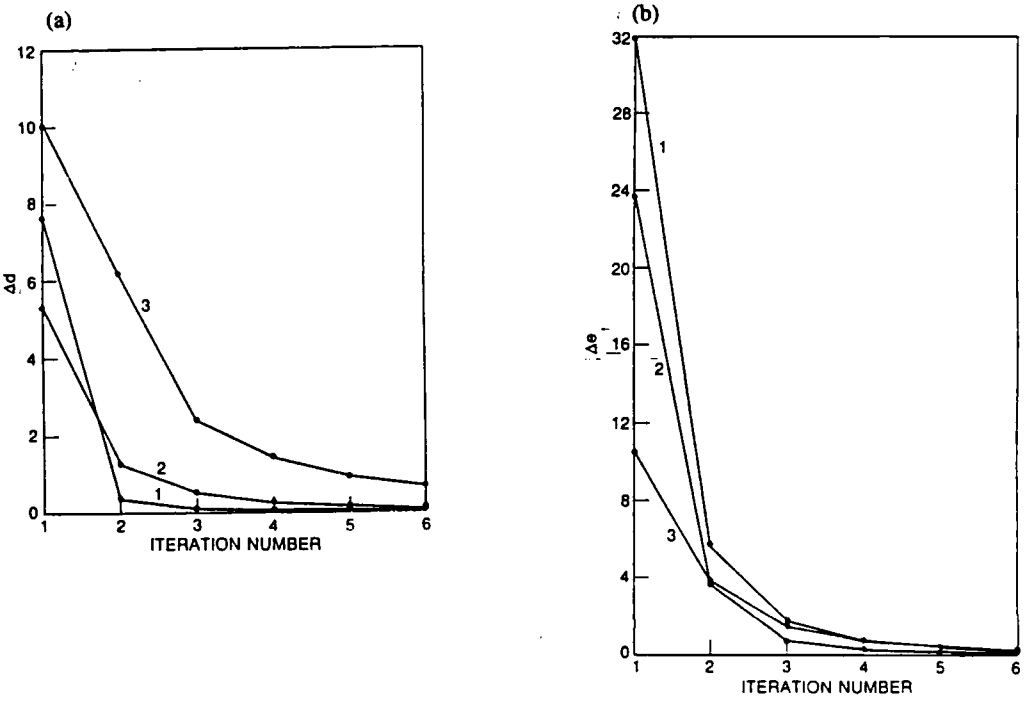

FIG. 7. The root-mean-square (rms) changes in the amplitudes on the US grid of (a) the mass divergence Δd in dynes cm^{-2} s^{-1}, (b) the generalized geopotential Δe in units of 10^{11} dynes s^{-2}, and (c) the vorticity Δv in dynes cm^{-2} s^{-1}, versus the iteration number in the vertical mode initialization scheme, for each of the first three vertical modes. In (d) is shown the rms change Δp_s in the surface pressure in mb versus the iteration number. The rms values are averaged for all the analyses of the week of 12Z January 23 to 12Z January 29, 1986. (e) The rms change in the amplitude of the mass divergence Δd in dynes cm^{-2} s^{-1} versus iteration number for the highest mode initialized, as the number of modes initialized is varied from one to six modes for the analysis on 12Z January 23, 1986 only.

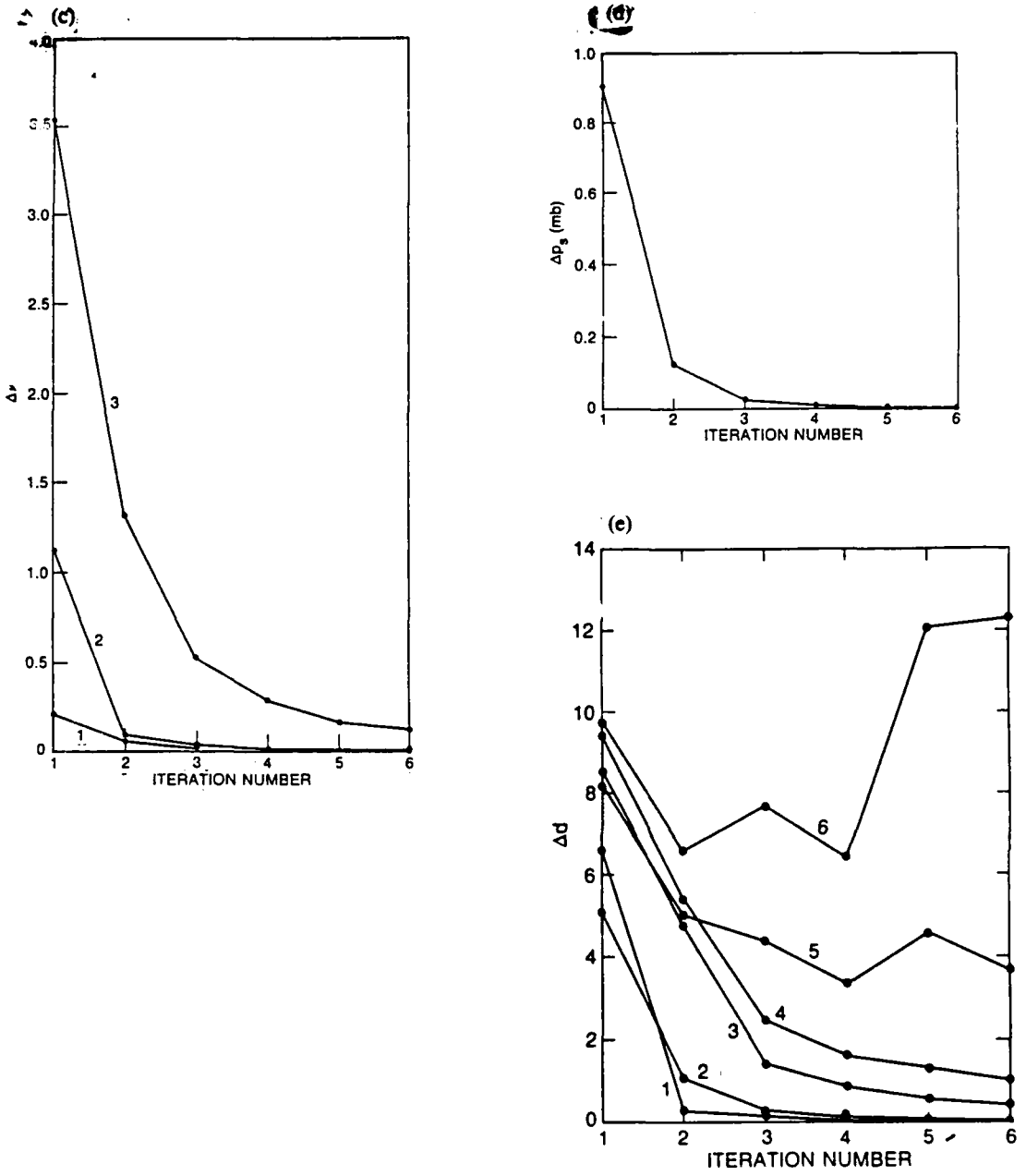

FIG. 7. The root-mean-square (rms) changes in the amplitudes on the US grid of (a) the mass divergence Δd in dynes cm^{-2} s^{-1}, (b) the generalized geopotential Δe in units of 10^{11} dynes s^{-2}, and (c) the vorticity Δv in dynes cm^{-2} s^{-1}, versus the iteration number in the vertical mode initialization scheme, for each of the first three vertical modes. In (d) is shown the rms change Δp_s in the surface pressure in mb versus the iteration number. The rms values are averaged for all the analyses of the week of 12Z January 23 to 12Z January 29, 1986. (e) The rms change in the amplitude of the mass divergence Δd in dynes cm^{-2} s^{-1} versus iteration number for the highest mode initialized, as the number of modes initialized is varied from one to six modes for the analysis on 12Z January 23, 1986 only.

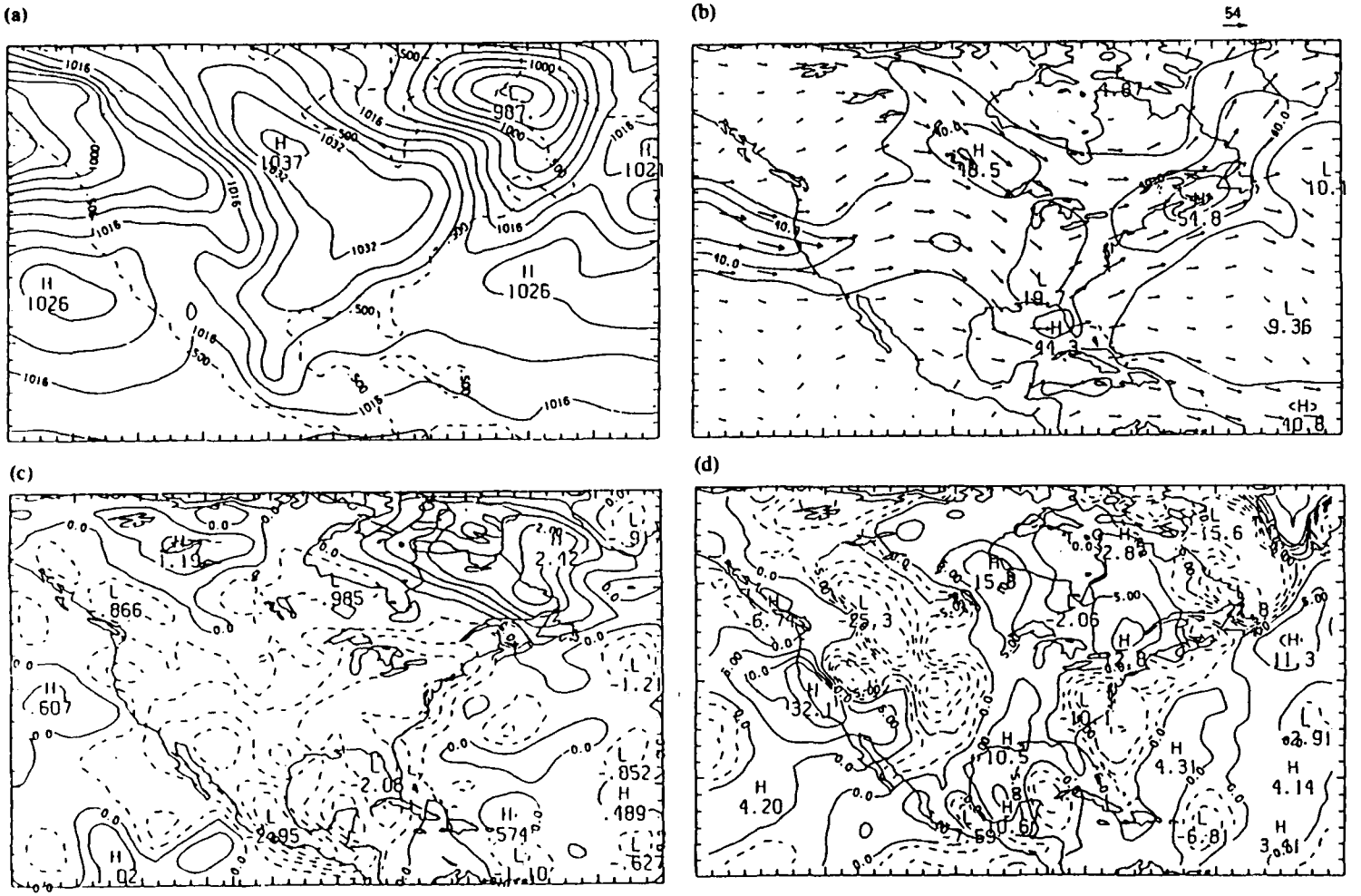

FIG. 8. The analyzed (a) sea-level pressure and (b) wind field on the US grid at model sigma level σ = 0.25 for 12Z January 23, 1986. The contours of sea-level pressure are every 4 mb and the isotachs are every 10 m s^{-1}, increasing from 30 m s^{-1}. The maximum wind vector shown is 54 m s^{-1}. (c) The surface pressure change and (d) the vertical motion field in units of 10^{-3} hr^{-1} in the middle troposphere at a sigma level σ = 0.45, after the vertical mode initialization. Contours of surface pressure change are every 0.5 mb. Contours for the vertical motion are every 2.5 x 10^{-3} hr^{-1} for magnitudes above 10 x 10^{-3} hr^{-1} and every 15 x 10^{-3} hr^{-1} otherwise.

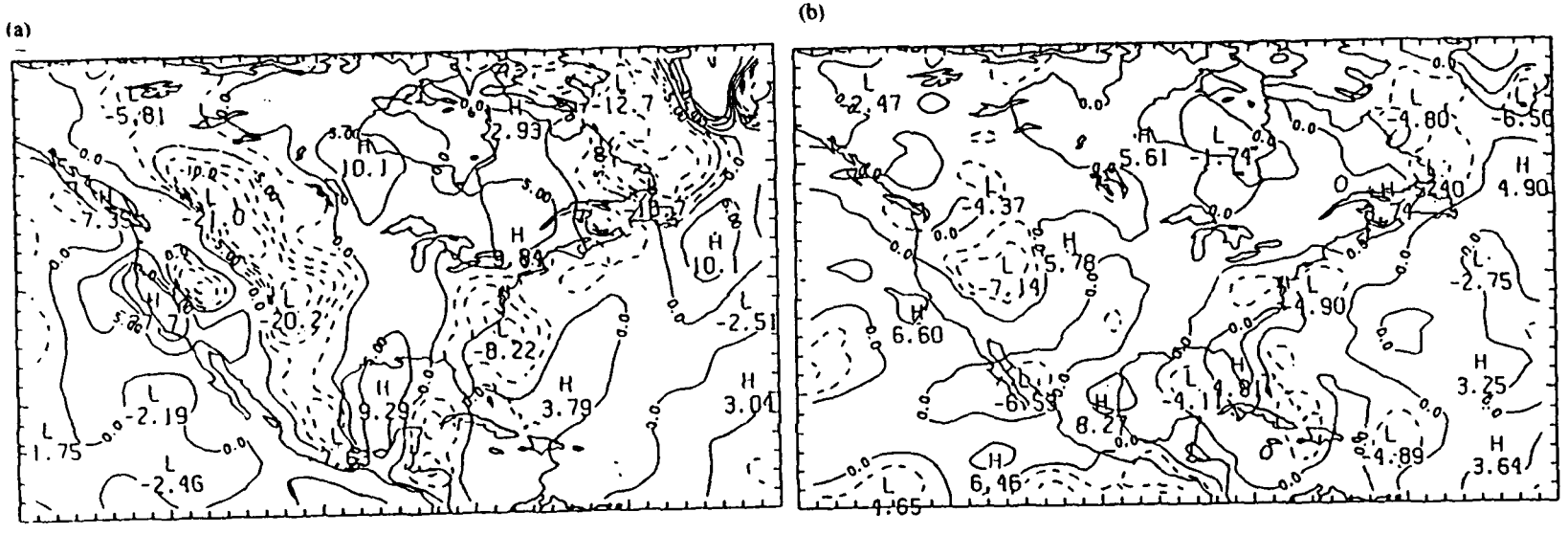

FIG. 9. The contribution to the vertical motion at sigma level $\sigma = 0.45$ in (a) the first three vertical modes, and (b) in the remaining modes. Contours of vertical motion are as in Fig. 8d.

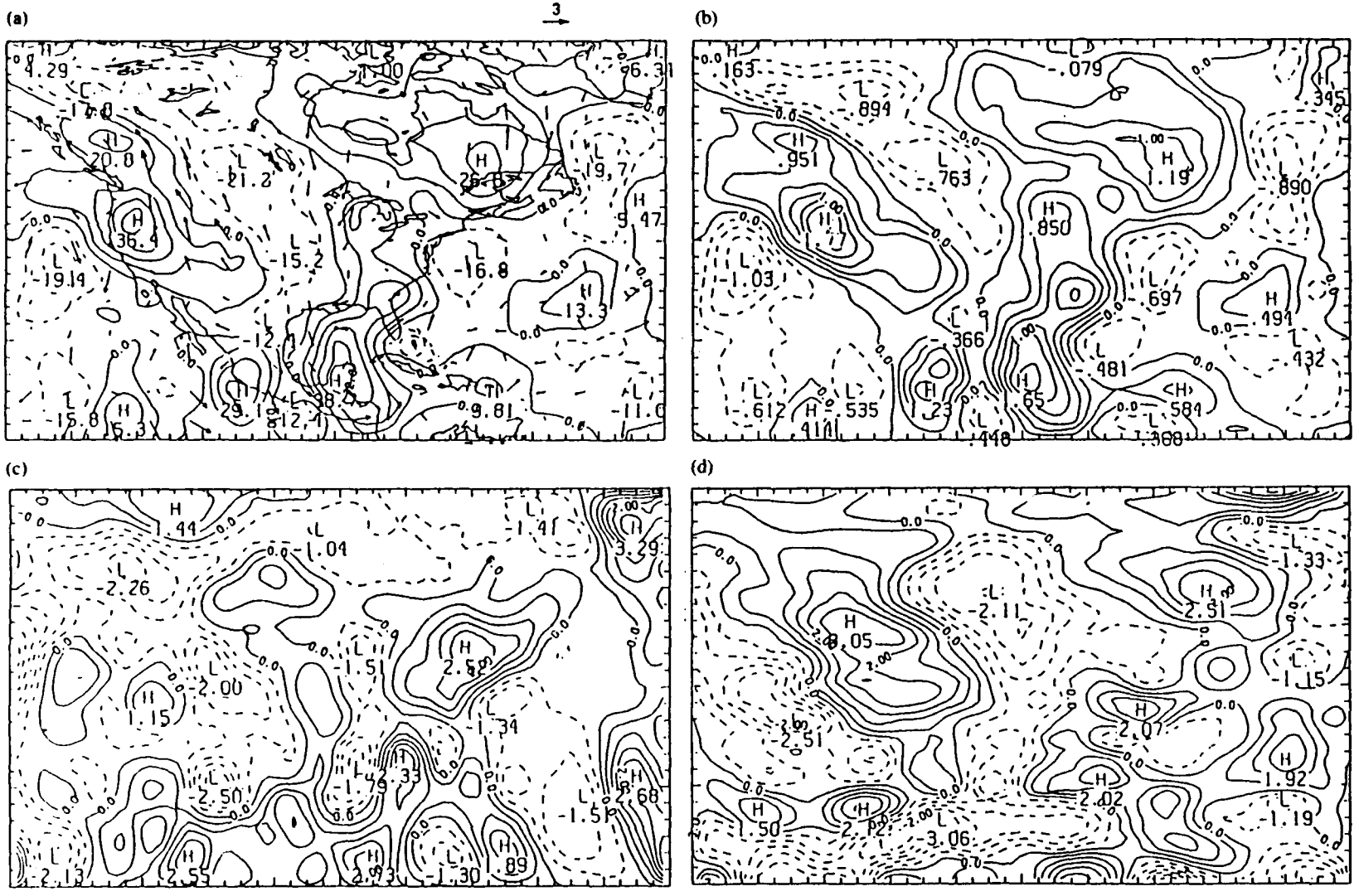

FIG. 10. The changes on the US grid in (a) the geopotential height and the wind field, (b) the temperature, (c) the u-component of the wind and (d) the v-component of the wind at the sigma level of σ = 0.25 for 12Z January 23, 1986. The contours of geopotential change are every 8 gpm and the maximum vector is 3 m s^{-1}. Contours of the wind components are 0.5 m s^{-1}, and 0.25°C for the temperature changes.

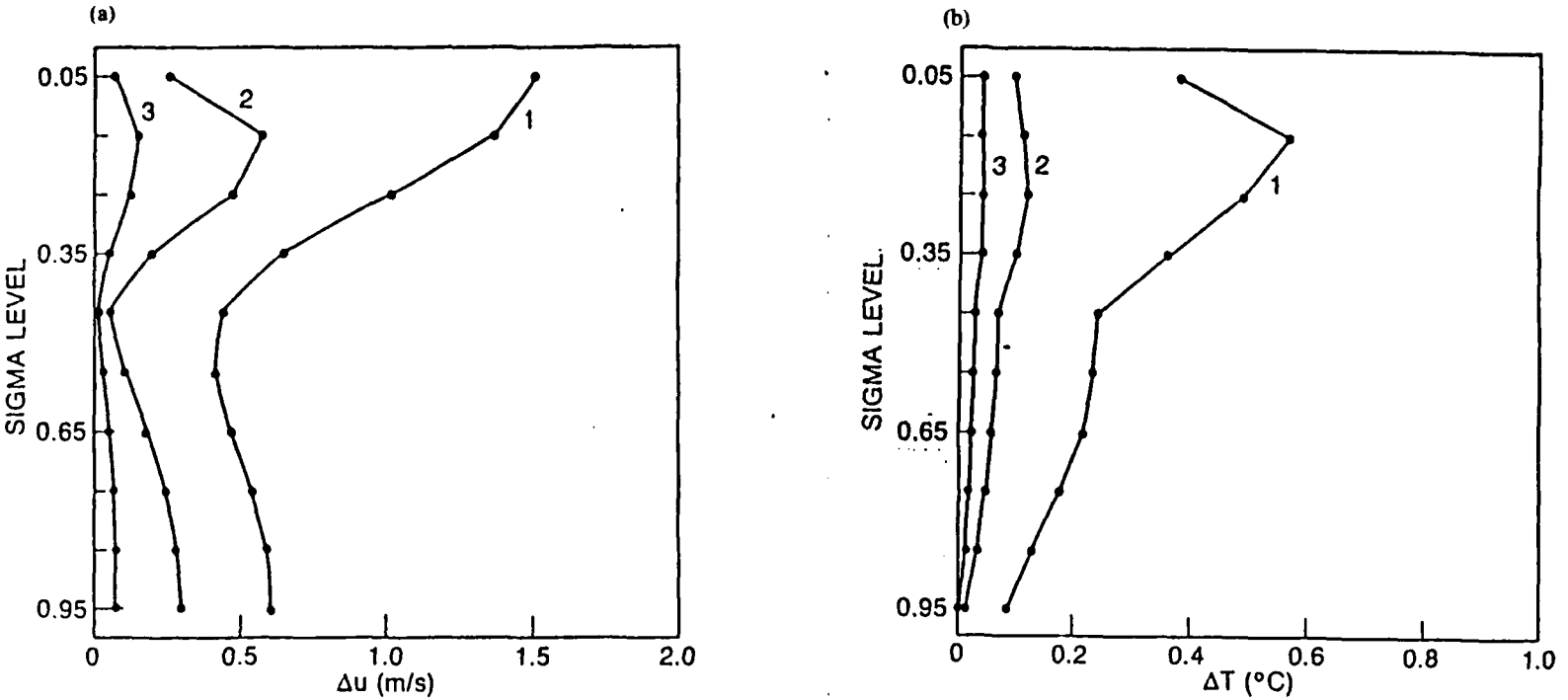

FIG. 11. The root-mean-square changes on the US grid in (a) the u-component of the wind in m s^{-1} and (b) the temperature in °C, versus sigma level for the first three iterations of the vertical mode initialization scheme, for 12Z January 23, 1986.

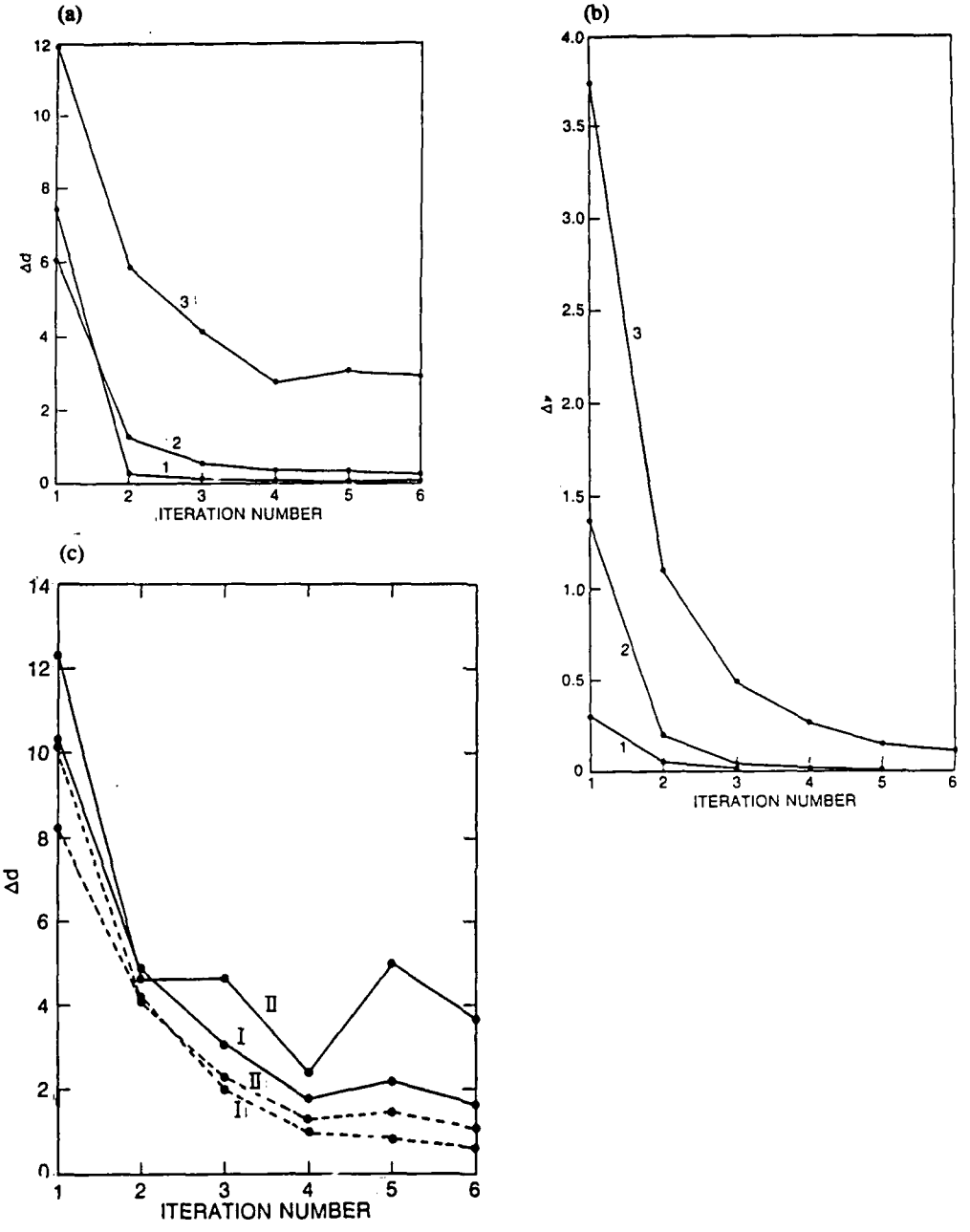

FIG. 12. The root-mean-square (rms) changes on the GALE grid in the amplitudes of (a) the mass divergence, and (b) the vorticity versus iteration number in the vertical mode initialization scheme for each of the first three vertical modes, averaged for all the analyses for the week of 12Z January 23 to 12Z January 29, 1986. (c) Comparing the rms changes in the amplitude of the mass divergence when the GALE topography (see Fig. 6b) is used (solid lines) to that when the GALE topography, which has been further smoothed (see Fig. 6c) in a five degree zone around the lateral boundary, is used (dashed lines). The analyses only on 12Z January 23 (labelled I) and 12Z January 24, 1986 (labelled II) are used.

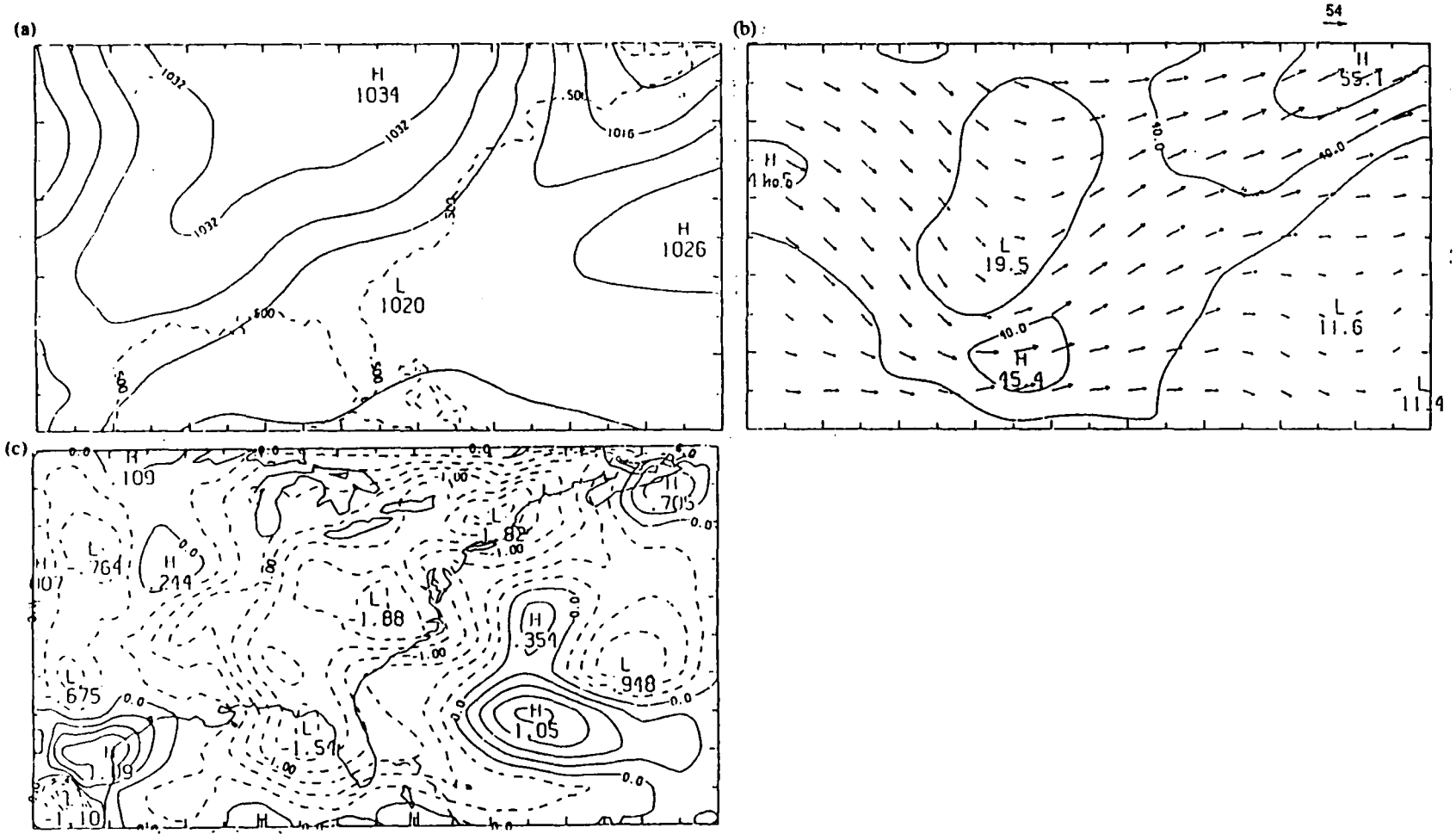

FIG. 13. The analyzed (a) sea-level pressure and (b) wind field on the GALE grid at the model sigma level σ = 0.25 for 122 January 23, 1986. The contours are as in Fig. 8a and b. The maximum wind vector shown is 54 m s^{-1}. (c) The surface pressure change in mb, after the vertical mode initialization. Contours of surface pressure change are every 0.25 mb.

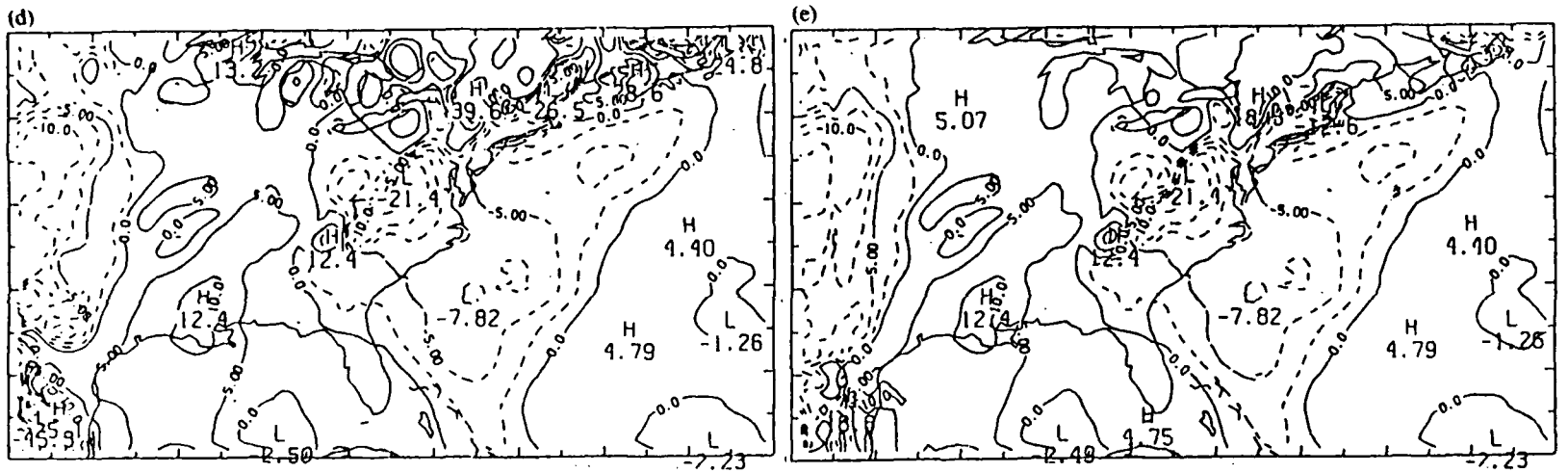

FIG. 13 cont. (d) The vertical motion field in units of 10^{-3} hr^{-1} in the middle troposphere at sigma level $\sigma = 0.45$, after the vertical mode initialization. (e) The vertical motion field as in (d) except for using the smoother topography in the five degree zone around the lateral boundary. Contours for the vertical motion are as in Fig. 8d.

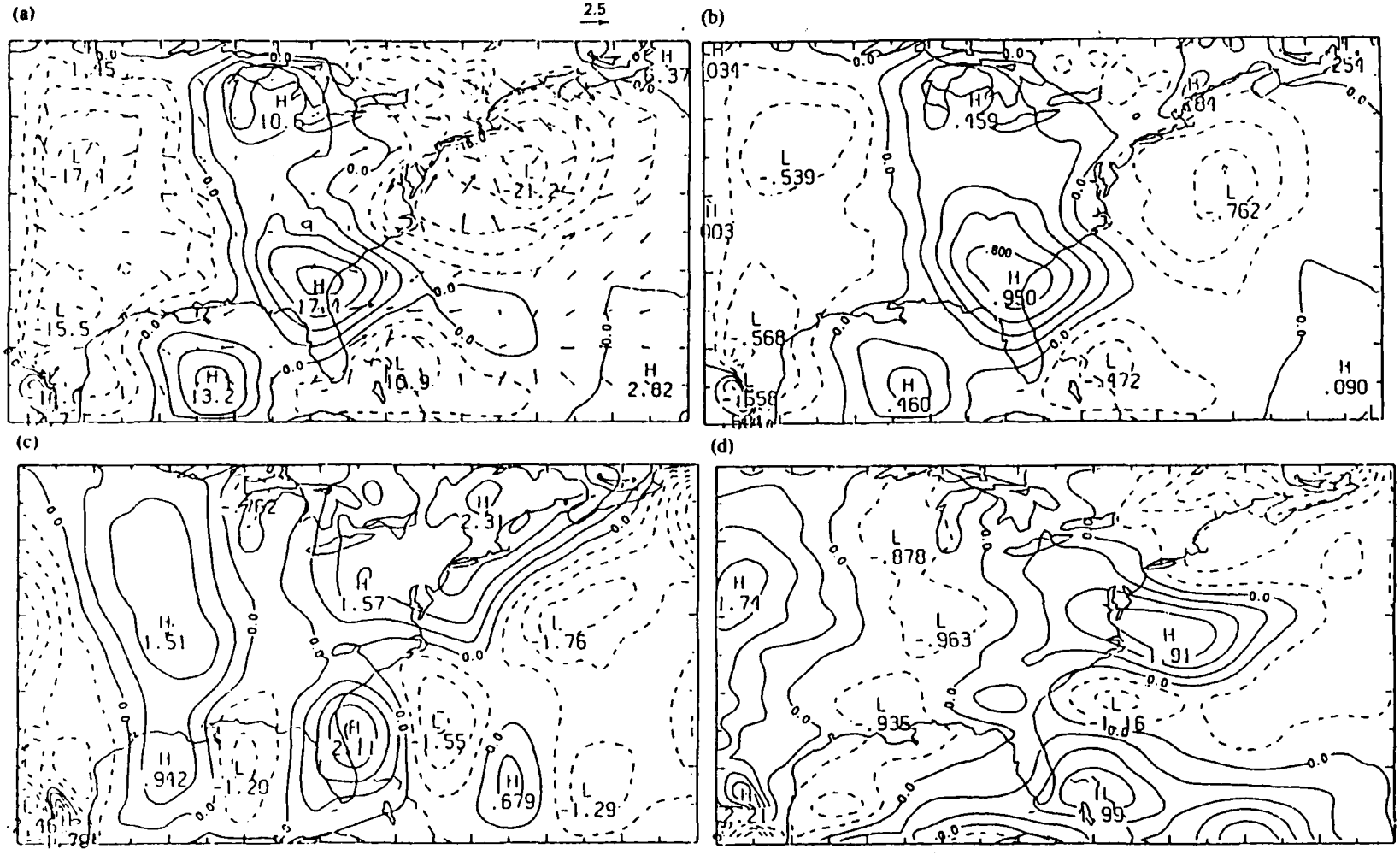

FIG. 14. The changes on the GALE grid in (a) the geopotential height and the wind field, (b) the temperature, (c) the u-component of the wind and (d) the v-component of the wind at the sigma level of σ = 0.25 for 12Z January 23, 1986. The contours of geopotential change are every 4 gpm and the maximum vector is 2.5 m s^{-1}. Contours of the wind components are 0.5 m s^{-1}, and 0.2°C for the temperature changes.

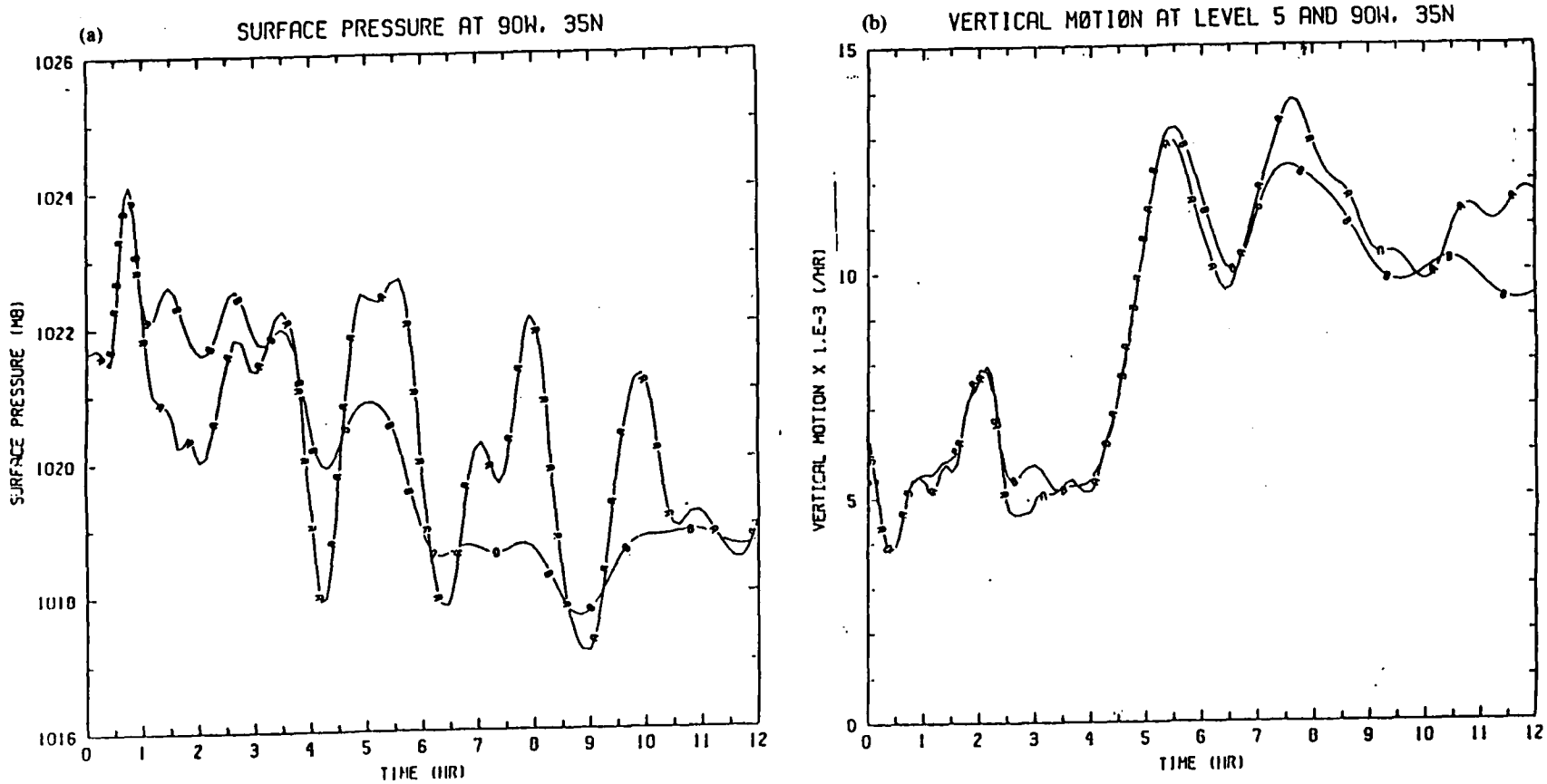

FIG. 15. Time series of (a) surface pressure in mb and (b) the vertical motion (in sigma coordinates) in $hour^{-1}$ at sigma level $\sigma = 0.5$, at a grid point on the GALE grid at 90°W and 35°N, during the first 12 hours of integration. Curves are for uninitialized initial conditions for an explicit integration in time (Curve A) and a split-explicit integration (Curve B).

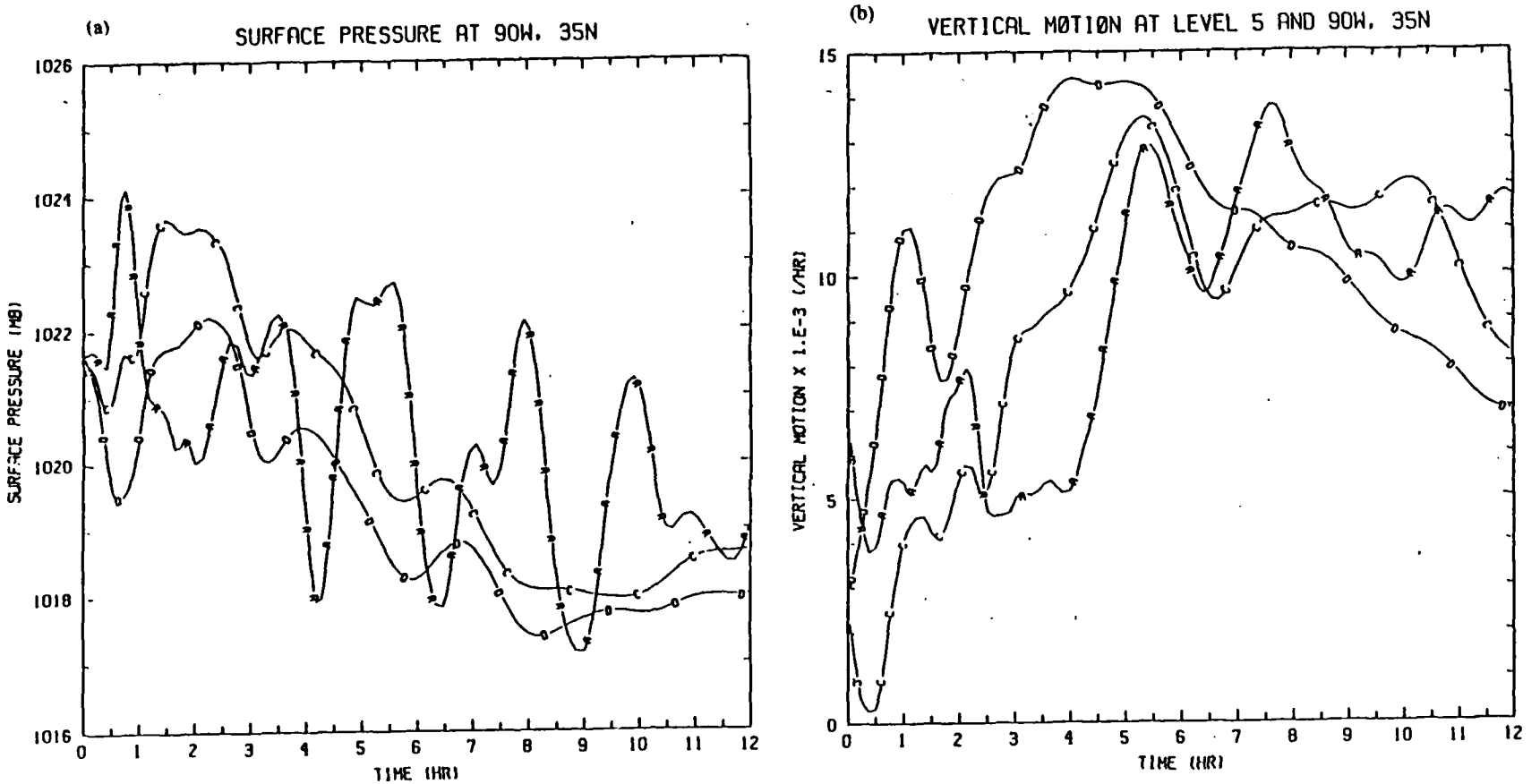

FIG. 16. Time series of (a) surface pressure in mb and (b) the vertical motion (in sigma coordinates) in hour^{-1} at sigma level $\sigma = 0.5$, at a grid point on the GALE grid at 90°W and 35°N, during the first 12 hours of integration. Curves are for uninitialized initial conditions for an explicit integration in time (Curve A); for a split-explicit integration with a non-divergent initial condition (Curve C) and for split-explicit integrations with a non-linear mass balance (Curve D).

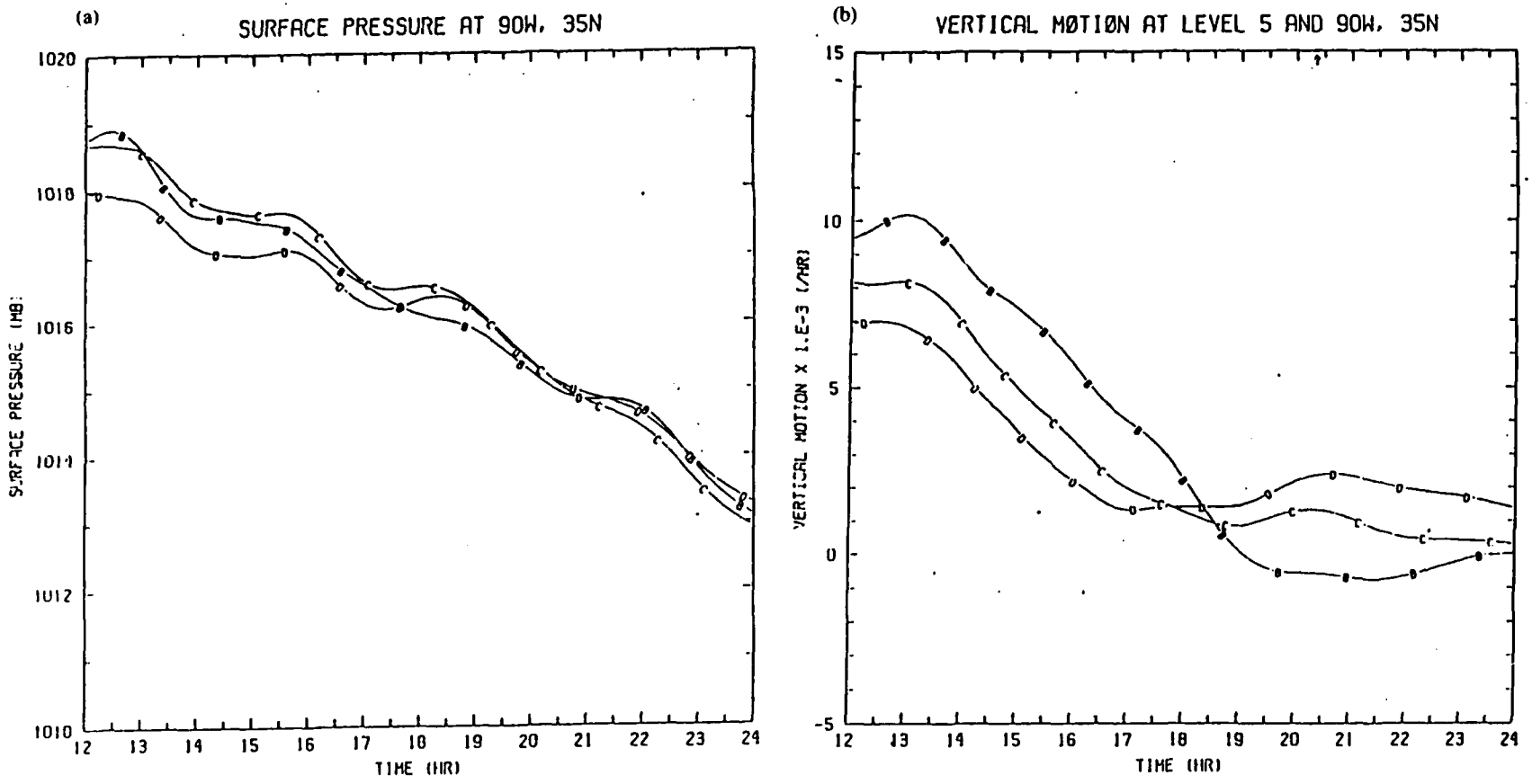

FIG. 17. Time series of (a) surface pressure in mb and (b) the vertical motion (in sigma coordinates) in hour^{-1} at sigma level σ = 0.5, at a grid point on the GALE grid at 90°W and 35°N, during the second 12 hours of integration. Curves are for uninitialized initial conditions for a split-explicit integration (Curve B); for a split-explicit integration with a non-divergent initial condition (Curve C) and for split-explicit integrations with a non-linear mass balance (Curve D).

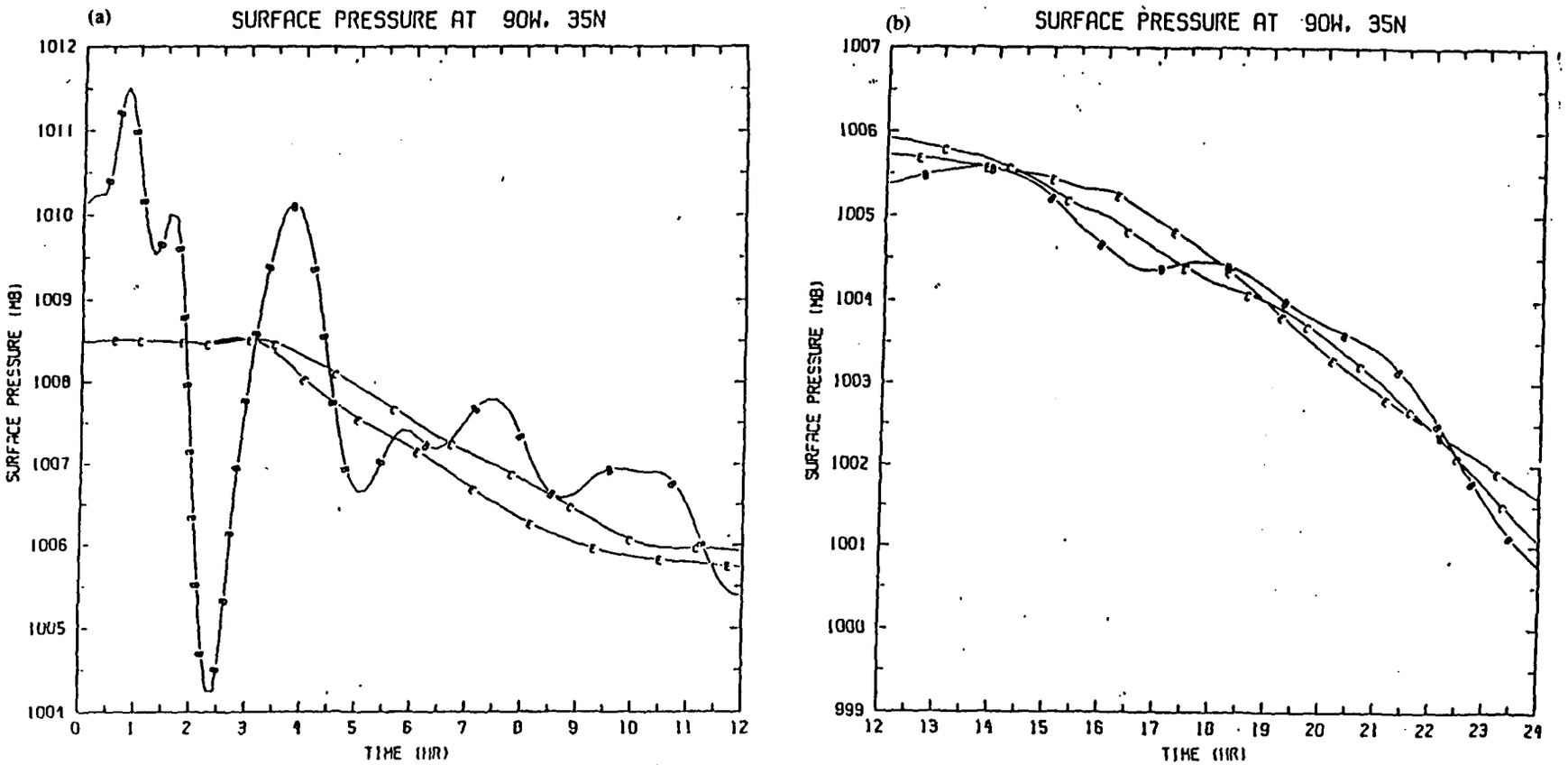

FIG. 18. Time series of surface pressure in mb and the vertical motion (in sigma coordinates) at σ = 0.5, at a grid point at 90°W and 35°N on the US grid. (a) shows the surface pressure during the first 12 hours of integration and (b) the second 12 hours of integration. (c) shows the vertical motion in hour^{-1} during the first 12 hours of integration and (d) the second 12 hours of integration. Curves are for uninitialized initial conditions (Curve B) and for initialized initial conditions (Curve C), using the Perkey Kreitzberg lateral boundary scheme. Curve E is for initialized initial conditions with the Davies lateral boundary scheme.

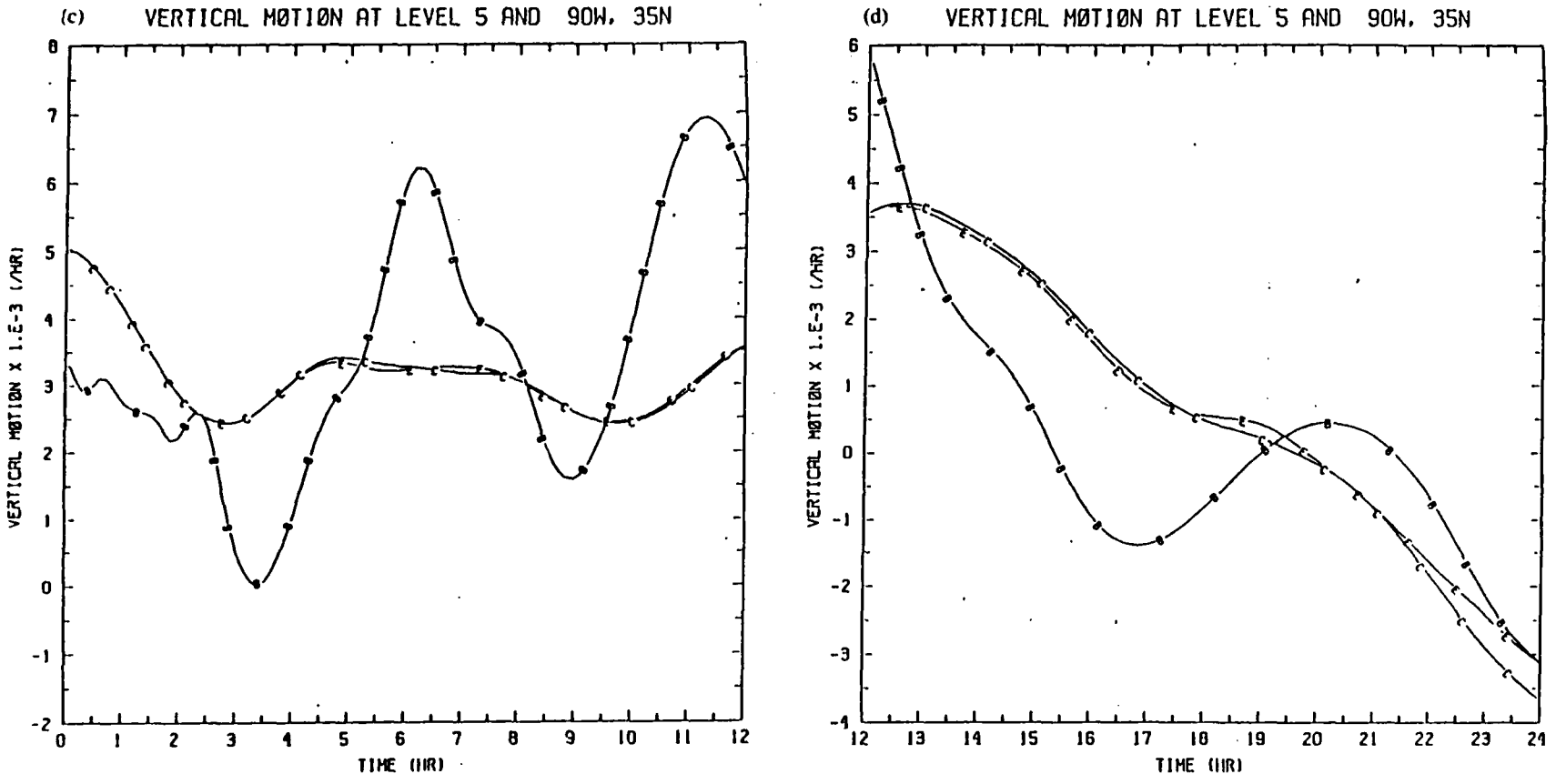

FIG. 18. Time series of surface pressure in mb and the vertical motion (in sigma coordinates) at σ = 0.5, at a grid point at 90°W and 35°N on the US grid. (a) shows the surface pressure during the first 12 hours of integration and (b) the second 12 hours of integration. (c) shows the vertical motion in hour^{-1} during the first 12 hours of integration and (d) the second 12 hours of integration. Curves are for uninitialized initial conditions (Curve B) and for initialized initial conditions (Curve C), using the Perkey Kreitzberg lateral boundary scheme. Curve E is for initialized initial conditions with the Davies lateral boundary scheme.

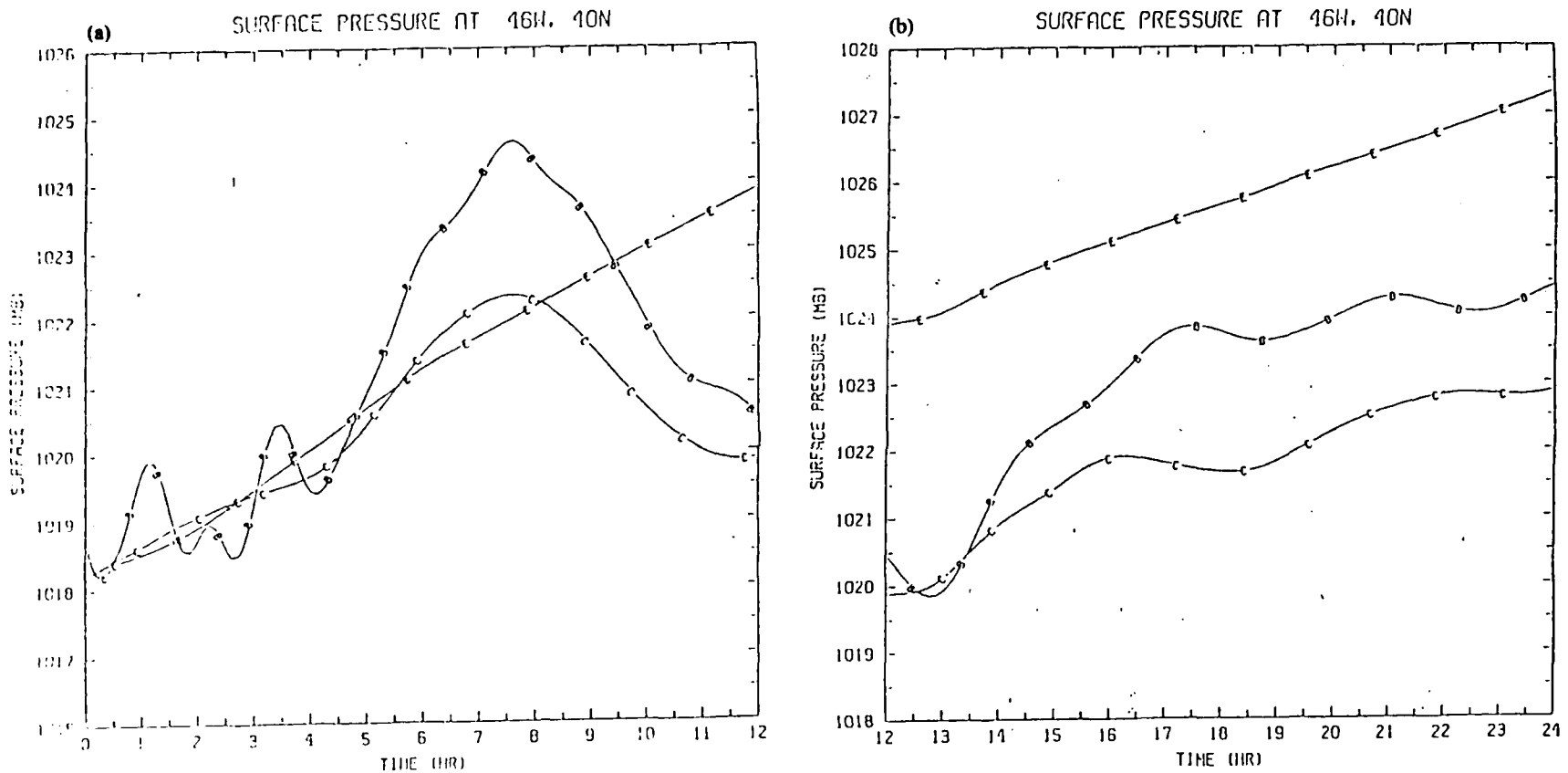

FIG. 19. Time series of surface pressure in mb and the vertical motion (in sigma coordinates) in hour^{-1} at σ = 0.5, at a grid point in the boundary zone on the US grid at 46°W and 40°N. (a) shows the surface pressure in mb during the first 12 hours of integration and (b) the second 12 hours of integration. (c) shows the vertical motion during the first 12 hours of integration and (d) the second 12 hours of integration. Curves are as in Fig. 18.

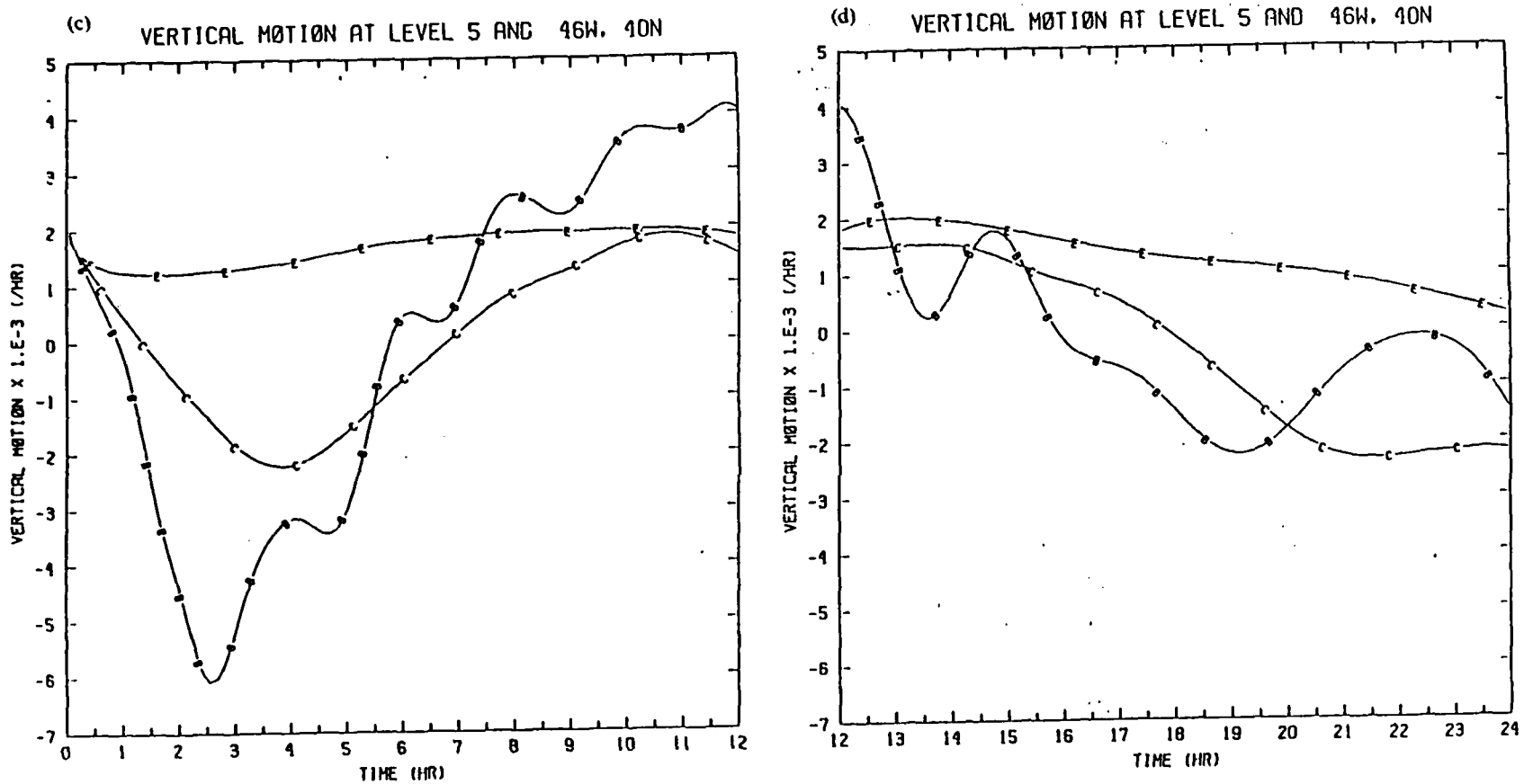

FIG. 19. Time series of surface pressure in mb and the vertical motion (in sigma coordinates) in hour^{-1} at σ = 0.5, at a grid point in the boundary zone on the US grid at 46°W and 40°N. (a) shows the surface pressure in mb during the first 12 hours of integration and (b) the second 12 hours of integration. (c) shows the vertical motion during the first 12 hours of integration and (d) the second 12 hours of integration. Curves are as in Fig. 18.

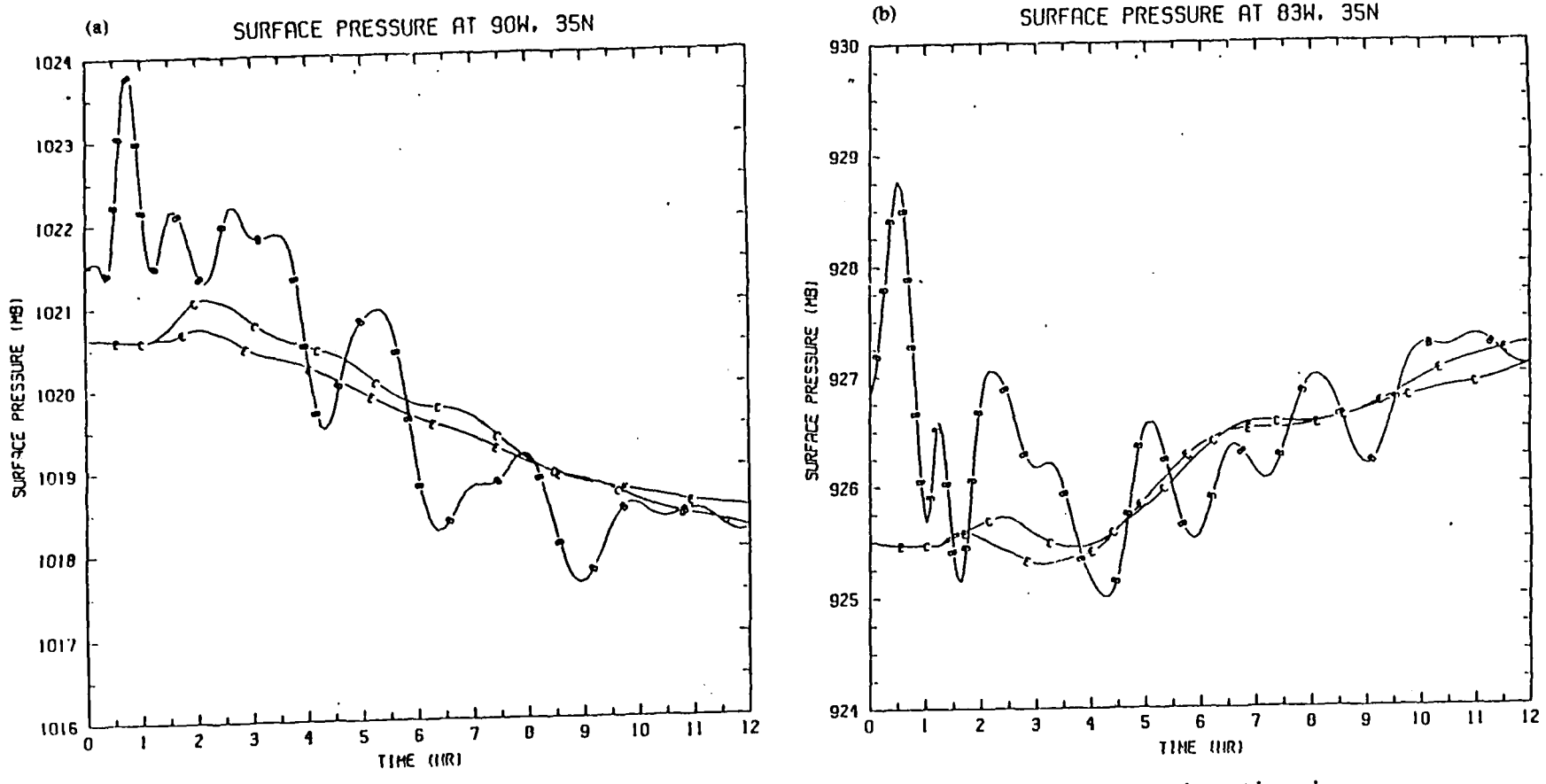

FIG. 20. Time series of surface pressure and the vertical motion (in sigma coordinates) at σ = 0.5 at two grid points on the GALE grid during the 12 hours of integration. (a) shows the surface pressure in mb at 90°W and 35°N and (b) at 83°W and 35°N. (c) shows the vertical motion in hour^{-1} at 90°W and 35°N and (d) at 83°W and 35°N. Curves are for uninitialized initial conditions (Curve B) and for initialized initial conditions (Curve C), using the Perkey Kreitzberg lateral boundary scheme. Curve E is for initialized initial conditions with the Davies lateral boundary scheme.

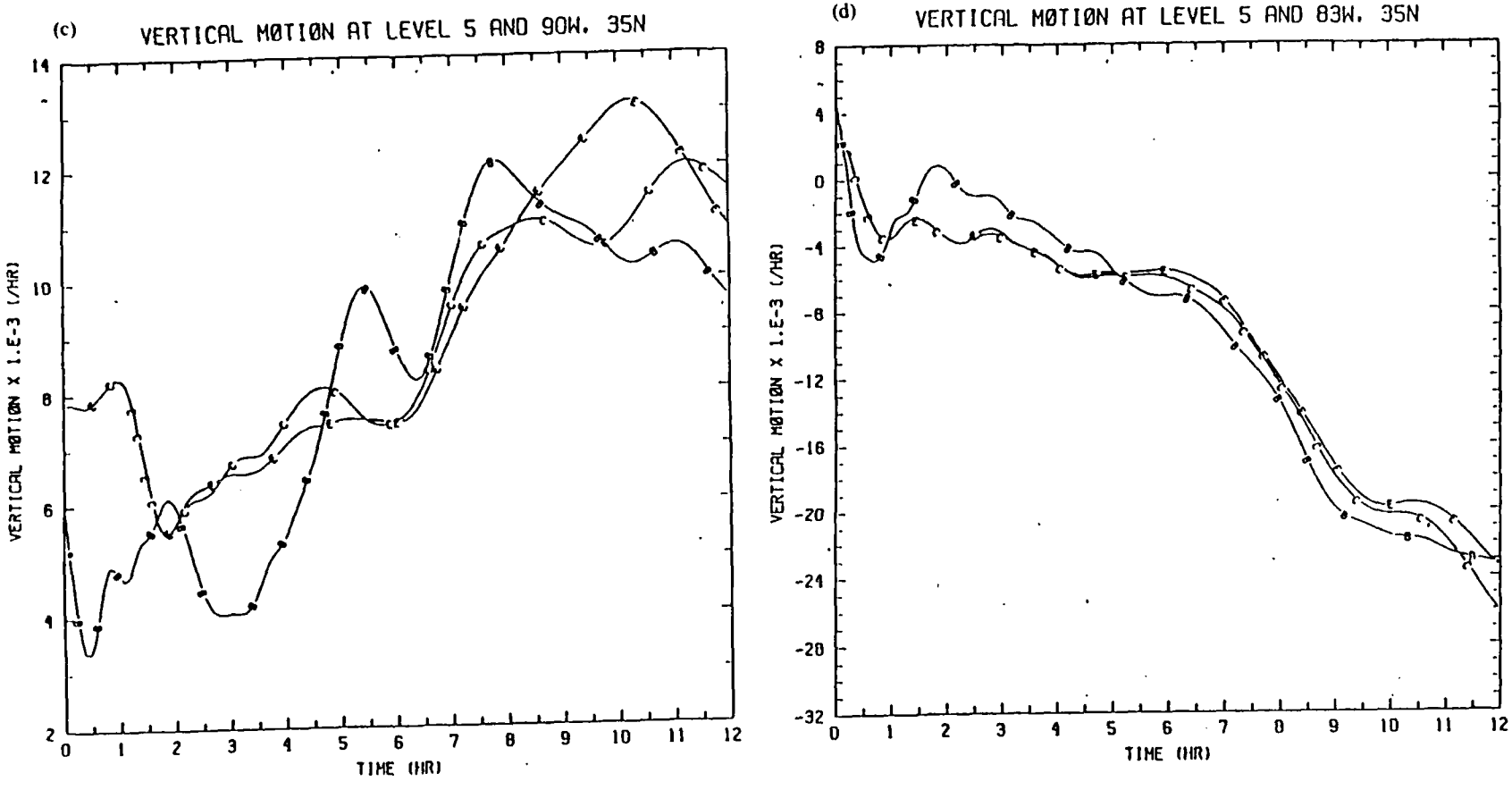

FIG. 20. Time series of surface pressure and the vertical motion (in sigma coordinates) at σ = 0.5 at two grid points on the GALE grid during the 12 hours of integration. (a) shows the surface pressure in mb at 90°W and 35°N and (b) at 83°W and 35°N. (c) shows the vertical motion in hour^{-1} at 90°W and 35°N and (d) at 83°W and 35°N. Curves are for uninitialized initial conditions (Curve B) and for initialized initial conditions (Curve C), using the Perkey Kreitzberg lateral boundary scheme. Curve E is for initialized initial conditions with the Davies lateral boundary scheme.

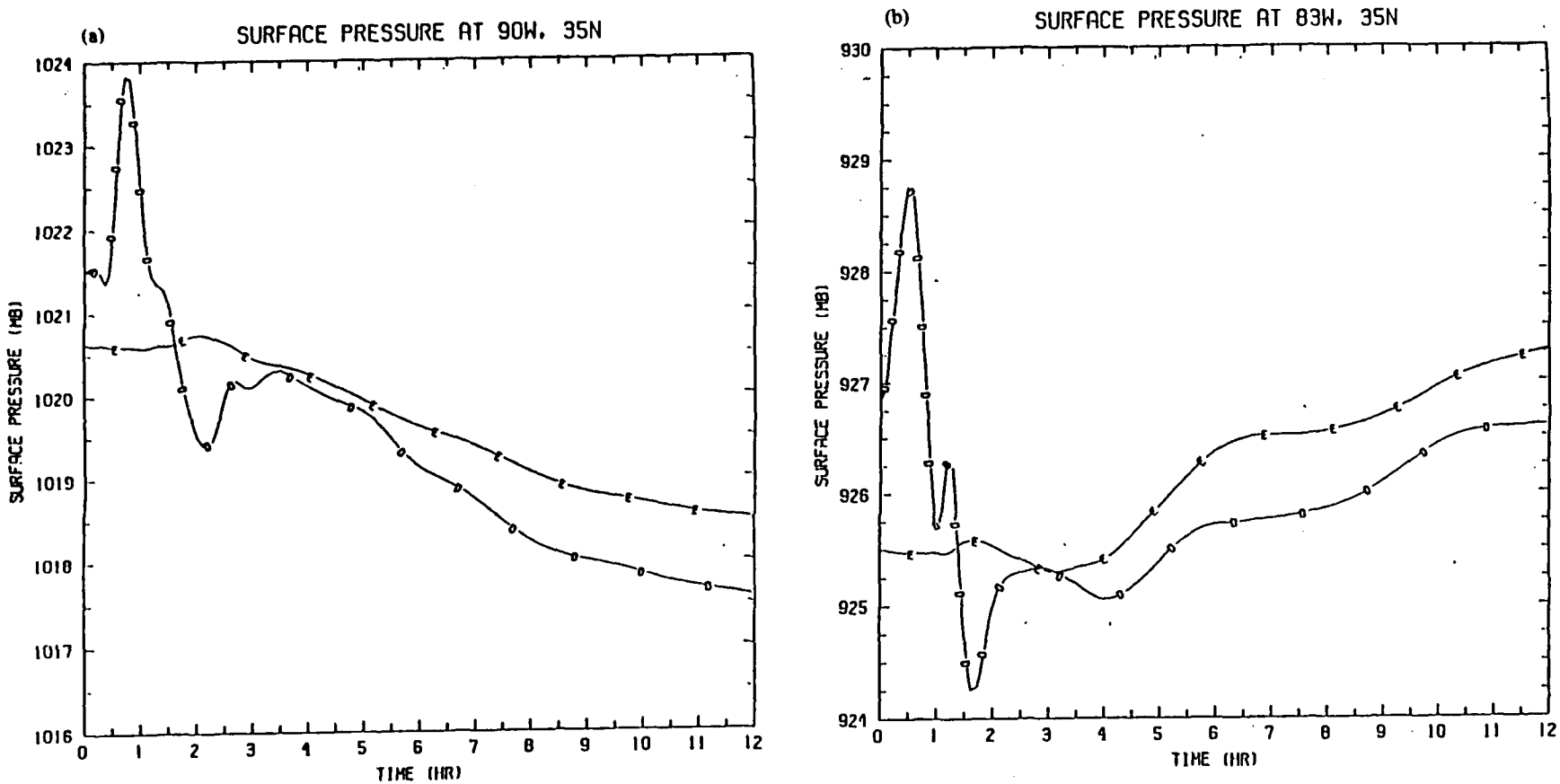

FIG. 21. Time series of surface pressure and the vertical motion (in sigma coordinates) at σ = 0.5 at two grid points on the GALE grid during the 12 hours of integration. (a) shows the surface pressure in mb at 90°W and 35°N and (b) at 83°W and 35°N. (c) shows the vertical motion in hour^{-1} at 90°W and 35°N and (b) at 83°W and 35°N. Curves are for uninitialized initial conditions (Curve D) and for initialized initial conditions (Curve E), using the Davies lateral boundary scheme.

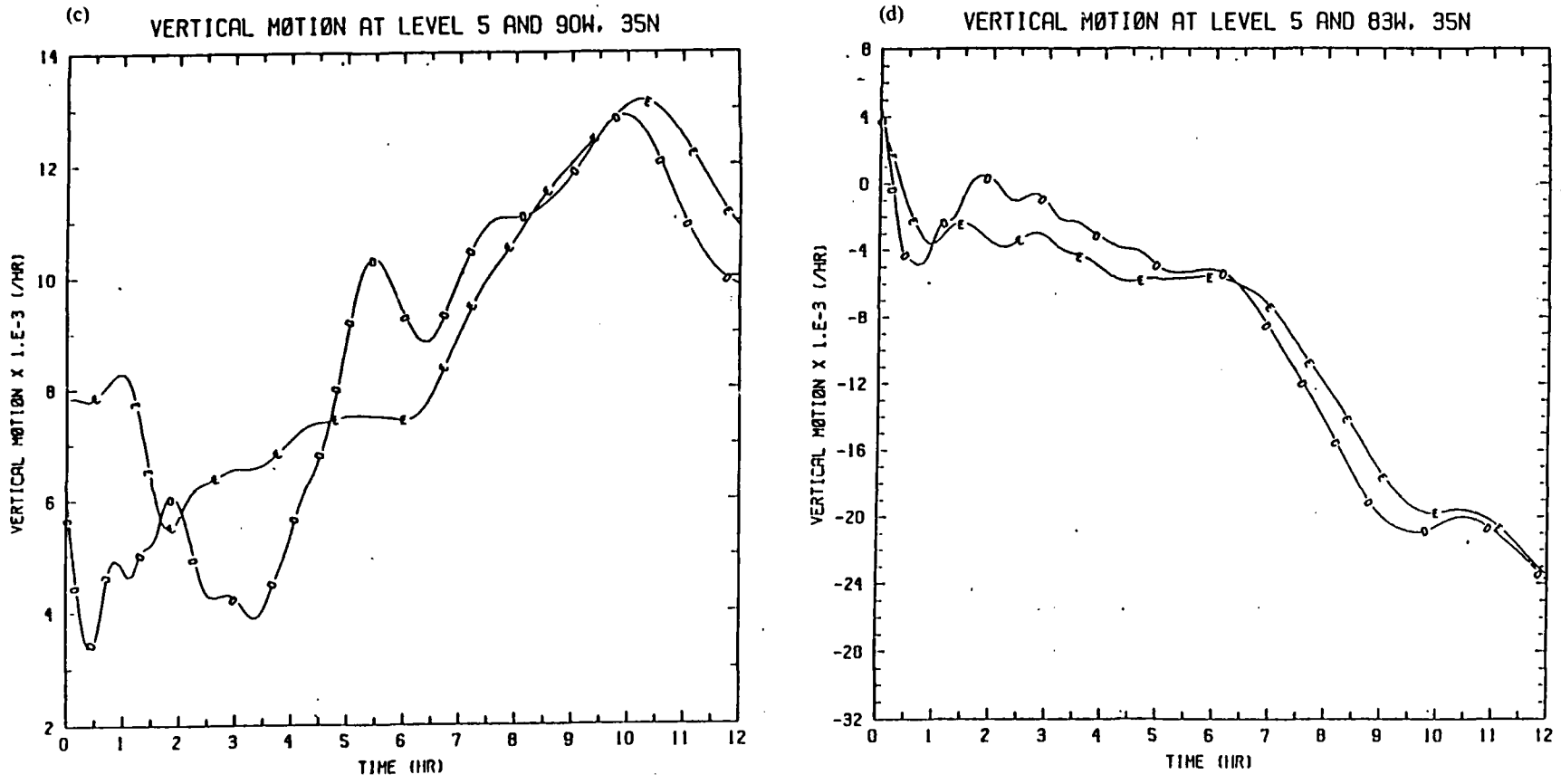

FIG. 21. Time series of surface pressure and the vertical motion (in sigma coordinates) at σ = 0.5 at two grid points on the GALE grid during the 12 hours of integration. (a) shows the surface pressure in mb at 90°W and 35°N and (b) at 83°W and 35°N. (c) shows the vertical motion in hour^{-1} at 90°W and 35°N and (b) at 83°W and 35°N. Curves are for uninitialized initial conditions (Curve D) and for initialized initial conditions (Curve E), using the Davies lateral boundary scheme.

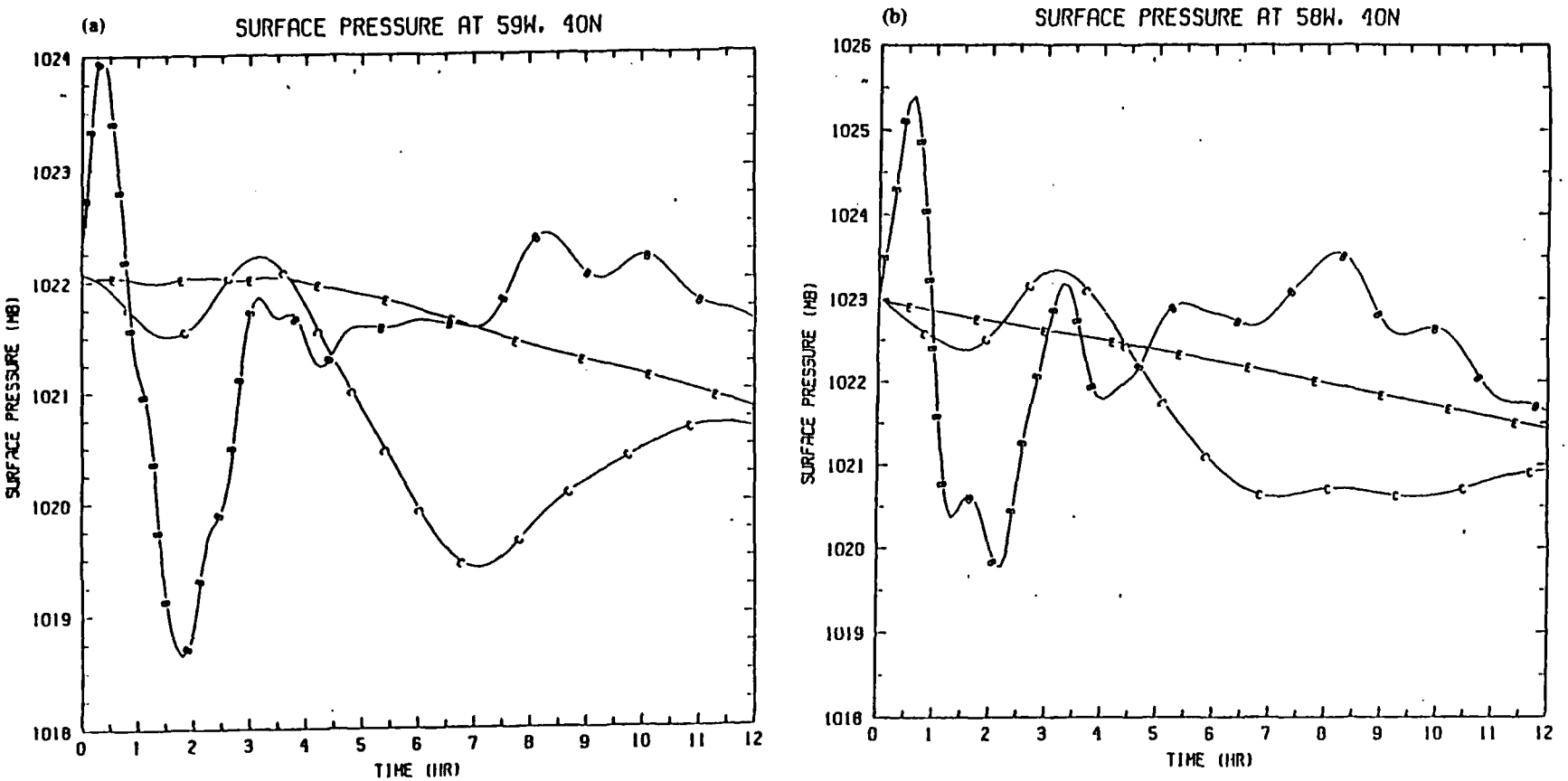

FIG. 22. Time series of surface pressure and the vertical motion (in sigma coordinates) at σ = 0.5 at two grid points in the boundary zone on the GALE grid during the 12 hours of integration. (a) shows the surface pressure in mb at 59°W and 40°N and (b) at 58°W and 40°N. (c) shows the vertical motion in hour^{-1} at 59°W and 40°N and (d) at 58°W and 40°N. Curves are for uninitialized initial conditions (Curve B) and for initialized initial conditions (Curve C), using the Perkey Kreitzberg lateral boundary scheme. Curve E is for initialized initial conditions with the Davies lateral boundary scheme.

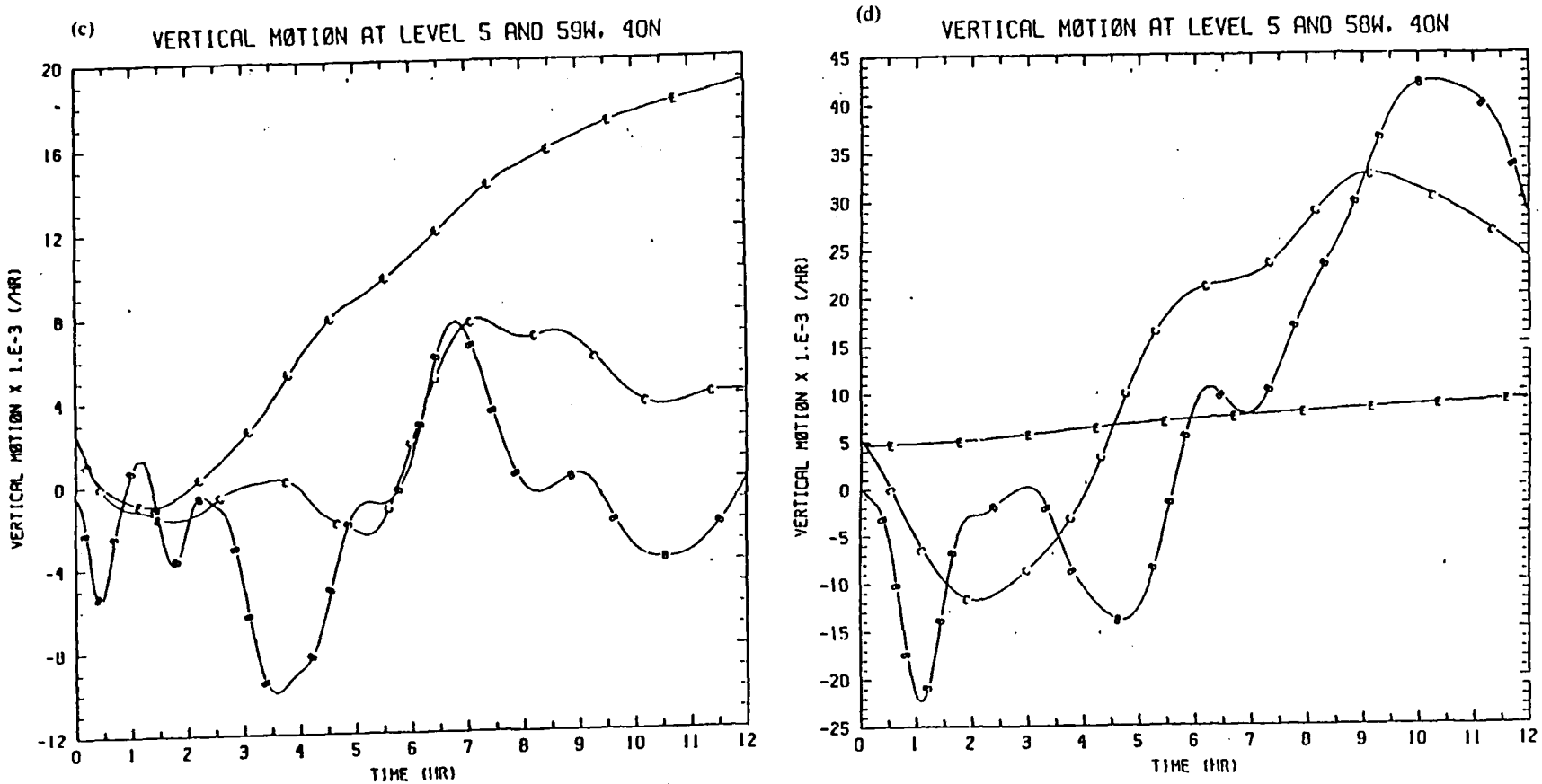

FIG. 22. Time series of surface pressure and the vertical motion (in sigma coordinates) at σ = 0.5 at two grid points in the boundary zone on the GALE grid during the 12 hours of integration. (a) shows the surface pressure in mb at 59°W and 40°N and (b) at 58°W and 40°N. (c) shows the vertical motion in hour^{-1} at 59°W and 40°N and (d) at 58°W and 40°N. Curves are for uninitialized initial conditions (Curve B) and for initialized initial conditions (Curve C), using the Perkey Kreitzberg lateral boundary scheme. Curve E is for initialized initial conditions with the Davies lateral boundary scheme.

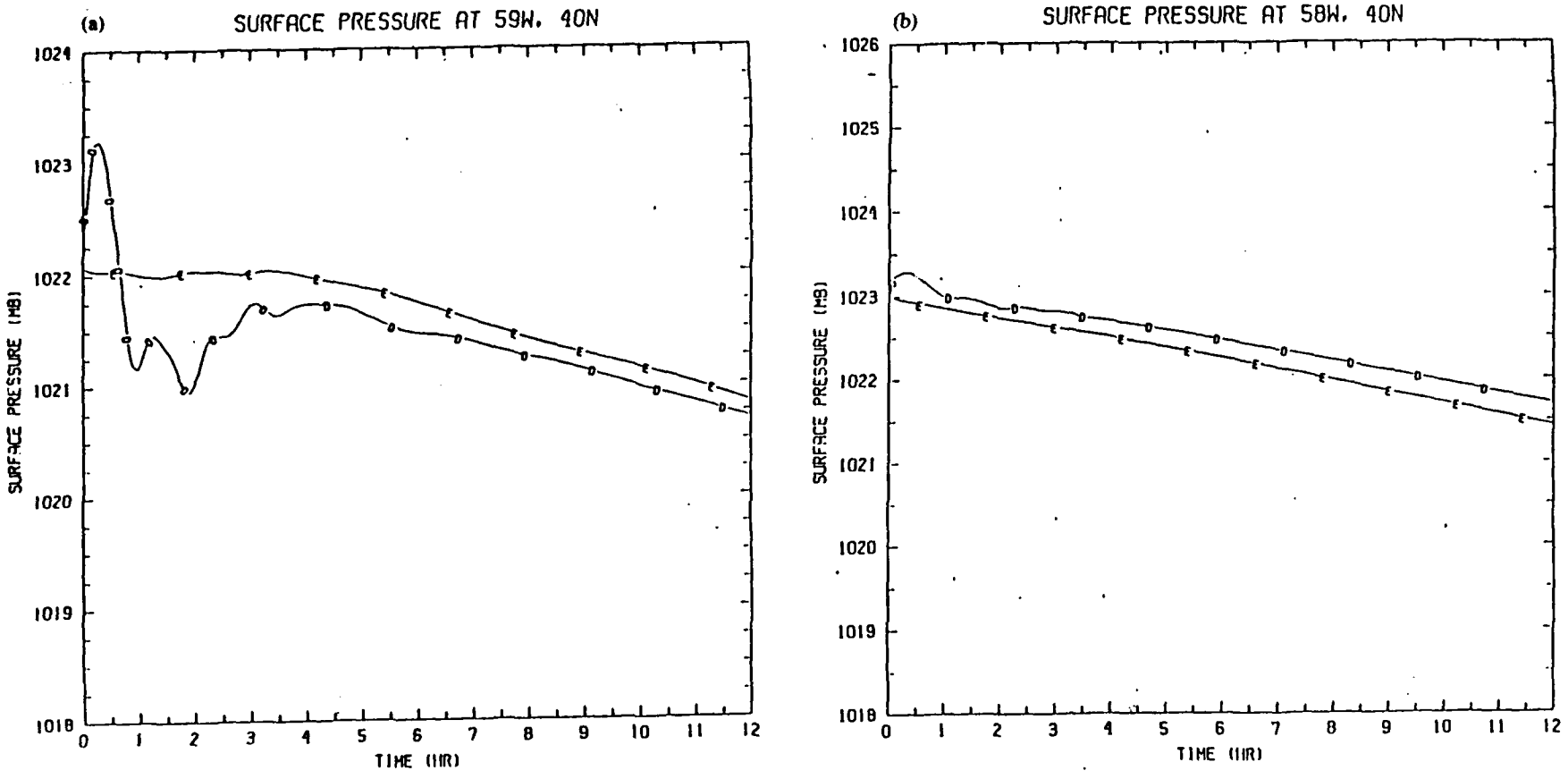

FIG. 23. Time series of surface pressure and the vertical motion (in sigma coordinates) at σ = 0.5 at two grid points in the boundary zone on the GALE grid during the 12 hours of integration. (a) shows the surface pressure in mb at 59°W and 40°N and (b) at 58°W and 40°N. (c) shows the vertical motion in hour^{-1} at 59°W and 40°N and (d) at 58°W and 40°N. Curves are for uninitialized initial conditions (Curve D) and for initialized initial conditions (Curve E), using the Davies lateral boundary scheme.

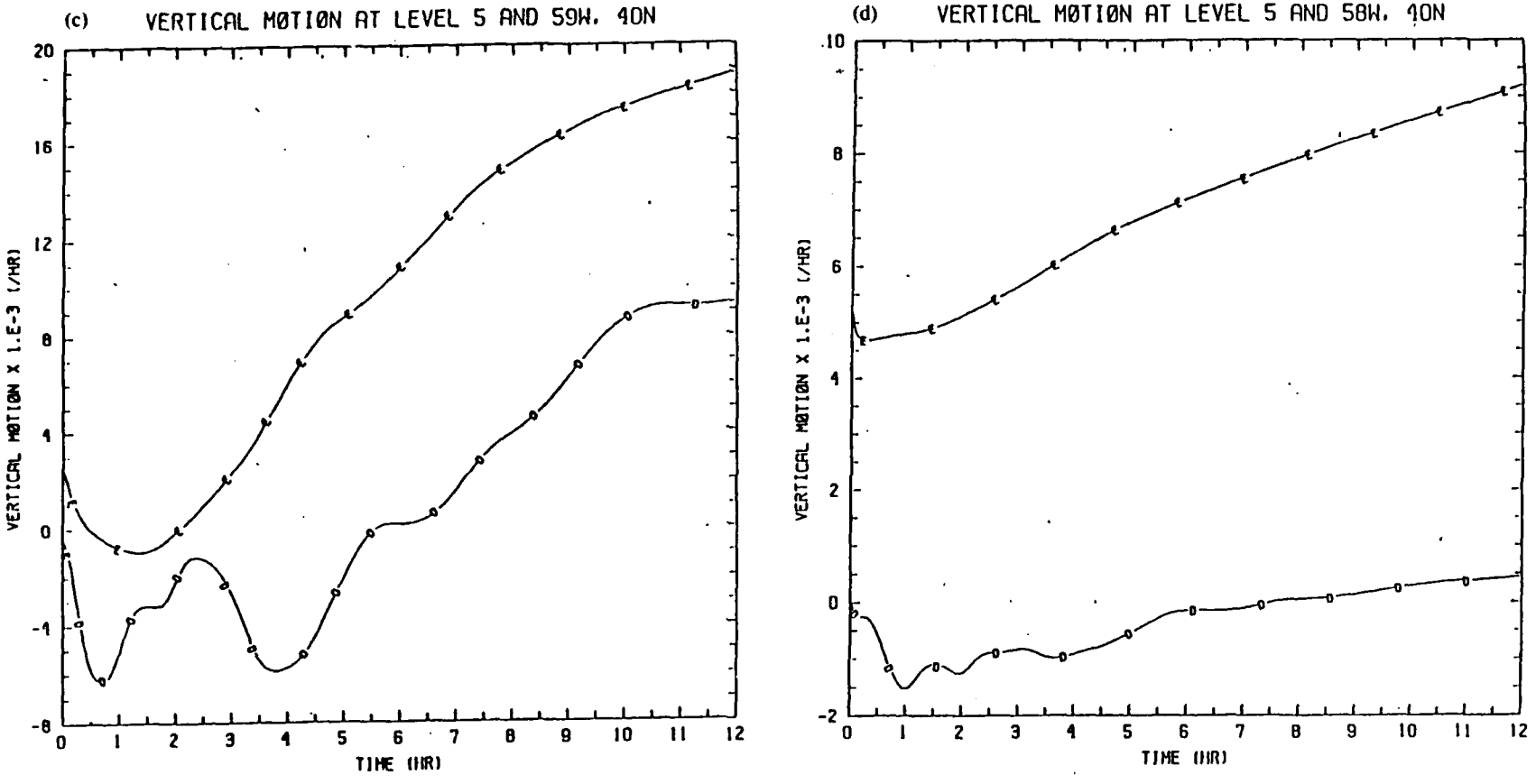

FIG. 23. Time series of surface pressure and the vertical motion (in sigma coordinates) at σ = 0.5 at two grid points in the boundary zone on the GALE grid during the 12 hours of integration. (a) shows the surface pressure in mb at 59°W and 40°N and (b) at 58°W and 40°N. (c) shows the vertical motion in hour^{-1} at 59°W and 40°N and (d) at 58°W and 40°N. Curves are for uninitialized initial conditions (Curve D) and for initialized initial conditions (Curve E), using the Davies lateral boundary scheme.